

2

NAVAL POSTGRADUATE SCHOOL

Monterey, California

AD-A261 925



DTIC
ELECTE
MAR 29 1993
S C D

THESIS

UNSTEADY AIRFOIL FLOW SOLUTIONS
ON MOVING ZONAL GRIDS

by

Antonio M. Cricelli

December 1992

Thesis Advisor:
Co-Advisor:

John A. Ekaterinaris
Max F. Platzer

Approved for public release; distribution is unlimited

93 3 26 084

93-06311



Unclassified

Security Classification of this page

REPORT DOCUMENTATION PAGE

1a Report Security Classification: Unclassified		1b Restrictive Markings	
2a Security Classification Authority		3 Distribution/Availability of Report	
2b Declassification/Downgrading Schedule		Approved for public release; distribution is unlimited.	
4 Performing Organization Report Number(s)		5 Monitoring Organization Report Number(s)	
6a Name of Performing Organization Naval Postgraduate School	6b Office Symbol (if applicable) 31	7a Name of Monitoring Organization Naval Postgraduate School	
6c Address (city, state, and ZIP code) Monterey CA 93943-5000		7b Address (city, state, and ZIP code) Monterey CA 93943-5000	
8a Name of Funding/Sponsoring Organization	6b Office Symbol (if applicable)	9 Procurement Instrument Identification Number	
Address (city, state, and ZIP code)		10 Source of Funding Numbers	
		Program Element No	Project No
		Task No	Work Unit Accession No
11 Title (include security classification) UNSTEADY AIRFOIL FLOW SOLUTIONS ON MOVING ZONAL GRIDS			
12 Personal Author(s) Antonio M. Cricelli			
13a Type of Report Master's Thesis	13b Time Covered From To	14 Date of Report (year, month, day) 1992, December, 17	15 Page Count 147
16 Supplementary Notation The views expressed in this thesis are those of the author and do not reflect the official policy or position of the Department of Defense or the U.S. Government.			
17 Cosati Codes		18 Subject Terms (continue on reverse if necessary and identify by block number)	
Field	Group	Subgroup	
		CFD, Unsteady Flow, Zonal Grids	
19 Abstract (continue on reverse if necessary and identify by block number)			
<p>Investigation of subsonic and transonic steady and unsteady flowfields over airfoils is an active area of current computational and experimental research. The performance of rotary wing and fixed wing aircraft can be enhanced by taking advantage of unsteady phenomena such as dynamic lift. However, several undesirable effects have prevented designers from taking advantage of these concepts. In the past few years many advances have been made in algorithm, development for the numerical solution of the Euler and the Navier Stokes equations. In this study, these new techniques are applied to body fixed zonal grid approach. This zonal approach is more computationally efficient in solving the governing equations than previous approaches, and has certain advantages over the standard single moving grid approach. The zonal grids consists of two grids, one being the inner grid which is fixed to the airfoil, and the other being the outer grid which extends to the far field or to a specified outer boundary. The inner grid is allowed to rotate with the body, while the outer grid remains fixed. The thin--layer Navier--Stokes equations are solved for inner grid, and the Euler equations are solved for the outer grid. Communication between the two grids is accomplished by interpolated the flow quantities at the zonal interface. Solutions are obtained for flows at fixed angles of incidence, and for unsteady flows over pitching and oscillating airfoils. The computed results are in good agreement with available experimental data.</p>			
20 Distribution/Availability of Abstract <input checked="" type="checkbox"/> unclassified/unlimited <input type="checkbox"/> same as report <input type="checkbox"/> DTIC users		21 Abstract Security Classification Unclassified	
22a Name of Responsible Individual Max F. Platzer		22b Telephone (include Area Code) (408) 656 - 2058	22c Office Symbol AA/PI

DD FORM 1473, 84 MAR

83 APR edition may be used until exhausted

security classification of this page

All other editions are obsolete

Unclassified

Approved for public release; distribution is unlimited

Unsteady Airfoil Flow Solutions on
Moving Zonal Grids

by

Antonio M. Cricelli
Computer Engineer, NPS
B.S., Penn State University, 1987

Submitted in partial fulfillment of the
requirements for the degree of

MASTER OF SCIENCE IN AERONAUTICAL ENGINEERING

from the

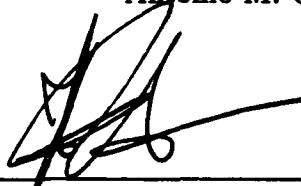
NAVAL POSTGRADUATE SCHOOL


December, 1992

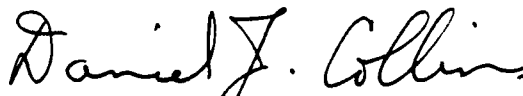
Author:


Antonio M. Cricelli

Approved by:


John A. Ekaterinaris, Thesis Advisor


Max F. Platzter, Thesis Co-Advisor


Daniel J. Collins, Chairman
Department of Aeronautics and Astronautics

ABSTRACT

Subsonic and transonic steady and unsteady flowfields over airfoils are investigated with the numerical solution of the governing equations. This study aims to enhance the performance of rotary wing and fixed wing aircraft by better understanding and by taking advantage of unsteady phenomena such as dynamic lift. In the past few years many advances have been made in algorithm development for the numerical solution of the Euler and the Navier Stokes equations. In this study, these new zonal techniques are applied. A zonal approach is more computationally efficient in solving the governing equations than previous approaches, and has certain advantages over the standard single moving grid approach. The zonal grid consists of two grids, one being the inner grid which is fixed to the airfoil, and the other being the outer grid which extends to the far field or to a specified outer boundary. The inner grid is allowed to rotate with the body, while the outer grid remains fixed. The thin-layer Navier-Stokes equations are solved for the inner grid, while the Euler equations are solved for the outer grid. Communication between the two grids is accomplished by interpolating the flow quantities at the zonal interface. Solutions are obtained for flows at fixed angles of incidence, and for unsteady flows over pitching and oscillating airfoils. The computed results are in good agreement with available experimental data.

DTIC QUALITY INSPECTED 1

Accession For	
NTIS CRA&I	<input checked="" type="checkbox"/>
DTIC TAB	<input type="checkbox"/>
Unannounced	<input checked="" type="checkbox"/>
Justification _____	
By _____	
Distribution /	
Availability Codes	
Dist	Avail and/or Special
A-1	

TABLE OF CONTENTS

I.	INTRODUCTION	1
	A. BACKGROUND	1
	B. PURPOSE	4
II.	GOVERNING EQUATIONS	6
	A. CONTINUITY EQUATION	6
	B. MOMENTUM EQUATION	6
	C. ENERGY EQUATION	7
	D. TURBULENCE MODEL	9
	E. TRANSFORMATION TO GENERALIZED COORDINATES . . .	11
	F. THIN LAYER NAVIER STOKES EQUATIONS	13
III.	SOLUTION METHODS	15
	A. ZONAL GRID GENERATION	15
	B. NUMERICAL SCHEME	16
	C. BOUNDARY CONDITIONS	18
IV.	RESULTS AND DISCUSSION	22
	A. STEADY STATE SOLUTIONS	22
	1. Inviscid Test Cases	22
	a. Case 1. Baseline Grid: 81x40 Inner and 81x22 Outer . . .	22
	b. Case 2. Baseline Inner Grid With a 41x22 Outer Grid . .	25
	c. Case 3. Overlap Boundary Set to 1 Chord Length Away From Body	27
	d. Case 4. Overlap Boundary Set to .75 Chord Length Away From Airfoil	29

e.	Case 5. Grid With Oval Interface	31
f.	Case 6. Baseline Grid With Half the Radial Grid Points On Outer Grid	34
2.	Viscous Test Case	36
B.	RAMP MOTION SOLUTION	43
1.	Boundary Layer Comparisons For Ramp Motion	51
2.	Computed Ramp Flow Details	57
C.	OSCILLATORY MOTION SOLUTION	121
V.	CONCLUSIONS	125
	REFERENCES	127
	INITIAL DISTRIBUTION LIST	130

LIST OF TABLES

4.1	TABLE OF GRID DENSITIES USED TO COMPUTE INVISCID SOLUTIONS.	23
-----	---	----

LIST OF FIGURES

4.1	Case 1. Computed Pressure Coefficient Using Baseline Grid	23
4.2	Case 1. Baseline Grid	24
4.3	Case 2. Computed Pressure Coefficient with the Outer Grid Having Half the Circumferential Resolution of Baseline Grid	25
4.4	Case 2. Baseline Grid with Outer Grid Halved	26
4.5	Case 3. Computed Pressure Coefficient For the Overlap Boundary Set to One Chord Length Away From The Airfoil	27
4.6	Case 3. Grid With Overlap Boundary Set to One Chord Length Away From Body.	28
4.7	Case 4. Computed Pressure Coefficient for Inner Grid Radius Set Equal to .75 Chord Lengths Away From The Airfoil	29
4.8	Case 4. Grid With Overlap Boundary Set to .75 Chord Lengths Away From Airfoil	30
4.9	Case 5. Computed Pressure Coefficient Using the Oval Grid	31
4.10	Case 5. Grid With Oval Interface	32
4.11	Case 5. Mach Contours for Oval Grid	33
4.12	Case 6. Computed Pressure Coefficients Using a Grid With Half the Radial Resolution of the Baseline Grid	34
4.13	Case 6. Grid With Half the Radial Resolution of the Baseline Grid	35
4.14	Viscous Grid: 181×56 Inner and 181×26 Outer	37
4.15	Steady Viscous Pressure Coefficient, $\alpha = 3.27^\circ$	38
4.16	Steady Viscous Pressure Coefficient, $\alpha = 4.97^\circ$	38
4.17	Steady Viscous Pressure Coefficient, $\alpha = 6.69^\circ$	39

4.18 Steady Viscous Pressure Coefficient, $\alpha = 7.54^\circ$	39
4.19 Steady Viscous Pressure Coefficient, $\alpha = 8.38^\circ$	40
4.20 Steady Viscous Pressure Coefficient, $\alpha = 9.27^\circ$	40
4.21 Steady Viscous Pressure Coefficient, $\alpha = 10.12^\circ$	41
4.22 Steady Viscous Pressure Coefficient, $\alpha = 10.99^\circ$	41
4.23 Steady Viscous Pressure Coefficient, $\alpha = 11.9^\circ$	42
4.24 Comparison of the Measured and Computed Lift for the Ramp Motion	43
4.25 Ramp Motion Pressure Coefficient at $\alpha = 1.86^\circ$	44
4.26 Ramp Motion Pressure Coefficient at $\alpha = 2.94^\circ$	44
4.27 Ramp Motion Pressure Coefficient at $\alpha = 4.14^\circ$	45
4.28 Ramp Motion Pressure Coefficient at $\alpha = 4.87^\circ$	45
4.29 Ramp Motion Pressure Coefficient at $\alpha = 5.85^\circ$	46
4.30 Ramp Motion Pressure Coefficient at $\alpha = 6.72^\circ$	46
4.31 Ramp Motion Pressure Coefficient at $\alpha = 8.02^\circ$	47
4.32 Ramp Motion Pressure Coefficient at $\alpha = 8.91^\circ$	47
4.33 Ramp Motion Pressure Coefficient at $\alpha = 9.85^\circ$	48
4.34 Ramp Motion Pressure Coefficient at $\alpha = 10.80^\circ$	48
4.35 Ramp Motion Pressure Coefficient at $\alpha = 11.77^\circ$	49
4.36 Ramp Motion Pressure Coefficient at $\alpha = 12.84^\circ$	49
4.37 Ramp Motion Pressure Coefficient at $\alpha = 13.89^\circ$	50
4.38 Ramp Motion Pressure Coefficient at $\alpha = 15.55^\circ$	50
4.39 Computed Boundary Layer Comparison at $x/c = 50\%$, $\alpha = 2.94^\circ$. .	52
4.40 Computed Boundary Layer Comparison at $x/c = 90\%$, $\alpha = 2.94^\circ$. .	52
4.41 Computed Boundary Layer Comparison at $x/c = 50\%$, $\alpha = 5.85^\circ$. .	53
4.42 Computed Boundary Layer Comparison at $x/c = 90\%$, $\alpha = 5.85^\circ$. .	53
4.43 Computed Boundary Layer Comparison at $x/c = 50\%$, $\alpha = 8.91^\circ$. .	54

4.44	Computed Boundary Layer Comparison at $x/c = 90\%$, $\alpha = 8.91^\circ$. . .	54
4.45	Computed Boundary Layer Comparison at $x/c = 50\%$, $\alpha = 11.77^\circ$. .	55
4.46	Computed Boundary Layer Comparison at $x/c = 90\%$, $\alpha = 11.77^\circ$. .	55
4.47	Computed Boundary Layer Comparison at $x/c = 50\%$, $\alpha = 15.55^\circ$. .	56
4.48	Computed Boundary Layer Comparison at $x/c = 90\%$, $\alpha = 15.55^\circ$. .	56
4.49	Ramp Motion Flow Details, $M_\infty = .3$, $k = .0127$, $Re = 2.7 \times 10^6$, $\alpha = 1.86^\circ$	59
4.50	Ramp Motion Flow Details, $M_\infty = .3$, $k = .0127$, $Re = 2.7 \times 10^6$, $\alpha = 2.94^\circ$	60
4.51	Ramp Motion Flow Details, $M_\infty = .3$, $k = .0127$, $Re = 2.7 \times 10^6$, $\alpha = 4.14^\circ$	61
4.52	Ramp Motion Flow Details, $M_\infty = .3$, $k = .0127$, $Re = 2.7 \times 10^6$, $\alpha = 5.85^\circ$	62
4.53	Ramp Motion Flow Details, $M_\infty = .3$, $k = .0127$, $Re = 2.7 \times 10^6$, $\alpha = 6.72^\circ$	63
4.54	Ramp Motion Flow Details, $M_\infty = .3$, $k = .0127$, $Re = 2.7 \times 10^6$, $\alpha = 8.02^\circ$	64
4.55	Ramp Motion Flow Details, $M_\infty = .3$, $k = .0127$, $Re = 2.7 \times 10^6$, $\alpha = 8.91^\circ$	65
4.56	Ramp Motion Flow Details, $M_\infty = .3$, $k = .0127$, $Re = 2.7 \times 10^6$, $\alpha = 9.85^\circ$	66
4.57	Ramp Motion Flow Details, $M_\infty = .3$, $k = .0127$, $Re = 2.7 \times 10^6$, $\alpha = 10.80^\circ$	67
4.58	Ramp Motion Flow Details, $M_\infty = .3$, $k = .0127$, $Re = 2.7 \times 10^6$, $\alpha = 11.77^\circ$	68

4.59 Ramp Motion Flow Details, $M_\infty = .3$, $k = .0127$, $Re = 2.7 \times 10^6$, $\alpha = 12.84^\circ$	69
4.60 Ramp Motion Flow Details, $M_\infty = .3$, $k = .0127$, $Re = 2.7 \times 10^6$, $\alpha = 13.89^\circ$	70
4.61 Ramp Motion Flow Details, $M_\infty = .3$, $k = .0127$, $Re = 2.7 \times 10^6$, $\alpha = 15.55^\circ$	71
4.62 Ramp Motion Flow Details, $M_\infty = .3$, $k = .0127$, $Re = 2.7 \times 10^6$, $\alpha = 16.00^\circ$	72
4.63 Ramp Motion Flow Details, $M_\infty = .3$, $k = .0127$, $Re = 2.7 \times 10^6$, $\alpha = 16.50^\circ$	73
4.64 Ramp Motion Flow Details, $M_\infty = .3$, $k = .0127$, $Re = 2.7 \times 10^6$, $\alpha = 17.00^\circ$	74
4.65 Ramp Motion Flow Details, $M_\infty = .3$, $k = .0127$, $Re = 2.7 \times 10^6$, $\alpha = 17.50^\circ$	75
4.66 Ramp Motion Flow Details, $M_\infty = .3$, $k = .0127$, $Re = 2.7 \times 10^6$, $\alpha = 18.00^\circ$	76
4.67 Ramp Motion Flow Details, $M_\infty = .3$, $k = .0127$, $Re = 2.7 \times 10^6$, $\alpha = 18.50^\circ$	77
4.68 Ramp Motion Flow Details, $M_\infty = .3$, $k = .0127$, $Re = 2.7 \times 10^6$, $\alpha = 19.00^\circ$	78
4.69 Ramp Motion Flow Details, $M_\infty = .3$, $k = .0127$, $Re = 2.7 \times 10^6$, $\alpha = 19.50^\circ$	79
4.70 Ramp Motion Flow Details, $M_\infty = .3$, $k = .0127$, $Re = 2.7 \times 10^6$, $\alpha = 20.00^\circ$	80
4.71 Ramp Motion Flow Details, $M_\infty = .3$, $k = .0127$, $Re = 2.7 \times 10^6$, $\alpha = 20.50^\circ$	81

4.72 Ramp Motion Flow Details, $M_\infty = .3$, $k = .0127$, $Re = 2.7 \times 10^6$, $\alpha = 21.00^\circ$	82
4.73 Ramp Motion Flow Details, $M_\infty = .3$, $k = .0127$, $Re = 2.7 \times 10^6$, $\alpha = 21.50^\circ$	83
4.74 Ramp Motion Flow Details, $M_\infty = .3$, $k = .0127$, $Re = 2.7 \times 10^6$, $\alpha = 22.00^\circ$	84
4.75 Ramp Motion Flow Details, $M_\infty = .3$, $k = .0127$, $Re = 2.7 \times 10^6$, $\alpha = 22.50^\circ$	85
4.76 Ramp Motion Flow Details, $M_\infty = .3$, $k = .0127$, $Re = 2.7 \times 10^6$, $\alpha = 23.00^\circ$	86
4.77 Ramp Motion Flow Details, $M_\infty = .3$, $k = .0127$, $Re = 2.7 \times 10^6$, $\alpha = 23.50^\circ$	87
4.78 Ramp Motion Flow Details, $M_\infty = .3$, $k = .0127$, $Re = 2.7 \times 10^6$, $\alpha = 24.00^\circ$	88
4.79 Ramp Motion Flow Details, $M_\infty = .3$, $k = .0127$, $Re = 2.7 \times 10^6$, $\alpha = 24.50^\circ$	89
4.80 Ramp Motion Flow Details, $M_\infty = .3$, $k = .0127$, $Re = 2.7 \times 10^6$, $\alpha = 25.00^\circ$	90
4.81 Ramp Motion Flow Details, $M_\infty = .3$, $k = .0127$, $Re = 2.7 \times 10^6$, $\alpha = 25.50^\circ$	91
4.82 Ramp Motion Flow Details, $M_\infty = .3$, $k = .0127$, $Re = 2.7 \times 10^6$, $\alpha = 26.00^\circ$	92
4.83 Ramp Motion Flow Details, $M_\infty = .3$, $k = .0127$, $Re = 2.7 \times 10^6$, $\alpha = 26.50^\circ$	93
4.84 Ramp Motion Flow Details, $M_\infty = .3$, $k = .0127$, $Re = 2.7 \times 10^6$, $\alpha = 27.00^\circ$	94

4.85 Ramp Motion Flow Details, $M_\infty = .3$, $k = .0127$, $Re = 2.7 \times 10^6$, $\alpha = 27.50^\circ$	95
4.86 Ramp Motion Flow Details, $M_\infty = .3$, $k = .0127$, $Re = 2.7 \times 10^6$, $\alpha = 28.00^\circ$	96
4.87 Ramp Motion Flow Details, $M_\infty = .3$, $k = .0127$, $Re = 2.7 \times 10^6$, $\alpha = 28.50^\circ$	97
4.88 Ramp Motion Flow Details, $M_\infty = .3$, $k = .0127$, $Re = 2.7 \times 10^6$, $\alpha = 29.00^\circ$	98
4.89 Ramp Motion Flow Details, $M_\infty = .3$, $k = .0127$, $Re = 2.7 \times 10^6$, $\alpha = 29.50^\circ$	99
4.90 Ramp Motion Flow Details, $M_\infty = .3$, $k = .0127$, $Re = 2.7 \times 10^6$, $\alpha = 30.00^\circ$	100
4.91 Ramp Motion Flow Details, $M_\infty = .3$, $k = .0127$, $Re = 2.7 \times 10^6$, $\alpha = 31.00^\circ$	101
4.92 Ramp Motion Flow Details, $M_\infty = .3$, $k = .0127$, $Re = 2.7 \times 10^6$, $\alpha = 32.00^\circ$	102
4.93 Ramp Motion Flow Details, $M_\infty = .3$, $k = .0127$, $Re = 2.7 \times 10^6$, $\alpha = 33.00^\circ$	103
4.94 Ramp Motion Flow Details, $M_\infty = .3$, $k = .0127$, $Re = 2.7 \times 10^6$, $\alpha = 34.00^\circ$	104
4.95 Ramp Motion Flow Details, $M_\infty = .3$, $k = .0127$, $Re = 2.7 \times 10^6$, $\alpha = 35.00^\circ$	105
4.96 Ramp Motion Flow Details, $M_\infty = .3$, $k = .0127$, $Re = 2.7 \times 10^6$, $\alpha = 36.00^\circ$	106
4.97 Ramp Motion Flow Details, $M_\infty = .3$, $k = .0127$, $Re = 2.7 \times 10^6$, $\alpha = 37.00^\circ$	107

4.98 Ramp Motion Flow Details, $M_\infty = .3$, $k = .0127$, $Re = 2.7 \times 10^6$, $\alpha = 38.00^\circ$.	108
4.99 Ramp Motion Flow Details, $M_\infty = .3$, $k = .0127$, $Re = 2.7 \times 10^6$, $\alpha = 39.00^\circ$.	109
4.100 Ramp Motion Flow Details, $M_\infty = .3$, $k = .0127$, $Re = 2.7 \times 10^6$, $\alpha = 40.00^\circ$.	110
4.101 Ramp Motion Flow Details, $M_\infty = .3$, $k = .0127$, $Re = 2.7 \times 10^6$, $\alpha = 41.00^\circ$.	111
4.102 Ramp Motion Flow Details, $M_\infty = .3$, $k = .0127$, $Re = 2.7 \times 10^6$, $\alpha = 42.00^\circ$.	112
4.103 Ramp Motion Flow Details, $M_\infty = .3$, $k = .0127$, $Re = 2.7 \times 10^6$, $\alpha = 43.00^\circ$.	113
4.104 Ramp Motion Flow Details, $M_\infty = .3$, $k = .0127$, $Re = 2.7 \times 10^6$, $\alpha = 44.00^\circ$.	114
4.105 Ramp Motion Flow Details, $M_\infty = .3$, $k = .0127$, $Re = 2.7 \times 10^6$, $\alpha = 45.00^\circ$.	115
4.106 Ramp Motion Flow Details, $M_\infty = .3$, $k = .0127$, $Re = 2.7 \times 10^6$, $\alpha = 46.00^\circ$.	116
4.107 Ramp Motion Flow Details, $M_\infty = .3$, $k = .0127$, $Re = 2.7 \times 10^6$, $\alpha = 47.00^\circ$.	117
4.108 Ramp Motion Flow Details, $M_\infty = .3$, $k = .0127$, $Re = 2.7 \times 10^6$, $\alpha = 48.00^\circ$.	118
4.109 Ramp Motion Flow Details, $M_\infty = .3$, $k = .0127$, $Re = 2.7 \times 10^6$, $\alpha = 49.00^\circ$.	119
4.110 Ramp Motion Flow Details, $M_\infty = .3$, $k = .0127$, $Re = 2.7 \times 10^6$, $\alpha = 50.00^\circ$.	120

4.111	Comparison of Measured and Computed Lift for Oscillatory Test Case	121
4.112	Comparison of Measured and Computed Moment Coefficient for Oscillatory Test Case	122
4.113	Comparison of the Measured and Computed Unsteady Surface Pressure Coefficient of Oscillatory Motion, $\alpha = 5.95^\circ$ upstroke.	123
4.114	Comparison of the Measured and Computed Unsteady Surface Pressure Coefficient of Oscillatory Motion, $\alpha = 6.97^\circ$ upstroke.	123
4.115	Comparison of the Measured and Computed Unsteady Surface Pressure Coefficient of Oscillatory Motion, $\alpha = 6.57^\circ$ downstroke.	124
4.116	Comparison of the Measured and Computed Unsteady Surface Pressure Coefficient of Oscillatory Motion, $\alpha = 5.95^\circ$ downstroke.	124

ACKNOWLEDGMENT

First I would like to thank Dr. Bob Wood and Jerry Higman for their efforts in persuading me to return to school and work towards a masters degree. If it were not for them, I would never have started this work.

A big thank you to fellow staff members, Marla Convington, Rosemarie Tantillo and Jirophon Gerrard. They helped me balance my workload so that I could take classes during the workday.

I would also like to acknowledge Dr. Ismial Tuncer for his inputs to this thesis and his excellent plotting program which I used to generate my contour plots. A special thanks to Dr. Garth Hobson for his almost daily inputs. Dr. Hobson seemed to always be in the Advanced Computing Lab when I had a question on computational fluid dynamics or I needed someone to bounce some ideas off of. I am also especially grateful to the following graduates of NPS: Ray Coutley, Steve Grosheymer, Huemon Kwon, Anthony Wang and Jeff Clarkson. All of whom through their hard work layed down the foundation so that this work could be accomplished.

Many thanks to Dr. John Ekaterinaris, one of my two thesis advisors. None of this work could have been completed without the countless hours he spent developing the code that I used for my research. He also spent many hours teaching me to use all of the software available at NASA Ames Research Center. He deserves much of the credit for this thesis. Heart felt thanks to my other thesis advisor, Prof. Max Platzer. Prof. Platzer and I made an agreement in which I would teach him UNIX, and he would teach me CFD. Over the course of this study, he has taught me so much more than just CFD. In working with him, I have grown both professionally and personally.

I also want to thank Dr. Ramesh Kolar for his encouragements. He helped me to continue with this thesis at times when I would have given up.

Finally I want to thank my wife Sue for the love, patience and understanding she has shown me while I completed this research. This thesis is dedicated to her.

I. INTRODUCTION

A. BACKGROUND

Investigation of steady and unsteady flowfields over airfoils is an active area of numerical and experimental research. Unsteady pitch-up motion of airfoils alters significantly the aerodynamic characteristics of lifting surfaces. Pitch-up motion of an airfoil produces lift augmentation and delay of stall to higher angles of incidence compared to airfoils held at a steady incidence. Understanding the mechanisms that cause the dynamic lift development is a subject of interest in both theoretical and applied research.

A comprehensive explanation of the dynamic lift phenomenon is given by Tyler and Leishman [Ref. 1]. To briefly summarize, unsteady airfoil motion tends to maintain high lift to higher angles-of-attack, because the unsteady flow causes a time delay in the build-up of the lift force and the adverse pressure gradient. The unsteady motion also gives the airfoil a virtual camber which decreases the leading edge pressure and pressure gradients. Depending on the flow conditions, as the airfoil begins to stall, a vortex forms at the leading edge which grows with time which is eventually shed downstream in the wake. This vortex shedding phenomenon alters the chordwise pressure distribution on the upper surface of the airfoil resulting in higher maximum lift coefficients. Sometimes, however, only a recirculating flow is observed at the airfoil trailing edge. As the pitch-up motion progresses the recirculating region extends upstream towards the leading edge and eventually a vortex is formed at the trailing edge.

Rotary wing and fixed wing aircraft designers can enhance the performance of the aircraft by taking advantage of the dynamic lift concept. However, the resulting undesirable pitching moment variations have deprived helicopters and airplanes of the benefits of dynamic lift [Ref. 2]. Carr [Ref. 3] gives a comprehensive review of the progress that has been made in the study of the dynamic stall phenomenon.

Experimental work on steady transonic flow on airfoils was conducted by McDewitt and Okuno [Ref. 4]. These data cover a wide range of flow conditions and can be used for steady code validation. One of the pioneering experimental works on unsteady airfoil flows was conducted by McCroskey et al [Ref. 5]. In their experiments, unsteady dynamic effects for two-dimensional airfoil flows were studied for the first time in conjunction with flows over helicopter blades. They showed the effects of unsteady lift and pitching moment on the retreating rotor blades. Their research also showed that unsteady motion parameters such as reduced frequency, appeared to be more important than airfoil shape in determining the dynamic stall airloads. Benchmark experimental data of oscillating and pitching airfoils was also collected by Landon [Ref. 6]. The experimental data of references [5] and [6] gives enough qualitative information for unsteady code validation. Recent experiments with oscillating airfoils, performed by Chandrasekhara and Brydges [Ref. 7], have shown definitively that at subsonic Mach numbers the unsteady flow in the vicinity of the leading edge can reach supersonic speeds and generate shocks.

Along with all the experimental studies being conducted, a great effort is also underway to compute unsteady viscous flows. Developments of numerical methods for the Navier-Stokes equations [Refs. 8, 9, 10] during the past few years provide new tools for the investigation and prediction of airfoil flows. In this investigation the compressible thin layer Navier-Stokes equations are solved using a zonal grid approach. The objective is to develop a computationally efficient method to study

two-dimensional unsteady flows. This will be accomplished by developing a solution procedure for two grids, an inner viscous grid around the solid body, and an outer grid which is coarser representing the outer flow field. The inner grid is free to rotate to any angle of attack, and the outer grid remains stationary.

The idea of moving meshes and dynamic meshes is not new. The dynamic and adaptive grid solution method refers to computational grids which are coupled to the physical problem that is being solved. An adaptive solution procedure with grid points that continually move during the solution process in order to resolve the developing gradients has been shown [Ref. 11]. A dynamic type of mesh has been applied by Rumsey and Anderson [Ref. 12] to simulate aileron buzz using the thin layer Navier-Stokes equations.

The idea of overlapped or patched grid schemes was used by Rubbert and Lee [Ref. 13] with the limitation that the grid lines at the boundaries were continuous. Benek et al [Ref. 14] developed the "CHIMERA" approach for two-dimensional embedded and overlapping grids. They demonstrated that the grid lines at the overlapped boundaries did not have to be continuous, and that the flow quantities could be successfully interpolated. The "CHIMERA" approach was later extended to three dimensions by Benek et al [Ref. 15]. Rai [Ref. 16] developed a technique for independent zonal grids where the flow variables were interpolated across the zonal interface. Chesshire and Henshaw [Ref. 17] developed a methodology for solving the steady compressible Navier-Stokes equations using multiple overlapped grids. Their methodology was demonstrated by solving the governing equations on a composite grid that was comprised of an airfoil grid, a leading-edge flap grid, a trailing-edge flap grid and a grid for the outer flowfield. Chyu and Davis [Ref. 18] investigated unsteady transonic flow using a moving airfoil grid. They developed stationary computational grids around the airfoil at its lowest and highest angles of attack, and then

interpolated a new grid as the airfoil oscillated to intermediate angles-of-attack. Reu and Ying [Ref. 19] developed a composite grid approach to study the flow about pitching airfoils in a wind tunnel. Their approach consisted of a structured inner grid and an unstructured grid for the outer flowfield.

Unsteady problems have also been solved by oscillating the incoming flow, as opposed to moving the grid. However, this method does not work if a solution is sought for two or more objects, such as a wing tail combination or a canard wing in relative motion to each other.

B. PURPOSE

In this work, unsteady compressible flows are investigated using a numerical technique which is applied to zonal meshes. The governing equations are solved on multiple computational grids, where one of the grids is free to move in unison with the solid boundary and the other grid is fixed. The meshes overlap at the zonal interface. The scheme that is developed is similar to the "CHIMERA" scheme mentioned previously, but we impose the restriction of a circular shape on the zonal interface.

The new approach developed in this study is more computationally efficient compared to previous schemes used to study unsteady flows. The zonal grid approach avoids the need to regenerate or interpolate entire grids at every angle of attack. The zonal interface is in a known position; therefore the entire flowfield does not need to be searched. In addition, since the outer grid remains stationary, the metric terms do not need to be recomputed at each time step. Another advantage is that the zonal interface is circular; therefore the flow variables are interpolated in the circumferential direction only. The zonal grid approach also allows for the application of different solution methods to the inner and outer grids. For example, viscous solution methods

near the solid body and an inviscid method on the outer mesh can be implemented.

The primary objective of this investigation is to develop and test the zonal grid methodology. The space discretization is based on Osher's [Ref. 26] upwind method. An implicit scheme is used for time integration. An advantage of upwind schemes is that they are naturally dissipative and no explicit artificial dissipation is required.

In order to meet our goal, a procedure for generating zonal grids was developed, along with the zonal flow solver. The effect of grid resolution on the accuracy of solutions was studied first for steady flows and the solutions were compared to experimental data collected by Harris [Ref. 21]. The unsteady results were validated using the experiments by Landon. The dependence of the solution on the location of the overlapped zonal region was examined. Viscous steady state solutions were computed and compared to experimental data. Finally, unsteady flows were investigated by computing solutions for airfoils in ramp and oscillatory motion. The ramp motion was started at zero angle of incidence, and ramped up to 30 degrees. The computed pressure coefficients were verified by comparing with available experimental pressure distributions. The boundary layers computed for this case were also compared to an interactive boundary layer code [Ref. 22]. The oscillatory test case was verified by comparing the computed pressure coefficients with experimental data. This approach and the computed results are described in the following chapters.

II. GOVERNING EQUATIONS

In order to compute compressible viscous fluid flow around a body, the continuity, momentum and energy equations must be solved simultaneously. The vector and the conservation-law form of the compressible Reynolds-averaged Navier-Stokes equation is presented. A detailed derivation can be found in [Ref. 23]

A. CONTINUITY EQUATION

The continuity equation expresses the conservation of mass law applied to a fluid passing through a control volume fixed in space

$$\frac{\partial \rho}{\partial t} + (\nabla \cdot \rho \mathbf{V}) = 0 \quad (2.1)$$

here ρ is the fluid density and \mathbf{V} is the fluid velocity. Equation 2.1 states that the net mass flux through a control volume bounding surface must be equal to the time rate of change of the mass inside the control volume. In a two-dimensional Cartesian coordinate system this equation reads

$$\frac{\partial \rho}{\partial t} + \frac{\partial}{\partial x}(\rho u) + \frac{\partial}{\partial z}(\rho w) = 0 \quad (2.2)$$

where u and w are velocity components along the x and z directions, respectively.

B. MOMENTUM EQUATION

The momentum equation expresses Newton's second law as applied to a fluid element passing through a control volume fixed in space. The momentum equation is:

$$\frac{\partial}{\partial t}(\rho \mathbf{V}) + \nabla \cdot \rho \mathbf{V} \mathbf{V} = \rho \mathbf{f} + \nabla \cdot \mathbf{\Pi}_{ij} \quad (2.3)$$

The first term in equation 2.3 represents the time rate of change of momentum per unit volume in the control volume. The second term represents the moment flux through the bounding surface of the control volume. f is the body force per unit volume and Π_{ij} is the stress tensor given by

$$\Pi_{ij} = -p\delta_{ij} + \mu \left[\frac{\partial u_i}{\partial x_j} - \frac{2}{3}\delta_{ij} \frac{\partial u_k}{\partial x_k} \right] \quad (2.4)$$

where $i, j, k = 1, 2, 3$ and δ_{ij} is the Kronecker delta.

By substituting equation 2.4 into equation 2.3 and expanding equation 2.3 for a two-dimensional Cartesian coordinate system obtain

$$\rho \frac{Du}{Dt} = \rho f_x - \frac{\partial p}{\partial x} + \frac{\partial}{\partial x} \left[\frac{2}{3}\mu \left(2\frac{\partial u}{\partial x} - \frac{\partial w}{\partial z} \right) \right] + \frac{\partial}{\partial z} \left[\mu \left(\frac{\partial w}{\partial x} + \frac{\partial u}{\partial z} \right) \right] \quad (2.5)$$

$$\rho \frac{Dw}{Dt} = \rho f_z - \frac{\partial p}{\partial z} + \frac{\partial}{\partial z} \left[\frac{2}{3}\mu \left(2\frac{\partial w}{\partial z} - \frac{\partial u}{\partial x} \right) \right] + \frac{\partial}{\partial x} \left[\mu \left(\frac{\partial w}{\partial x} + \frac{\partial u}{\partial z} \right) \right]$$

Equations 2.5 are known as the Navier-Stokes equations for two-dimensional flow.

C. ENERGY EQUATION

The energy equation is derived by applying the first law of thermodynamics (*rate of change of energy = net heat flux into particle + rate of work done on particle.*)

$$\begin{aligned} \frac{\partial e}{\partial t} - \frac{\partial Q}{\partial t} - \rho(f_x u + f_z w) &+ \frac{\partial}{\partial x}(eu + pu - u\tau_{xx} - w\tau_{xz} + Q_x) \\ &+ \frac{\partial}{\partial z}(ew + pw - w\tau_{zz} - u\tau_{xz} + Q_z) = 0 \end{aligned}$$

where e is the total energy per unit volume and Q is the heat addition per unit volume.

The above equations can be rewritten in non-dimensionalized vector form as

$$\frac{\partial \mathbf{Q}}{\partial t} + \frac{\partial \mathbf{F}}{\partial x} + \frac{\partial \mathbf{G}}{\partial z} = \frac{1}{Re} \left(\frac{\partial \mathbf{F}_v}{\partial x} + \frac{\partial \mathbf{G}_v}{\partial z} \right) \quad (2.6)$$

where

$$\mathbf{Q} = \begin{bmatrix} \rho \\ \rho u \\ \rho w \\ e \end{bmatrix}$$

$$\mathbf{F} = \begin{bmatrix} \rho u \\ \rho u^2 + p \\ \rho uw \\ (e + p)u \end{bmatrix} \quad \mathbf{G} = \begin{bmatrix} \rho w \\ \rho uw \\ \rho w^2 + p \\ (e + p)w \end{bmatrix}$$

$$\mathbf{F}_v = \begin{bmatrix} 0 \\ \tau_{xx} \\ \tau_{xz} \\ f_4 \end{bmatrix} \quad \mathbf{G}_v = \begin{bmatrix} 0 \\ \tau_{xz} \\ \tau_{zz} \\ g_4 \end{bmatrix}$$

Here,

$$\tau_{xx} = \frac{4}{3}\mu \left(u_x - \frac{1}{2}w_z \right)$$

$$\tau_{xz} = \mu (u_z + w_x)$$

$$\tau_{zz} = \frac{4}{3}\mu \left(w_z - \frac{1}{2}u_x \right)$$

$$f_4 = u\tau_{xx} + w\tau_{xz} + \frac{\mu}{\text{Pr}(\gamma - 1)}a_x^2$$

$$g_4 = u\tau_{xz} + w\tau_{zz} + \frac{\mu}{\text{Pr}(\gamma - 1)}a_z^2$$

$$\text{Re} = \frac{U_\infty L}{\nu}$$

where U_∞ is the free stream speed and L is a reference length. The pressure is related to u, w, ρ , and e by

$$p = (\gamma - 1)\left[e - \frac{1}{2}\rho(u^2 + w^2)\right]$$

In the above equations, the ratio of the specific heats, γ , is set equal to 1.4 and $a^2 = \gamma p / \rho$ is the local speed of sound.

The density is non-dimensionalized by the free stream density, ρ_∞ , the velocities are non dimensionalized by the free stream speed of sound, and the total energy is non dimensionalized by $\rho_\infty a_\infty^2$.

D. TURBULENCE MODEL

The Navier-Stokes equations can completely model fluid flow, however, in order to resolve turbulent scales at high Reynolds numbers and realistic geometries, very high grid densities are required. Therefore, present state-of-the-art algorithms and computer technology allows direct simulation of turbulent flows for only simple geometries and low Reynolds number flows which are of limited practical interest. In order to enable computation of turbulent flows for configurations, of practical interest, turbulence modeling is used. Turbulence models are implemented with the time-averaged forms of the Navier-Stokes equations.

Two widely used averaging procedures are the standard time averaging procedure for incompressible flow, and the mass-averaged approach for compressible flows [Ref. 24]. The time averaging procedure destroys high frequency information of the turbulence, but the unsteady mean flow information is preserved.

For the incompressible case, the randomly changing flow variables are replaced with their averages plus their fluctuations. For example, in the Cartesian coordinate system, the u velocity component is represented as $u = \bar{u} + u'$, where \bar{u} is the mean velocity and u' is the fluctuation about the mean. The governing equations are time averaged, and the average of the fluctuation terms is set equal to zero.

In the compressible flow case, the mass-weighted variable of the Favre averaging approach is used. In this case, u is represented as $u = \tilde{u} + u''$ where \tilde{u} is

$$\tilde{u} = \frac{\bar{\rho}u}{\bar{\rho}}$$

Here the time average of the doubly primed fluctuating quantities is not equal to zero. After the substitution is carried out for all of the fluctuating flow variables, the entire equation is time averaged. Next, all the time averaged terms that are doubly primed

and multiplied by density are defined to be zero. For example

$$\rho \bar{u}'' \equiv 0$$

The equations of mean motion resulting from the time averaging procedure have more unknowns than equations. This constitutes the closure problem of turbulence. In order to close these equations a turbulence model is used. Several models have been proposed, in this study.

The Baldwin-Lomax ($B-L$) turbulence model [Ref. 25] was used. This model is a two-layer eddy viscosity model which simulates the effect of turbulence in terms of the eddy viscosity coefficient μ_t . The term μ in the stress terms is replaced by $\mu + \mu_t$, and the μ/P_r in the heat flux terms is replaced with $\mu/P_r + \mu_t/P_{rt}$. The $B-L$ turbulence model is similar to the Cebeci-Smith turbulence model [Ref. 26], but it bypasses the need for finding the edge of the boundary layer by using vorticity instead of the boundary layer thickness. This model is adequate for flows which have mild pressure gradients, but it is not very suitable for highly separated flows. A complete description of the model is given in reference [25]. The basic equations of the model follow.

In the inner layer, the eddy viscosity is assumed to be proportional to the mixing length and vorticity, and in the outer layer it uses an exponentially decaying formula. The inner eddy viscosity is computed up to the point where it is equal to the outer eddy viscosity as shown below.

$$\mu_t = \begin{cases} (\mu_t)_{\text{inner}} & y \leq y_{\text{crossover}} \\ (\mu_t)_{\text{outer}} & y_{\text{crossover}} < y \end{cases} \quad (2.7)$$

where y is the normal distance from the wall and $y_{\text{crossover}}$ taken at its minimum value where it equals y . The inner eddy viscosity is given by:

$$(\mu_t)_{\text{inner}} = \rho l^2 |\omega|$$

where

$$l = \kappa y \left[1 - \exp\left(-\frac{y^+}{A^+}\right) \right]$$

$$|\omega| = \sqrt{\left(\frac{\partial w}{\partial x} - \frac{\partial u}{\partial z}\right)^2}$$

$$y^+ = \frac{\rho_w u_\tau y}{\mu_w}$$

A^+ is an experimentally determined damping constant, κ is the Von Karman constant

The outer eddy viscosity is given by

$$\mu_{\text{outer}} = \kappa C_{cp} \rho F(y)_{\text{WAKE}} F(y)_{\text{KLEB}}.$$

$F(y)_{\text{KLEB}}$ is the Klebanoff intermittency factor given by

$$F(y)_{\text{KLEB}} = \left[1 + 5.5 \left(\frac{C_{\text{KLEB}} y}{y_{\text{max}}} \right)^6 \right]^{-1}$$

κ and C_{cp} are constants. For boundary layers

$$F(y)_{\text{wake}} = y_{\text{max}} F_{\text{max}}.$$

For wakes and separated boundary layers

$$F(y)_{\text{wake}} = C_w k y_{\text{max}} \frac{u_{\text{DIF}}^2}{F_{\text{max}}}.$$

The quantity y_{max} is the value of y determined for the maximum value of F_{max} and

F_{max} is determined by

$$F(y) = y |\omega| \left[1 - \exp\left(-\frac{y^+}{A^+}\right) \right].$$

E. TRANSFORMATION TO GENERALIZED COORDINATES

In order to use an unweighted differencing scheme that facilitate the numerical implementation on body fitted coordinate systems suitable for complex configurations, the equations are transformed to a generalized coordinate system using the

following transformations

$$\xi = \xi(x, z); \quad \zeta = \zeta(x, z). \quad (2.8)$$

The above equations transform the governing equations from the physical domain to a body fitted coordinate system. The transformation is carried out by using the chain rule of partial differentiation

$$\frac{\partial}{\partial x} = \xi_x \frac{\partial}{\partial \xi} + \zeta_x \frac{\partial}{\partial \zeta}; \quad \frac{\partial}{\partial z} = \xi_z \frac{\partial}{\partial \xi} + \zeta_z \frac{\partial}{\partial \zeta} \quad (2.9)$$

For example, the continuity equation would be transformed in the following manner.

$$\frac{\partial \rho u}{\partial x} = \xi_x \frac{\partial \rho u}{\partial \xi} + \zeta_x \frac{\partial \rho v}{\partial \zeta}; \quad \frac{\partial \rho v}{\partial z} = \xi_z \frac{\partial \rho u}{\partial \xi} + \zeta_z \frac{\partial \rho v}{\partial \zeta} \quad (2.10)$$

ξ_x, ξ_z, ζ_x and ζ_z are known as the metrics. The metric terms can be determined in the following manner. First write the differential expressions for ξ and ζ

$$d\xi = \xi_x dx + \xi_z dz; \quad d\zeta = \zeta_x dx + \zeta_z dz \quad (2.11)$$

In matrix form the expressions become

$$\begin{bmatrix} d\xi \\ d\zeta \end{bmatrix} = \begin{bmatrix} \xi_x & \xi_z \\ \zeta_x & \zeta_z \end{bmatrix} \begin{bmatrix} dx \\ dz \end{bmatrix} \quad (2.12)$$

Next we write the differential expression for x and z

$$\begin{aligned} dx &= x_\xi d\xi + x_\zeta d\zeta \\ dz &= z_\xi d\xi + z_\zeta d\zeta \end{aligned} \quad (2.13)$$

In matrix form they become

$$\begin{bmatrix} dx \\ dz \end{bmatrix} = \begin{bmatrix} x_\xi & x_\zeta \\ z_\xi & z_\zeta \end{bmatrix} \begin{bmatrix} d\xi \\ d\zeta \end{bmatrix} \quad (2.14)$$

By comparing equations 2.12 and 2.14 we can write

$$\begin{bmatrix} x_\xi & x_\zeta \\ z_\xi & z_\zeta \end{bmatrix}^{-1} = \begin{bmatrix} \xi_x & \xi_z \\ \zeta_x & \zeta_z \end{bmatrix} \quad (2.15)$$

and solving for the metrics we get

$$\begin{aligned}\xi_x &= Jz_\zeta \\ \xi_z &= -Jx_\zeta \\ \zeta_x &= -Jz_\xi \\ \zeta_z &= Jz_\xi\end{aligned}\tag{2.16}$$

where

$$J = \frac{1}{\begin{vmatrix} x_\xi & x_\zeta \\ z_\xi & z_\zeta \end{vmatrix}}\tag{2.17}$$

The mapping from (x, z) to (ξ, ζ) is one to one if the Jacobian, J , is non singular.

F. THIN LAYER NAVIER STOKES EQUATIONS

In order to accurately calculate the normal gradients in the boundary layer, it is necessary to make the normal grid spacing very fine close to the solid surfaces. In the streamwise direction the flow gradients are not large and no fine grid spacing is required. As a result the grid cells near the body have a very high aspect ratio. With this type of grid, existing gradients in the streamwise direction are not fully resolved. In order to facilitate the numerical implementation of the thin layer approximation is employed by retaining only the viscous derivatives normal to the body. The thin layer Navier-Stokes equations transformed into a generalized curvilinear system in vector form are

$$\frac{\partial \hat{\mathbf{Q}}}{\partial t} + \frac{\partial \hat{\mathbf{F}}}{\partial \xi} + \frac{\partial \hat{\mathbf{G}}}{\partial \zeta} = \frac{1}{Re} \left[\frac{\partial \hat{\mathbf{S}}}{\partial \zeta} \right]$$

where

$$\hat{\mathbf{Q}} = \frac{1}{J} \begin{bmatrix} \rho \\ \rho u \\ \rho w \\ e \end{bmatrix}$$

$$\hat{\mathbf{F}} = \frac{1}{J} \begin{bmatrix} \rho U \\ \rho u U + \xi_x p \\ \rho w U + \xi_x p \\ (e + p)U - \xi_t p \end{bmatrix}$$

$$\hat{\mathbf{G}} = \frac{1}{J} \begin{bmatrix} \rho W \\ \rho u W + \zeta_x p \\ \rho w W + \zeta_z p \\ (e + p)W - \zeta_t p \end{bmatrix}$$

The viscous flux term is transformed as

$$\hat{\mathbf{S}} = \frac{1}{J} \begin{bmatrix} 0 \\ \mu m_1 u_\zeta + (\mu/3)m_2 \zeta_x \\ \mu m_1 w_\zeta + (\mu/3)m_2 \zeta_z \\ \mu m_1 m_3 + (\mu/3)m_2 m_4 \end{bmatrix}$$

where

$$\begin{aligned} m_1 &= \zeta_x^2 + \zeta_z^2 \\ m_2 &= \zeta_x u_\zeta + \zeta_z w_\zeta \\ m_3 &= \frac{1}{2} \frac{\partial}{\partial \xi} \frac{(u^2 + w^2)}{2} + \frac{1}{Pr(\gamma-1)} \frac{\partial a^2}{\partial \zeta} \\ m_4 &= \zeta_x u + \zeta_z w. \end{aligned} \tag{2.18}$$

U and W are the contravariant velocity components. These velocity components are normal and parallel to the constant ξ and ζ surfaces, respectively.

$$U = \xi_t + \xi_x u + \xi_z w$$

$$W = \zeta_t + \zeta_x u + \zeta_z w$$

III. SOLUTION METHODS

A. ZONAL GRID GENERATION

The zonal grids were generated using a software package called GRAPE2D, developed at NASA Ames Research Center by Reese L. Sorenson [Ref. 27]. GRAPE2D generates field grids by solving the following set of elliptic Poisson equations:

$$\begin{aligned}\xi_{xx} - \xi_{zz} &= P \\ \eta_{xx} - \eta_{zz} &= Q\end{aligned}\tag{3.1}$$

GRAPE2D was used to generate the inner and outer grid separately. In generating the inner grid, the number of circumferential and radial grid points, the spacing at the body surface, and the radius and shape of the outer boundary were specified. Once the inner grid was generated, the outer boundary of the inner grid was used as the inner boundary for the outer grid.

Due to the placement of the reference axis at the quarter chord of the airfoil, the grid spacing in front of the airfoil is larger than aft of the airfoil. This causes a problem in specifying an initial grid spacing for the outer grid. In order to obtain the smoothest overall transition from the inner grid to the outer grid, the starting spacing for the outer grid was obtained by averaging the minimum and maximum spacing at the outer boundary of the inner grid. The outer boundary of the outer grid was prescribed as a rectangular region, usually about six chord lengths away from the body.

The perfectly circular zonal boundary was accomplished by reading the overlapped regions x and z coordinates and finding an average radius which was measured from the center of the grid, regardless of the location of the inner body. Next, an arbitrary grid point was chosen to use as a reference point. Then an angle θ , θ

θ , was calculated which represented the angle between the reference grid point and the grid point under consideration. Then having the average radius and the angle θ for the grid points in the overlapped region, a new set of x and y coordinates was calculated using the following equations:

$$x = r \cos \theta, y = r \sin \theta \quad (3.2)$$

The overlapping of the two grids was performed by adding the next to last layer of grid points from the inner grid to the outer grid, and adding the second layer of grid points from the outer grid to the outer boundary of the inner grid. This resulted in an overlapped region of three grid points or two grid cells in the radial direction. The grid was also overlapped by a grid point in the circumferential direction.

B. NUMERICAL SCHEME

The numerical integration is performed using an upwind-biased, factorized, iterative, implicit numerical scheme [Ref. 20] given by

$$\begin{aligned} & \left[I + h_\xi (\nabla_\xi^b \tilde{A}_{i,k}^+ + \Delta_\xi^f \tilde{A}_{i,k}^-) \right]^p \times \\ & \left[I + h_\zeta (\nabla_\zeta^b \tilde{B}_{i,k}^+ + \Delta_\zeta^f \tilde{B}_{i,k}^- - Re^{-1} \delta_\zeta \tilde{M}_{i,k}) \right]^p \times (\tilde{Q}_{i,k}^{p+1} - \tilde{Q}_{i,k}^p) = \\ & - [(\tilde{Q}_{i,k}^p - \tilde{Q}_{i,k}^n) + h_\xi (\tilde{F}_{i+1/2,k}^p - \tilde{F}_{i-1/2,k}^p) \\ & + h_\zeta (\tilde{G}_{i,k+1/2}^p - \tilde{G}_{i,k-1/2}^p) - Re^{-1} h_\zeta (\tilde{S}_{i,k+1/2}^p - \tilde{S}_{i,k-1/2}^p)] \end{aligned} \quad (3.3)$$

In equation 3.3, $h_\xi = \Delta\tau/\Delta\xi$, etc., $\tilde{A}^\pm = (\partial\tilde{F}/\partial\tilde{Q})$, etc., are the flux Jacobian matrices, and Δ, ∇ , and δ are the forward, backward and central difference operators, respectively. The quantities $\tilde{F}_{i+1/2,k}$, $\tilde{G}_{i,k+1/2}$, and $\tilde{S}_{i,k+1/2}$ are numerical fluxes. The inviscid fluxes \hat{F} and \hat{G} are evaluated using Osher's upwinding scheme [Ref. 19]. The numerical fluxes for a third-order accurate scheme are given by

$$\begin{aligned} \hat{F}_{i+1/2,k} = & \tilde{F}_{i+1/2,k} + \frac{1}{6} \left[\Delta F_{i-1/2,k}^+ + 2\Delta F_{i+1/2,k}^+ \right] - \\ & \frac{1}{6} \left[\Delta F_{i+3/2,k}^- + 2\Delta F_{i+1/2,k}^- \right] = \tilde{F}(Q_{i,k}, Q_{i+1,k}) + \\ & \frac{1}{6} \left[\Delta F^+(Q_{i+1,k}, Q_{i,k}) + 2\Delta F^+(Q_{i,k}, Q_{i+1,k}) \right] - \\ & \frac{1}{6} \left[\Delta F^-(Q_{i,k}, Q_{i+1,k}) + 2\Delta F^-(Q_{i+1,k}, Q_{i,k}) \right] - \end{aligned} \quad (3.4)$$

Where \tilde{F} is the first-order numerical flux for the explicit Osher's scheme given by

$$\tilde{F}_{i+1/2,k} = \frac{1}{2} \left[F_{i,k} + F_{i+1,k} - \int_{Q_i}^{Q_{i+1}} \{F_q^+ - F_q^-\} dQ \right]$$

where $F_q = F_q^+ + F_q^-$, $F_q^\pm = \left(\frac{\partial F}{\partial Q}\right)^\pm$, and ΔF^\pm are the corrections to obtain a higher order accuracy. The Osher scheme evaluates the flux assuming a shock tube solution where F_q is piecewise continuous and yields good predictions of the flux, especially at supersonic Mach numbers. For the linearization of the left-hand side of Eq. 3.3, the flux Jacobian matrices A, B are evaluated by the Steger-Warming [Ref. 28] flux-vector splitting.

Time accuracy of the implicit numerical solution is obtained by performing Newton iteration to convergence for each time step. The approximation of \tilde{Q}^{n+1} at each subiteration is the quantity \tilde{Q}^p . When $p \geq 2$, during a given subiteration, $\tilde{Q}^p = \tilde{Q}^{n+1}$, but when $p = 1$ and no subiteration is performed, then $\tilde{Q}^p = \tilde{Q}^n$, and $\tilde{Q}^{p+1} = \tilde{Q}^{n+1}$. By subiterating to convergence, linearization and factorization errors are minimized, because the left-hand side of Eq. 3.3. can be driven to zero at each time step.

The linearization errors are eliminated by subiteration to convergence. Typically, two to three subiterations are sufficient to drop the residuals two orders of magnitude during the Newton iteration process.

High order accurate shock-capturing schemes have some limitations; they may select a nonphysical solution, they produce spurious oscillations and they may develop a nonlinear instability in nonsmooth and discontinuous flow regions. More appropriate high-order shock-capturing schemes, suitable for the computation of weak solutions are the TVD schemes, described in detail in [Ref. 29, 30]. In the present study, the Osher-Chakravarthy [Ref. 31] TVD scheme is used. This TVD scheme has flux limiters which impose constraints on the gradients of the fluxes. The flux-limited

values $\Delta \tilde{f}^\pm$ are computed from the unlimited fluxes Δf^\pm as follows

$$\begin{aligned}\Delta \tilde{f}_{i+3/2,k}^- &= \minmod \left[\Delta f_{i+3/2,k}^-, \beta \Delta f_{i+1/2,k}^- \right] \\ \Delta \tilde{f}_{i+1/2,k}^- &= \minmod \left[\Delta f_{i+1/2,k}^-, \beta \Delta f_{i+3/2,k}^- \right] \\ \Delta \tilde{f}_{i+1/2,k}^+ &= \minmod \left[\Delta f_{i+1/2,k}^+, \beta \Delta f_{i-1/2,k}^+ \right] \\ \Delta \tilde{f}_{i-1/2,k}^+ &= \minmod \left[\Delta f_{i-1/2,k}^+, \beta \Delta f_{i+1/2,k}^+ \right]\end{aligned}\tag{3.5}$$

where the *minmod* operator is defined by

$$\minmod[x, y] = \text{sign}(x) \times \max[0, \min\{|x|, y \text{sign}(x)\}]\tag{3.6}$$

The viscous fluxes $S_{i,k+1/2}$ are computed with central differences as follows

$$S_{i,k+1/2} = S[Q_{i,k+1/2}, (Q_\zeta)_{i,k+1/2}, \zeta_{i,k+1/2}]\tag{3.7}$$

$$Q_{i,k+1/2} = \frac{1}{2}(Q_{i,k} + Q_{i,k-1})\tag{3.8}$$

$$(Q_\zeta)_{i,k+1/2} = Q_{i,k+1} - Q_{i,k}\tag{3.9}$$

The experimental Reynolds numbers based on the chord length for the test cases examined are in the range $Re_c \approx 3.0 \times 10^6 - 5.0 \times 10^6$, and it is expected that the flow is mostly turbulent. Transitional flow is expected to have a small effect at regions very close to the leading edge. Present knowledge about boundary layer transition does not enable computation and modeling of the transition regime. Therefore, only fully turbulent solutions were computed. In the present work, the widely used two-layer Baldwin–Lomax turbulence model was used. The effectiveness of other turbulence models, such as the Johnson–King model [Ref. 32] and the RNG based algebraic model [Ref. 33] for steady and unsteady flows, was investigated in references [34] and [35].

C. BOUNDARY CONDITIONS

The solutions on the two grids are computed separately, with the inner and outer solutions communicating through the zonal interface boundary. The inner grid

surrounds the airfoil and includes the boundary layer region and the wake for viscous solutions. Inviscid solutions are obtained by applying the flow tangency slip condition where the normal contravariant velocity component, W , is set equal to zero on the surface. For viscous solutions, the nonslip condition is applied for the velocities on the airfoil surface. In both cases the density and pressure are obtained from the interior grid points by simple extrapolation. For unsteady solutions, the surface velocity is set equal to the airfoil speed obtained by the prescribed airfoil motion as follows

$$u = \frac{1}{J}(\zeta_t \xi_z - \xi_t \zeta_z), \quad w = \frac{1}{J}(\xi_t \zeta_x - \zeta_t \xi_x)$$

Unsteady solutions for pitching and oscillating airfoils are obtained by rotating the inner grid only. Therefore, only the metrics of the inner grid must be reevaluated for each time step.

At the inner zonal interface, the flow variables are obtained from the interior of the outer grid solution. Similarly, the inner zonal boundary of the outer grid obtains boundary information from the interior of the inner grid. The inner and outer grid radial lines are not aligned, in general. The relative location of the two grids with respect to the inertial reference frame as the inner grid rotates is computed. These distances between neighboring points at the zonal interface are used for a weighted averaging of the conservative variables.

All flows were computed for subsonic free-stream speeds. At the subsonic inflow and outflow boundaries of the outer grid, the flow variables were reevaluated using zero-order Riemann invariant extrapolation. At the inflow boundary, there are three incoming and one outgoing characteristics. Therefore, three variables, the density ρ , the normal velocity w , and the pressure p , are specified and the fourth variable, the axial velocity u is extrapolated from the interior. The inflow boundary conditions are given by

$$\begin{aligned}
\rho_1 &= \left(\frac{a_1^2}{\gamma s_1} \right)^{(1/\gamma-1)} \\
s_1 &= \left(\frac{\rho_\infty}{\rho_1} \right) \\
a_1 &= \frac{(\gamma-1)}{4} (R_1^+ - R_2^-) \\
u_1 &= (R_1^+ + R_2^-)/2 \\
w_1 &= w_\infty \\
p_1 &= \left(\frac{\rho_1 a_1^2}{\gamma} \right)
\end{aligned} \tag{3.10}$$

where R_1^+, R_2^- are the incoming and outgoing Riemann invariants given by

$$R_1^+ = u_\infty + 2a_\infty/(\gamma - 1), \quad R_2^- = u_2 - 2a_2/(\gamma - 1)$$

At the outflow boundary there are one incoming and three outgoing characteristics. Therefore only one quantity, the pressure, is specified, while the others are extrapolated from the interior. For the density and normal velocity, simple first-order extrapolation is used, and the axial outflow velocity is obtained from the zero-order outgoing Riemann invariant. The outflow boundary conditions are given by

$$\begin{aligned}
\rho_1 &= \rho_2 \\
u_1 &= R_1^+ - 2a_1/(\gamma - 1) \\
a_1 &= \sqrt{\gamma p_1 / \rho_1} \\
w_1 &= w_2 \\
p_1 &= p_\infty
\end{aligned} \tag{3.11}$$

were solved. For the unsteady flow solutions, the outer grid remained stationary and the metrics were not reevaluated at each time step.

IV. RESULTS AND DISCUSSION

The validity of the zonal grid approach was first investigated for inviscid solutions. An advantage of the present approach is that different grid densities may be used for the inner and outer grids. However, the accuracy and the conservative character of the solution for different locations of the zonal interface and grid densities must be assessed.

First, the accuracy of the computed results for different inner and outer grid densities was evaluated. The effect of the location of the zonal interface relative to the airfoil on the accuracy of the solution was also investigated. Then viscous solutions at fixed angles of incidence, up to approximately the static stall angle, were computed. Finally, unsteady flow responses to a ramp motion at subsonic free-stream speed of $M_\infty = 0.3$ and for an oscillation at a free-stream speed of $M_\infty = 0.6$ were computed.

A. STEADY STATE SOLUTIONS

1. Inviscid Test Cases

Preliminary test cases were computed using coarse meshes with an inviscid solution. A two-block grid consisting of an 81×40 point O-type inner grid and an 81×22 point O-type outer grid was used as a baseline grid for the inviscid solutions. Table 4.1 gives the inviscid grids that were tested.

a. Case 1. Baseline Grid: 81x40 Inner and 81x22 Outer

An inviscid solution using the baseline grid for subsonic flow over a NACA-0012 airfoil at $M_\infty = 0.8$, $\alpha = -1^\circ$ was obtained. The baseline grid is given in figure 4.2. The distribution of the computed surface pressure coefficient is compared with the measurements of [Ref. 4] in Fig. 4.1. Agreement with the experimental data

TABLE 4.1: GRID DENSITIES OF THE INVISCID SOLUTIONS COMPUTED FOR A NACA-0012 AIRFOIL AT $M_\infty = .8$ AND $\alpha = -0.1$.

Case	Inner Grid	Outer Grid	Inner Grid Radius
1	81×40	81×22	$1.5 \times \text{chord}$
2	81×40	41×22	$1.5 \times \text{chord}$
3	81×40	81×22	$1.0 \times \text{chord}$
4	81×40	81×22	$.75 \times \text{chord}$
5	81×18	81×19	<i>OvalGrid</i>
6	81×20	41×12	$1.5 \times \text{chord}$

is satisfactory for an Euler solution. It can be seen that with this mesh the strength of the shock is captured, but the location is lagged by 5 percent of the chord. The baseline solution is converged at 2000 iterations.

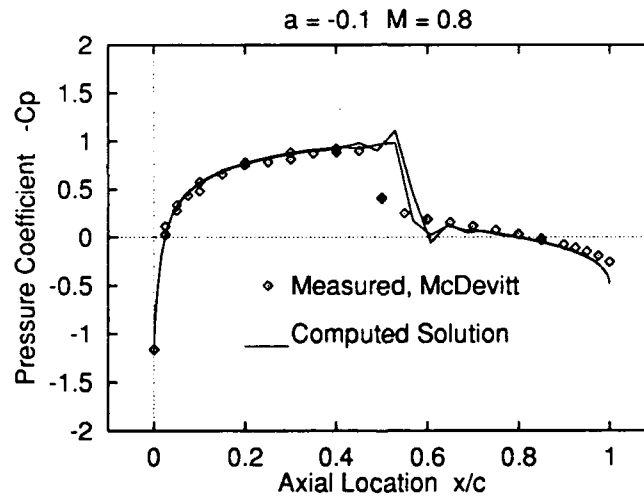


Figure 4.1: $M_\infty = 0.8$ Computed Solution With Baseline Grid Compared to Experiment.

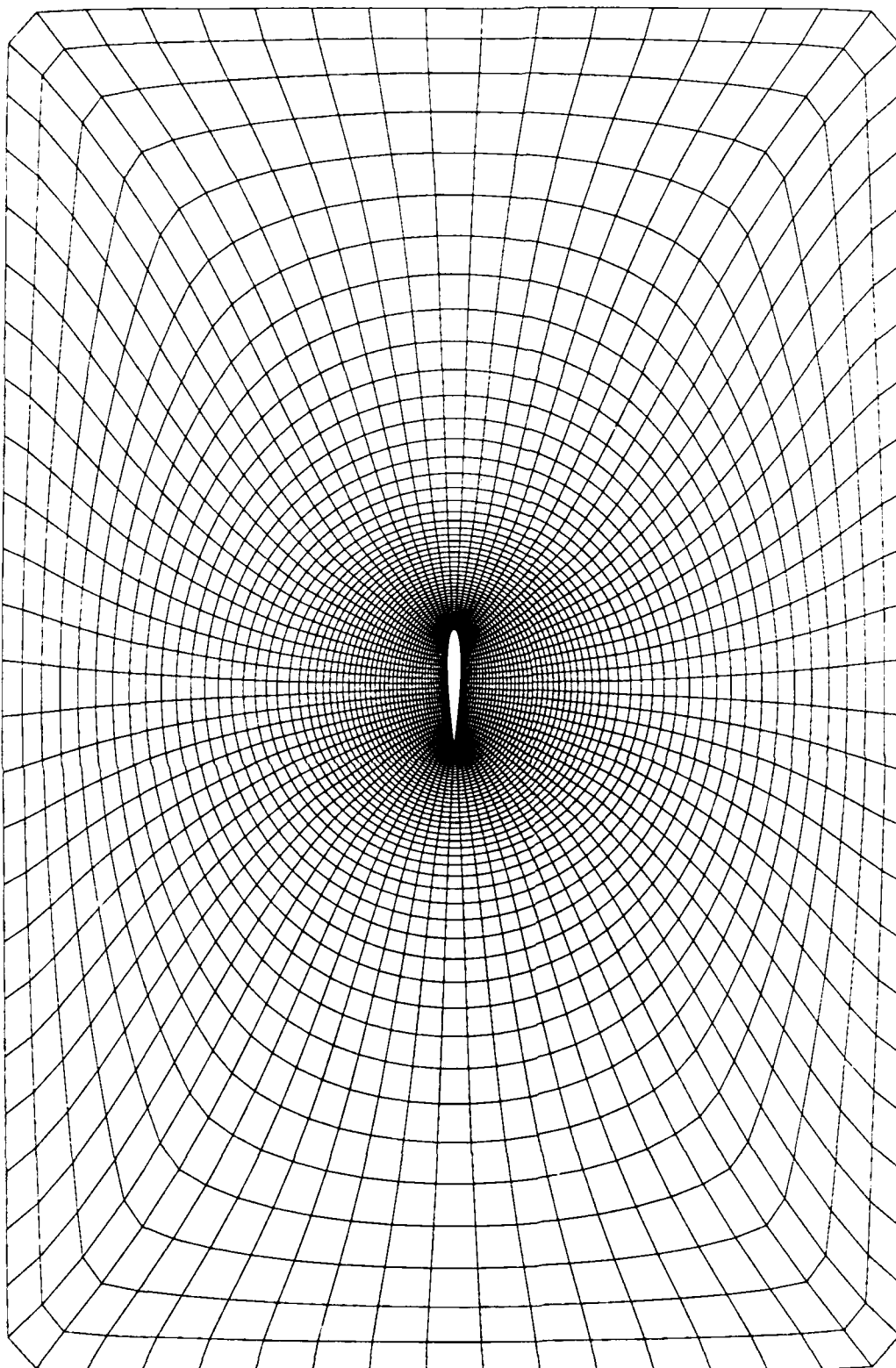


Figure 4.2: Inner Grid 81×40 Outer Grid is 81×22

b. Case 2. Baseline Inner Grid With a 41x22 Outer Grid

Next the effect of the outer grid density is investigated. The grid for Case 2 was generated by starting with the baseline grid and removing every other grid point from the outer grid. The resulting grid is given in Fig. 4.4. The Euler solution is compared to experiment in Fig. 4.3. Overall the converged solution for this case agrees with the baseline solution except it is noticed that the shock location for the upper and lower surface are slightly farther apart than the baseline grid solution.

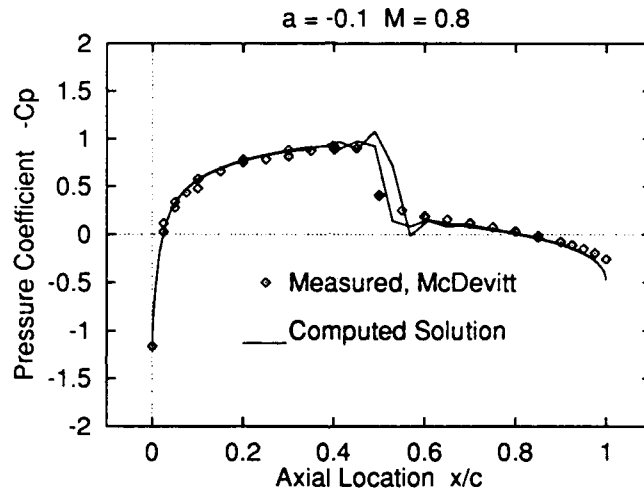


Figure 4.3: $M_\infty = 0.8$ Computed pressure coefficient solution compared to experimental data.

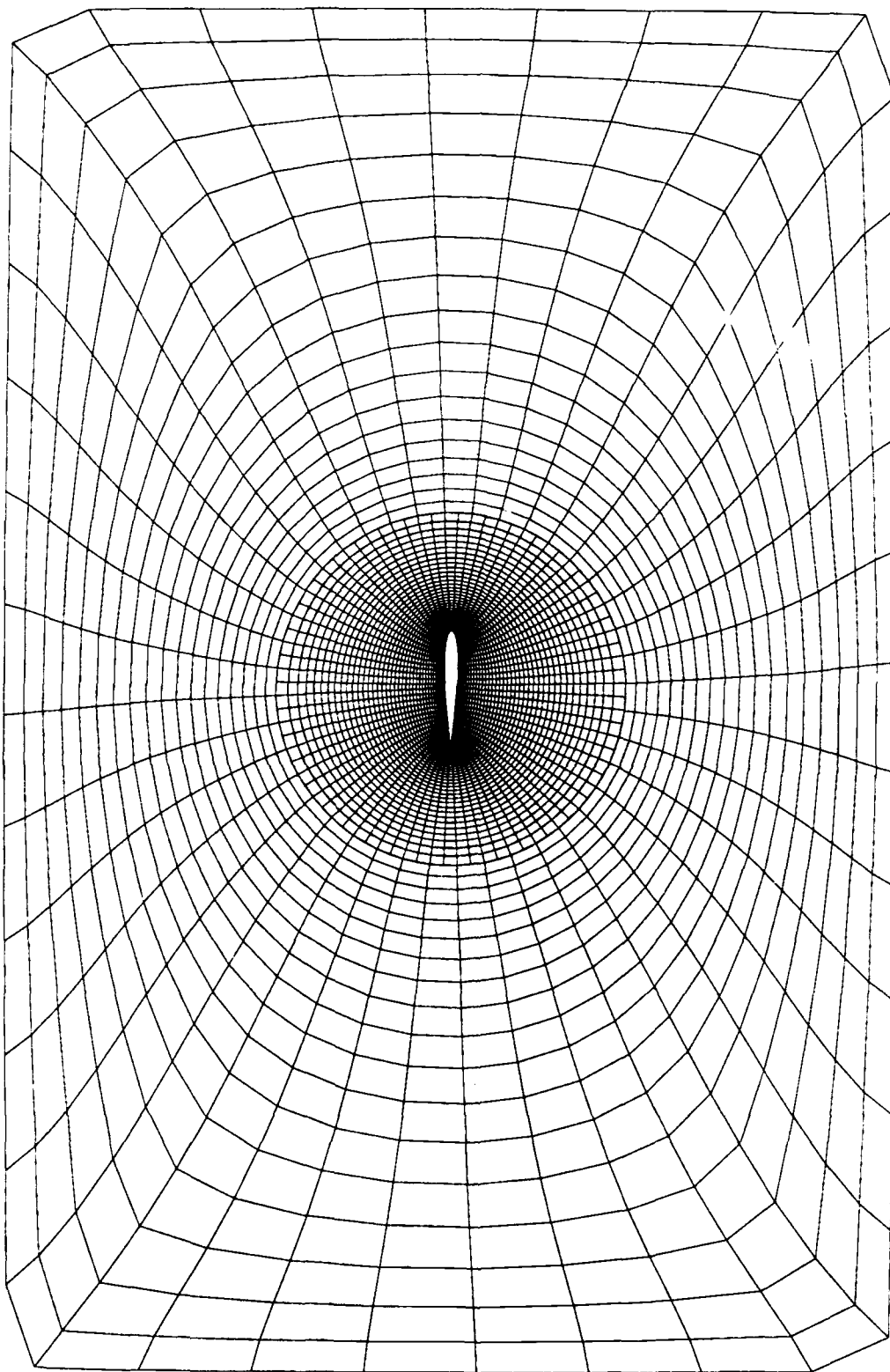


Figure 4.4: Inner Grid 81×40 Outer Grid is 41×22

c. **Case 3. Overlap Boundary Set to 1 Chord Length Away From Body**

In this case the effect of the overlap boundary location is studied. The grid generated is given in Fig. 4.6. It is seen that the transition from the inner to the outer grid is not as smooth as for the cases where the boundary was located 50 percent farther from the airfoil. At the leading and trailing edges, the overlapped boundary is only a half chord length away. In figure 4.5 the converged solution is given. With this grid very little effect on the shock strength and location is seen. The pressure coefficient before the shock is slightly underpredicted and after the shock is slightly overpredicted.

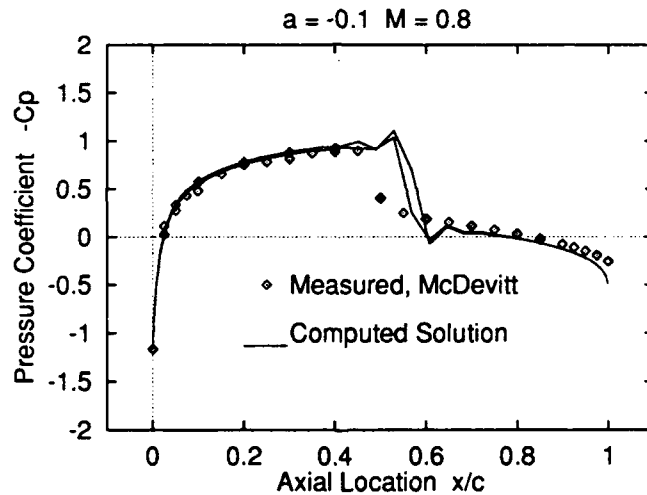


Figure 4.5: $M_\infty = 0.8$ Computed Solution Compared to Experiment.

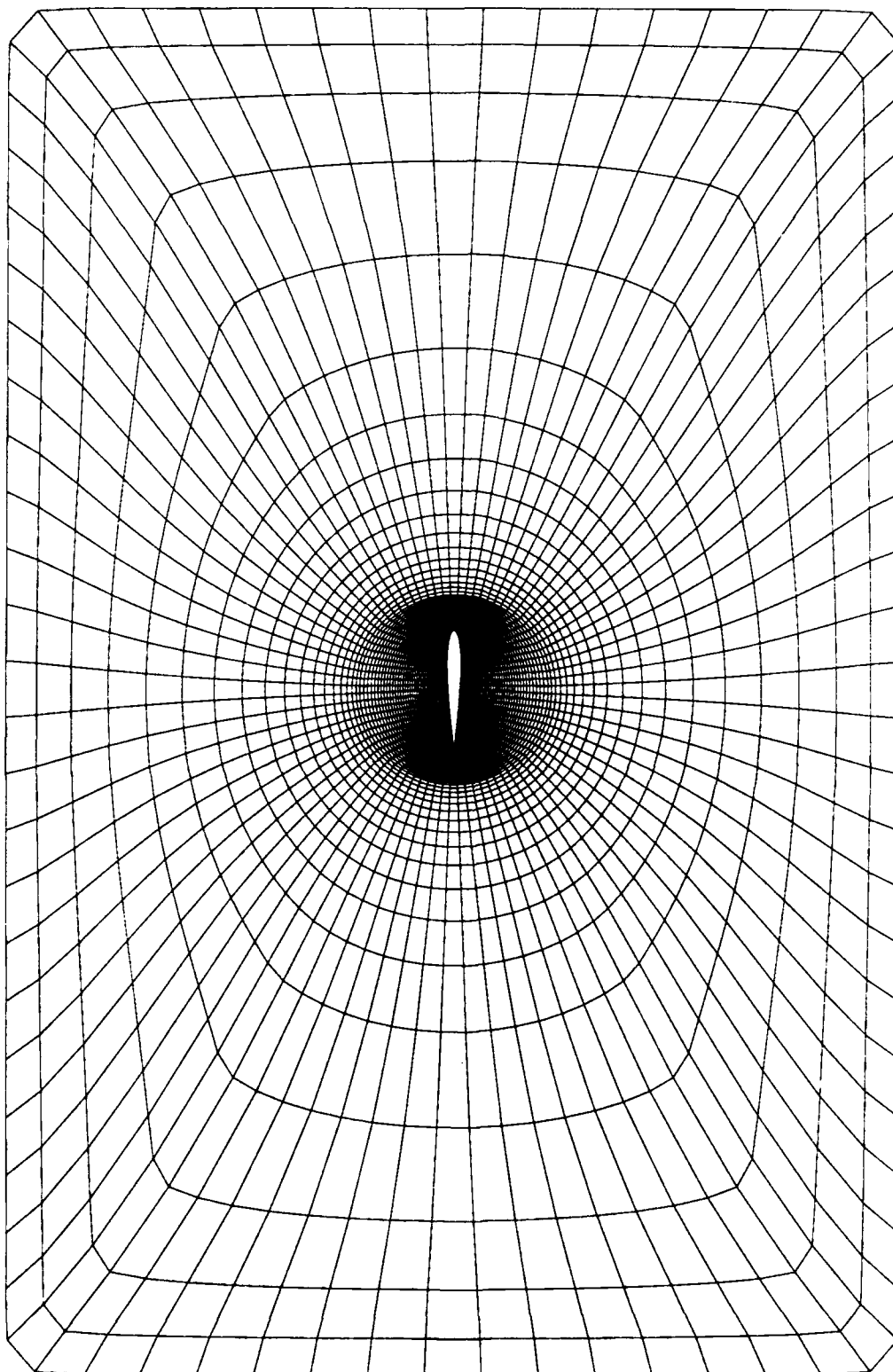


Figure 4.6: Inner Grid 81×40 Outer Grid is 81×22

d. Case 4. Overlap Boundary Set to .75 Chord Length Away From Airfoil

In order to further investigate the tendencies observed in Case 3, another grid is developed with the zonal interface closer to the airfoil. The overlapped region is only a quarter chord away from the leading and trailing edges of the airfoil as seen in Fig. 4.8. The solution obtained is compared to experiment in Fig. 4.7. The pressure coefficient is again slightly underpredicted before the shock and slightly overpredicted after the shock. It is also observed that the zonal interface location relative to the airfoil has little effect on the solution.

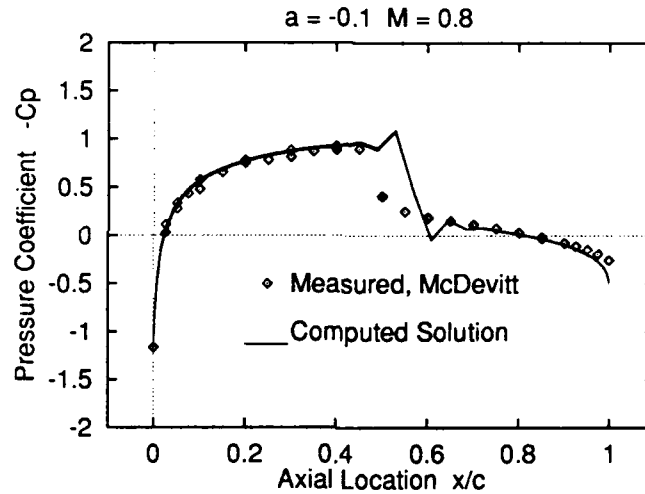


Figure 4.7: $M_\infty = 0.8$ Computed Solution Compared to Experiment.

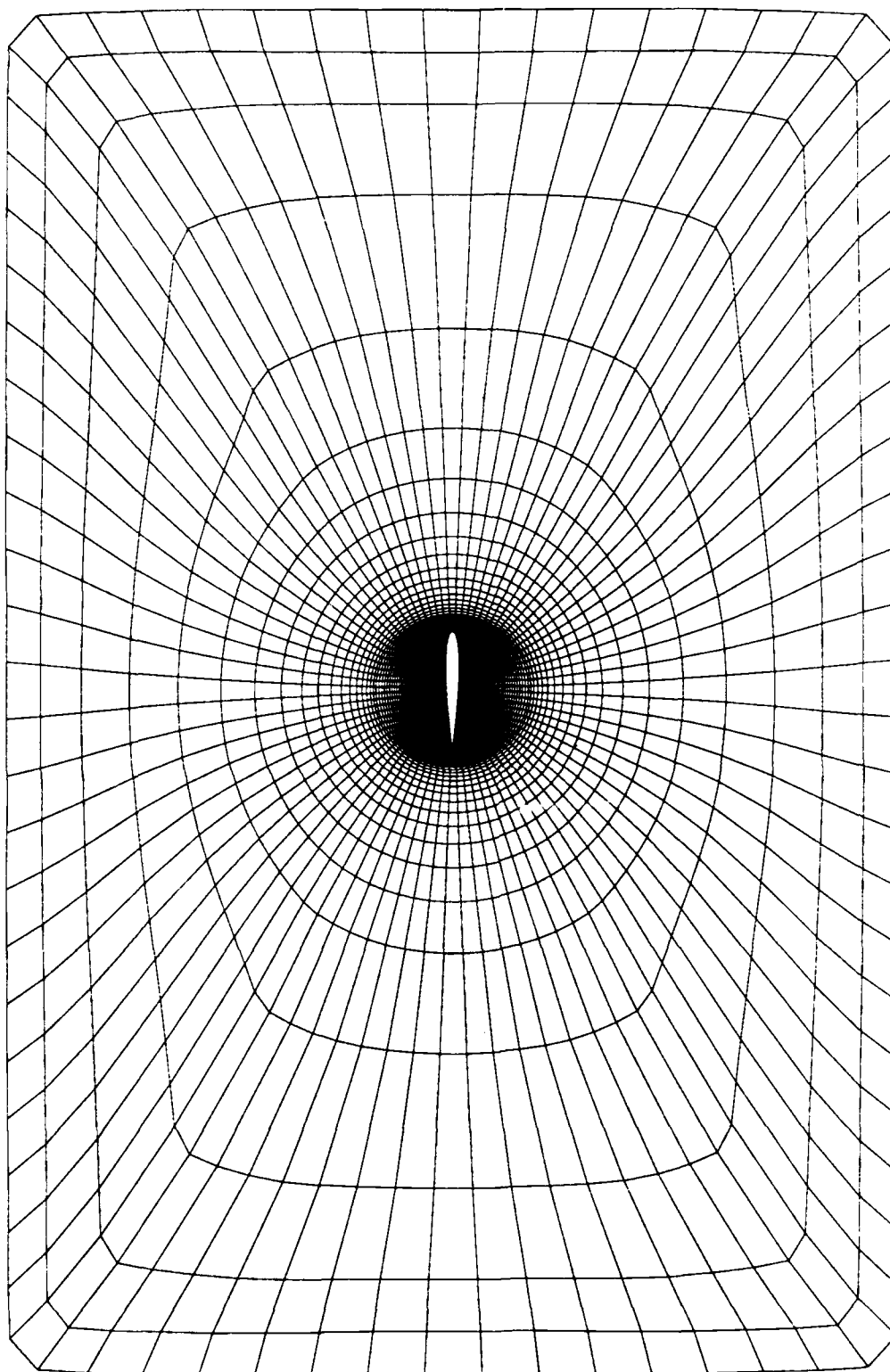


Figure 4.8: Inner Grid 81×40 Outer Grid is 81×22

e. Case 5. Grid With Oval Interface

The solution obtained for cases 3 and 4 showed that the location of the zonal interface had very little effect on the computed solutions. The ability of the zonal interface to pass flow discontinuities was also studied. It was known from the previous cases that the shock location was near the the mid chord point. The inner grid for this test case had to be generated so that the overlapped region was very close to the upper and lower surface of the airfoil. This was accomplished by generating an oval inner grid and an oval zonal interface. This grid is shown in figure 4.10. The computed surface pressure coefficient distribution is shown in figure 4.9. It is in agreement with the experimental data and with the previous computed solutions. The computed flow quantities, such as density and pressure, showed that the zonal approach used can pass shocks through the zonal interface. Figure 4.11 shows Mach contours which smoothly pass through the overlapped boundary.

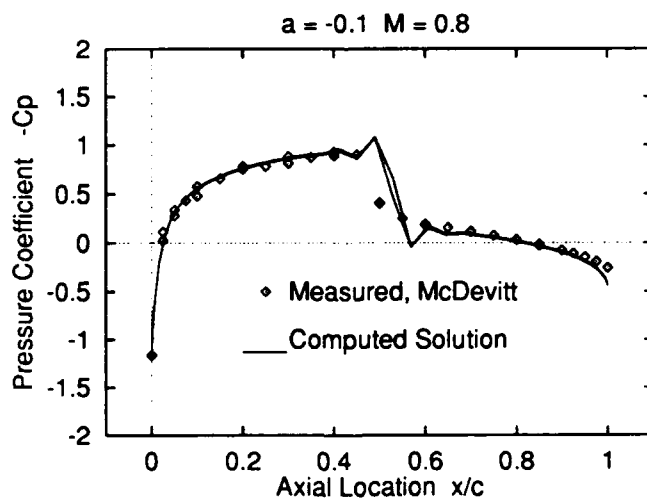


Figure 4.9: $M_\infty = 0.8$ Computed Solution Compared to Experiment.

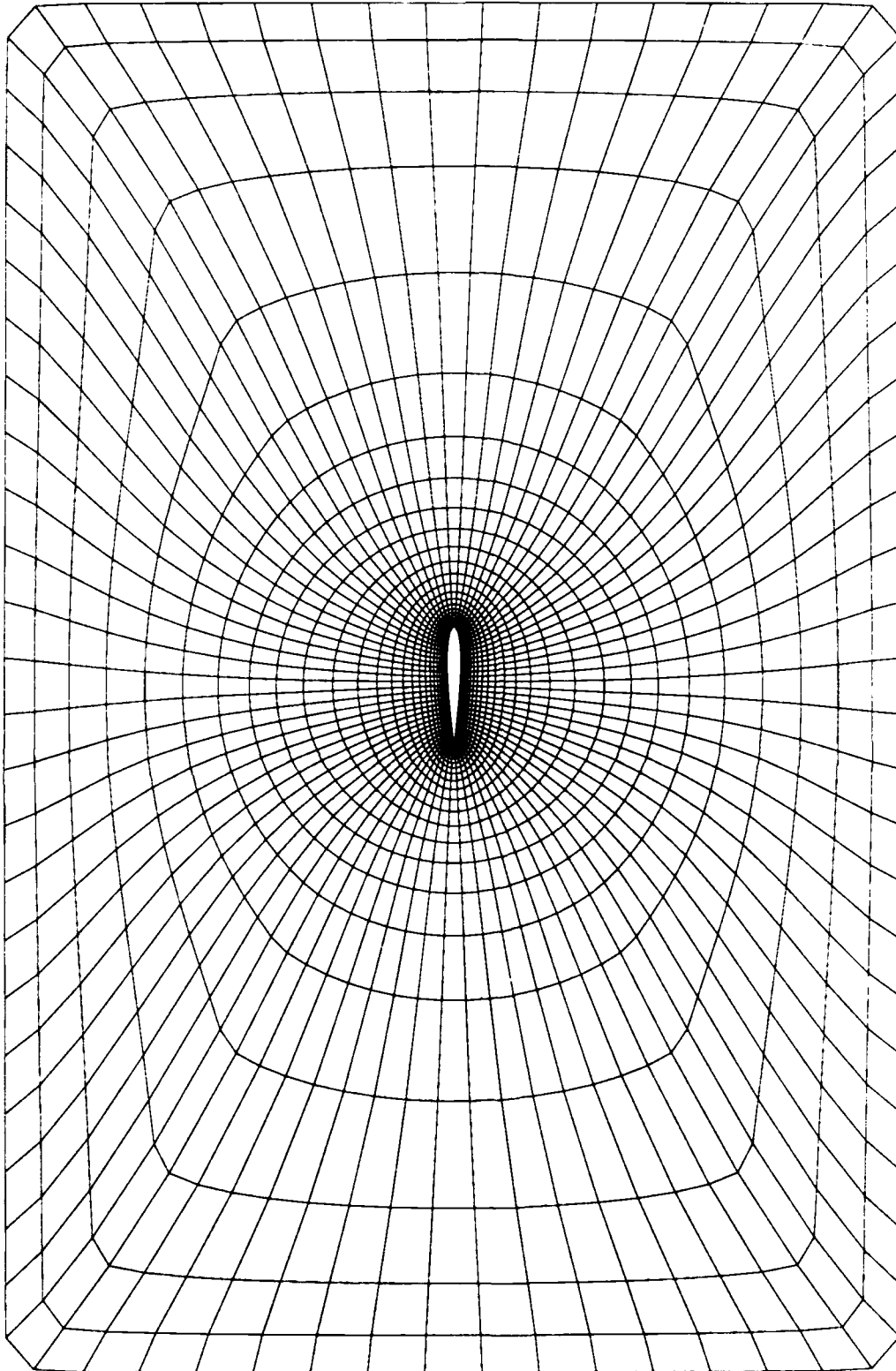


Figure 4.10: Inner Grid 81×18 Outer Grid is 81×19

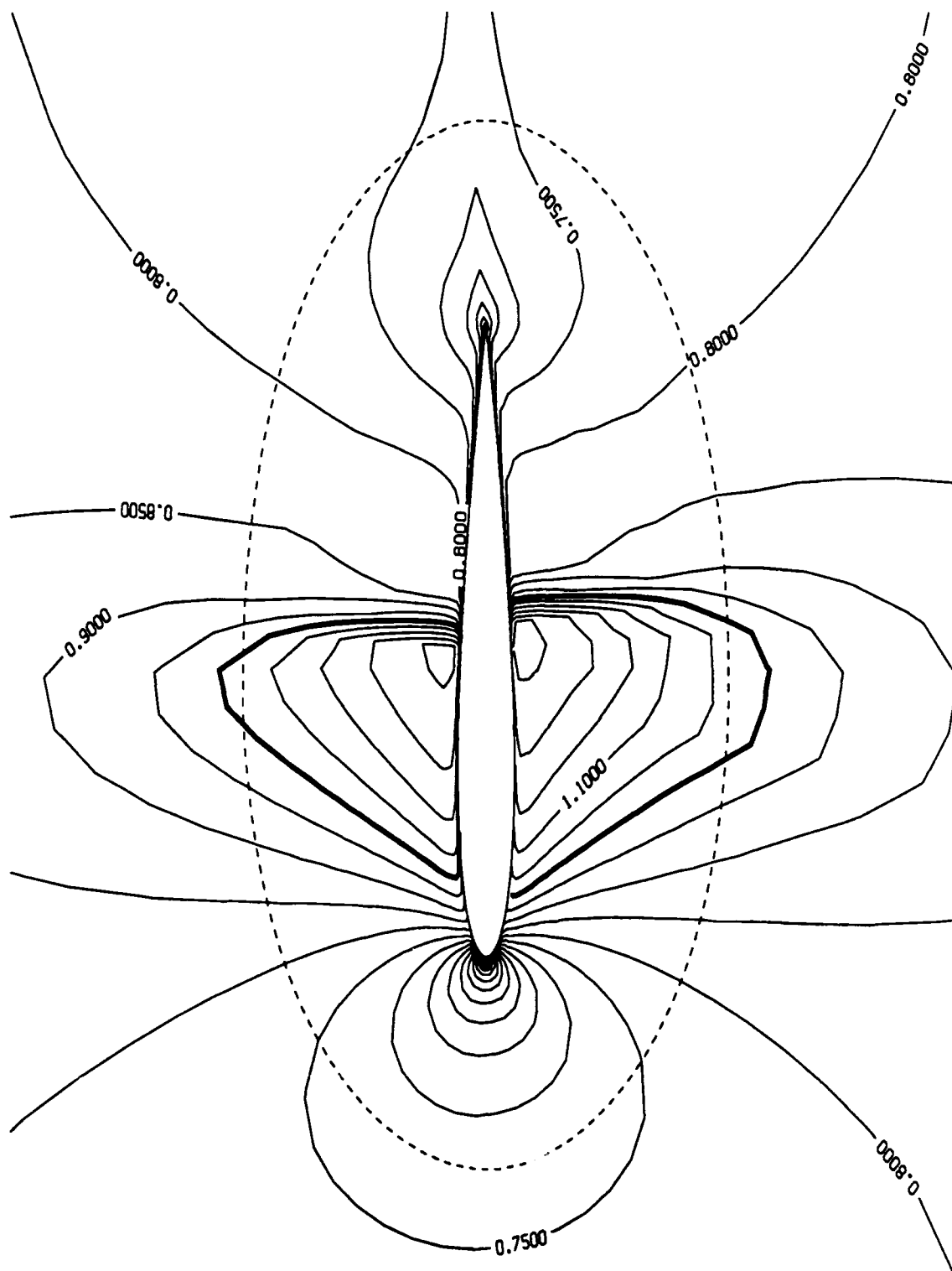


Figure 4.11: Mach Contours: Overlapped Region's Ability to Pass Flow Discontinuities.

f. Case 6. Baseline Grid With Half the Radial Grid Points On Outer Grid

In the previous cases, the effect of circumferential resolution was studied. Next, the effect of the radial resolution on the computed solutions is investigated. Figure 4.13 shows the grid generated to test these effects. The computed surface pressure coefficient distribution (in figure 4.12) was comparable with the solutions obtained with denser outer grids. Computations with an even coarser grid, e.g., a 41×11 point grid, predicted the shock location even further downstream due to lack of streamwise resolution.

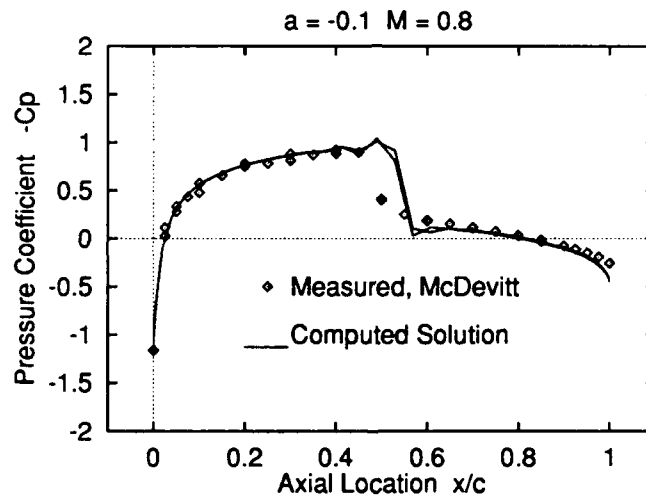


Figure 4.12: $M_\infty = 0.8$ Computed Solution Compared to Experiment.

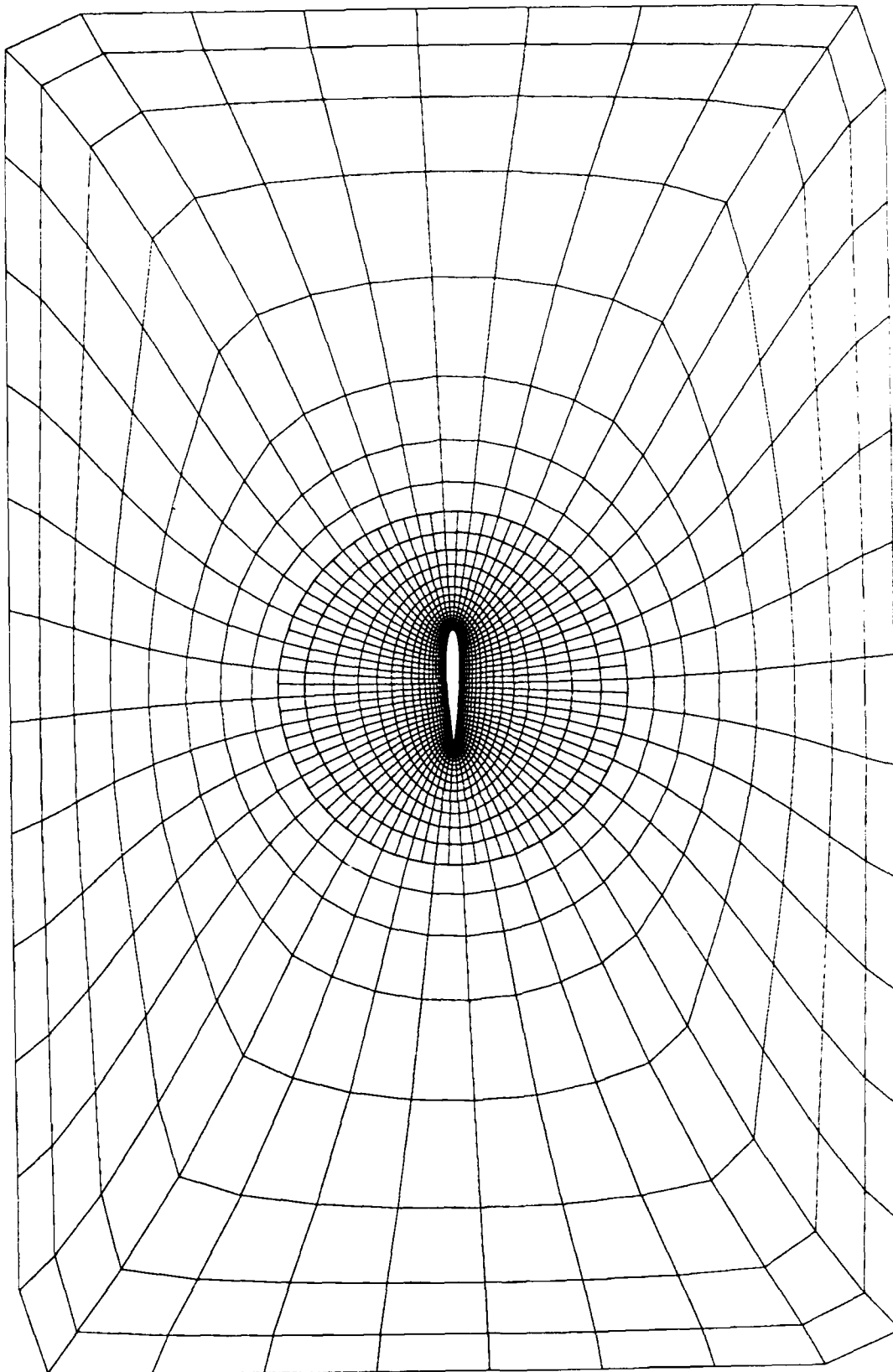


Figure 4.13: Inner Grid 81×40 Outer Grid is 41×12

2. Viscous Test Case

The Euler solutions presented in the previous section were used to study the effects of different grid densities on the computed solutions. Having confidence in the predictions of the code, the next step was to generate a viscous grid with the airfoil's quarter chord point at the center of the inner grid.

Viscous, subsonic flow solutions were obtained at the following fixed angles of attack: 3.27° , 4.97° , 6.69° , 8.38° , 9.27° , 10.12° , 10.99° and 11.90° . The flow conditions of the measurements reported in [Ref. 21] were used, e.g., $M_\infty = 0.3$, $Re = 4.0 \times 10^6$. The spacing of the grid was set to 0.0005 for the first grid point above the surface. The quarter chord point of the airfoil was set at the center of rotation so the airfoil could be ramped about the quarter chord point. These solutions were obtained on a 181×56 point viscous inner grid and a 181×26 point inviscid outer grid shown in figure 4.14.

Solutions were also computed on a grid with half the streamwise resolution, e.g., a 91×56 point grid. The computed surface pressure coefficient distributions using the 181×56 inner grid and 181×26 outer grid, are compared to experimental results in figures 4.15 through 4.23.

Solutions for fixed angles of incidence were obtained by two methods. First by rotating the inner grid to the specified angle of incidence and setting the oncoming flow to zero degrees. Second by rotating the flow to the angle of incidence and leaving the inner grid at zero angle relative to the outer grid. The computed pressure coefficients and boundary layers were the same for both cases.

For the low Mach number viscous solutions, no flux limiting was applied. It is seen that the computed results closely agree with the experimental data. At the higher angles of incidence the suction peak is not exactly captured. This is probably due to lack of grid resolution at the leading edge of the airfoil.

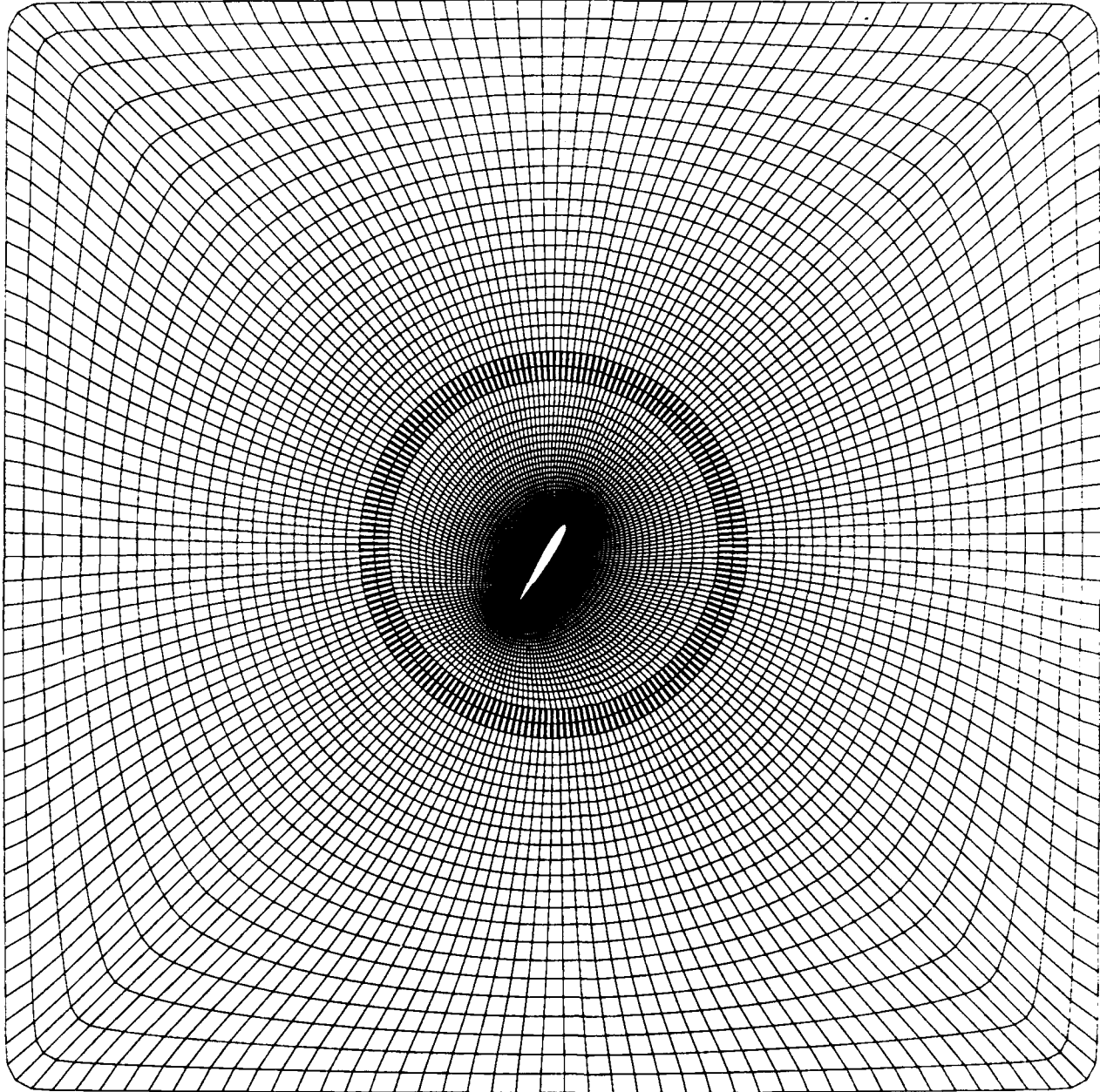


Figure 4.14: A NACA-0012 Airfoil Grid Centered at the Quarter Chord Point, 181x58 Inner Grid and 181x26 Outer.

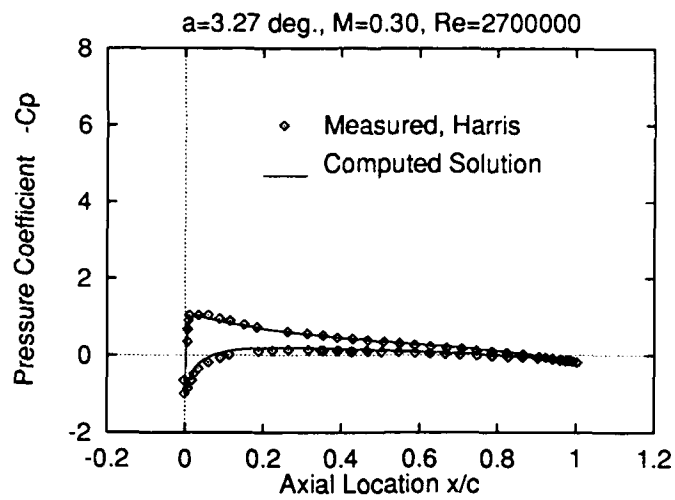


Figure 4.15: Viscous Computed Solution Compared to Experiment for $\alpha = 3.27^\circ$.

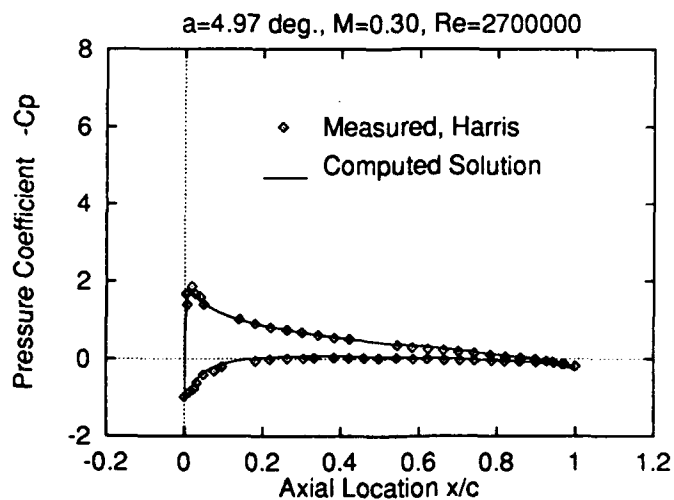


Figure 4.16: Viscous Computed Solution Compared to Experiment for $\alpha = 4.97^\circ$.

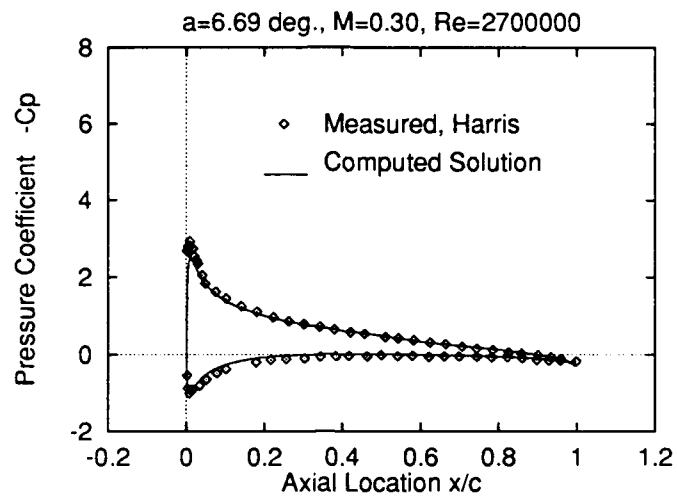


Figure 4.17: Viscous Computed Solution Compared to Experiment for $\alpha = 6.69^\circ$.

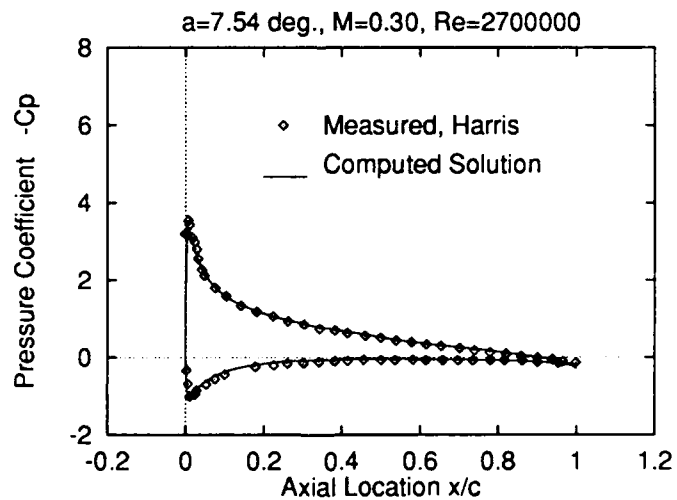


Figure 4.18: Viscous Computed Solution Compared to Experiment for $\alpha = 7.54^\circ$.

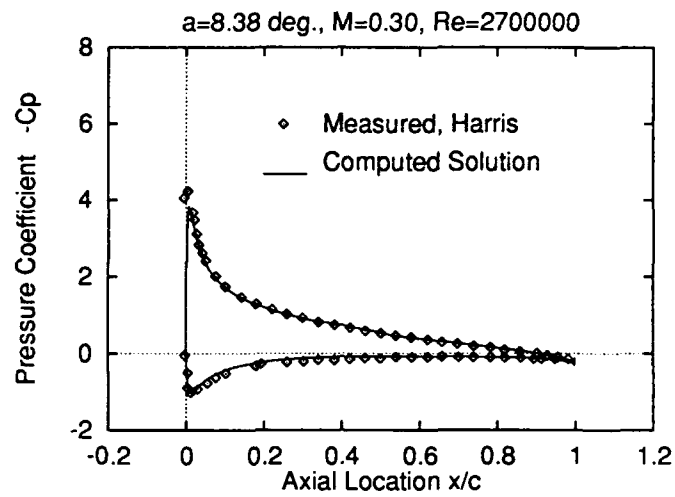


Figure 4.19: Viscous Computed Solution Compared to Experiment for $\alpha = 8.38^\circ$.

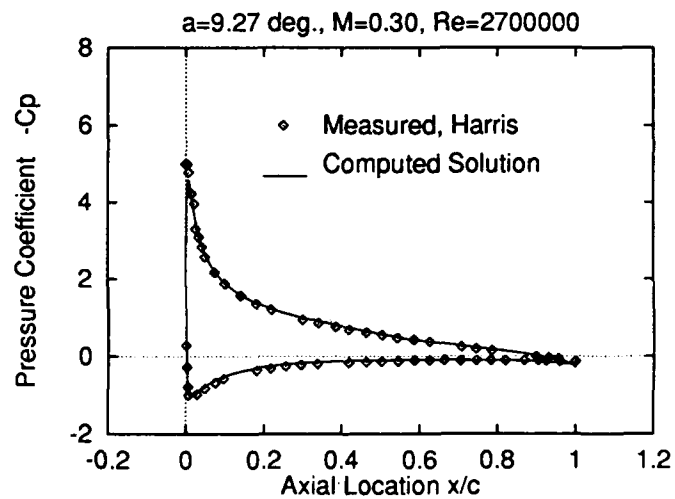


Figure 4.20: Viscous Computed Solution Compared to Experiment for $\alpha = 9.27^\circ$.

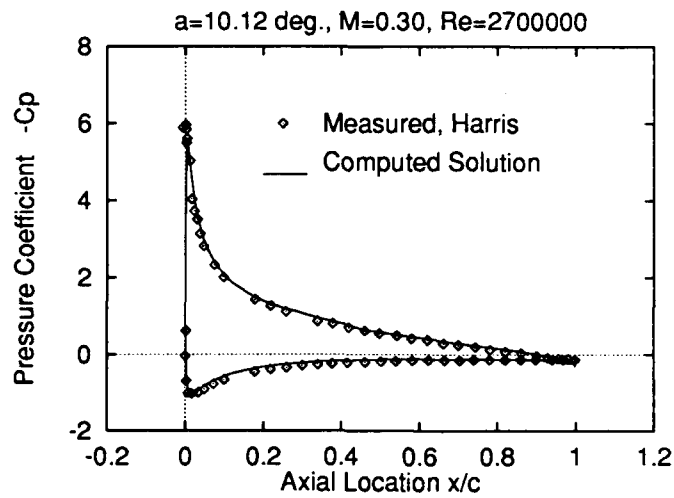


Figure 4.21: Viscous Computed Solution Compared to Experiment for $\alpha = 10.12^\circ$.

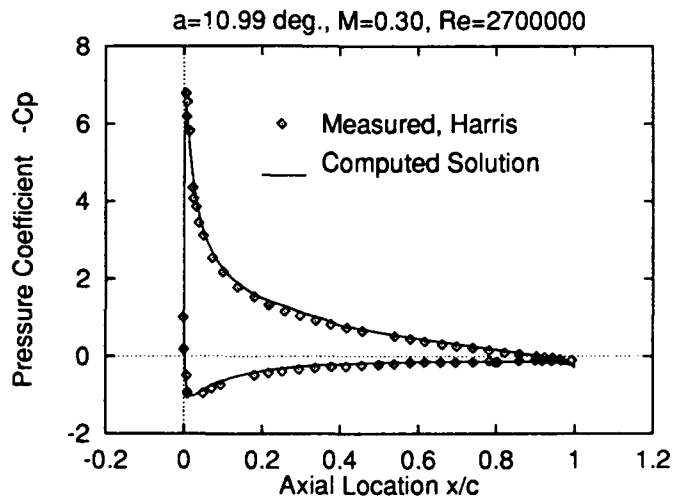


Figure 4.22: Viscous Computed Solution Compared to Experiment for $\alpha = 10.99^\circ$.

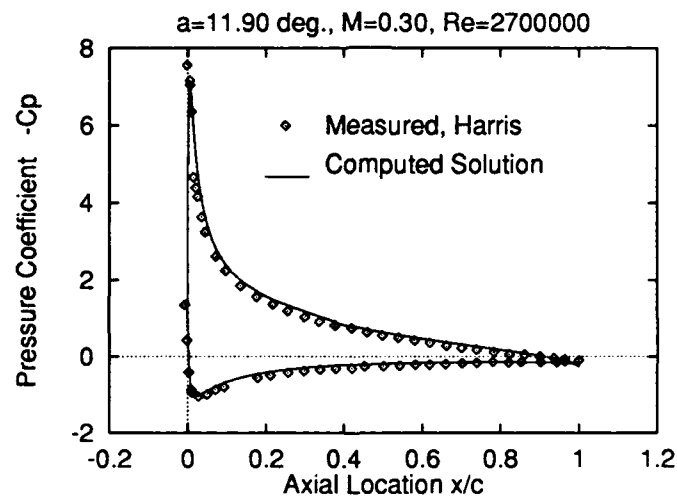


Figure 4.23: Viscous Computed Solution Compared to Experiment for $\alpha = 11.99^\circ$.

B. RAMP MOTION SOLUTION

The unsteady solution for a ramp motion from $\alpha = 0^\circ$ to $\alpha = 30^\circ$ at $M_\infty = 0.3$, $Re = 2.7 \times 10^6$ and reduced frequency, $k = 0.0127$ was obtained on both a 91×56 point inner grid and a 181×56 point inner grid. The pitch rate for the ramp motion k is defined as $k = \dot{\alpha}c/2U_\infty$. The computed lift response is compared with the experimental measurements of [Ref. 6] in Figure 4.24.

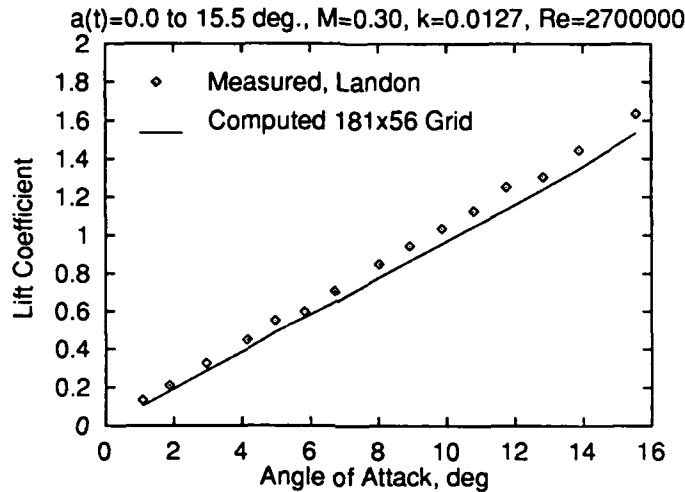


Figure 4.24: Comparison of the Measured and Computed Lift for the Ramp Motion

Both the coarse and fine grid solutions closely predict the measured lift. However, at the higher angles of attack, the finer grid gives higher lift. The computed surface pressure coefficient distributions at several angles of incidence are compared in Figures 4.25 - 4.38. Experimental surface pressure coefficients were available for the following angles of incidence: 2.94° , 5.84° , 8.91° , 11.76° , 15.5° , and they are displayed as diamonds in the figures. The computed surface pressure coefficient distribution is in good agreement with the measured data over the entire incidence range. The computed flowfield at the maximum angle of incidence, $\alpha = 15.5^\circ$, is mostly attached. A small separated flow region exists at the trailing edge region only. At a higher angle

of attack, $\alpha \approx 17.0^\circ$, the computed solution shows the development of the dynamic stall vortex in the leading edge region.

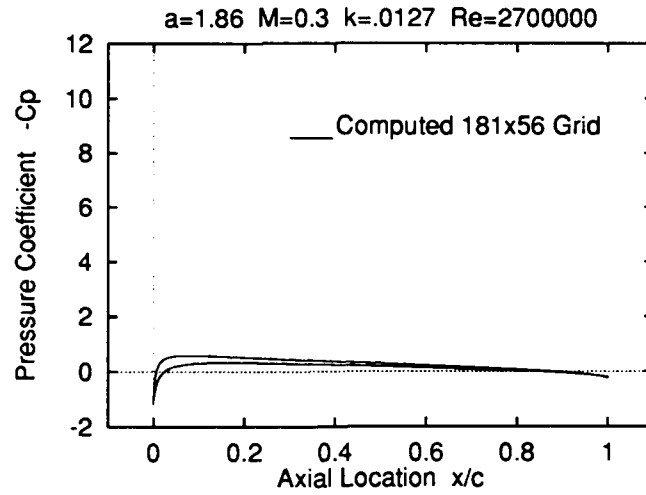


Figure 4.25: Computed ramp solution at $\alpha = 1.86^\circ$.

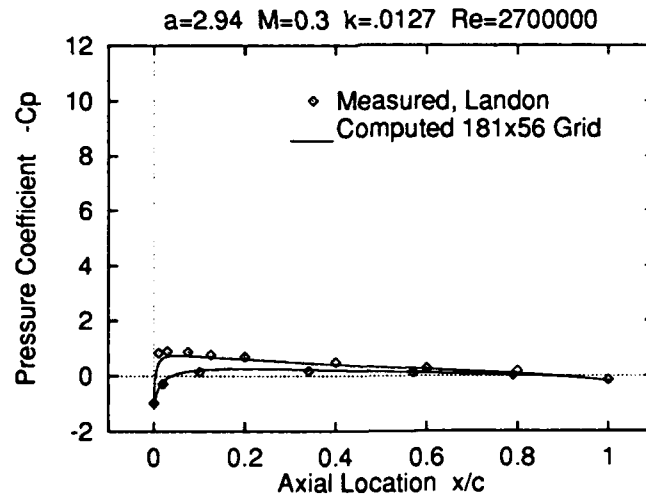


Figure 4.26: Computed ramp solution compared to experimental data at $\alpha = 2.94^\circ$.

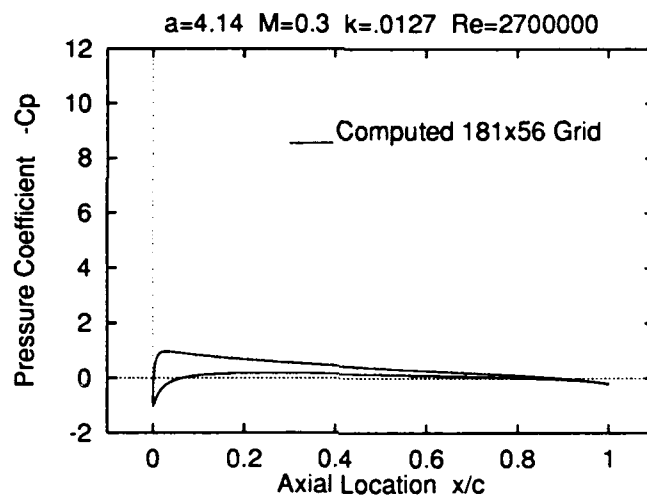


Figure 4.27: Computed ramp solution at $\alpha = 4.14^\circ$.

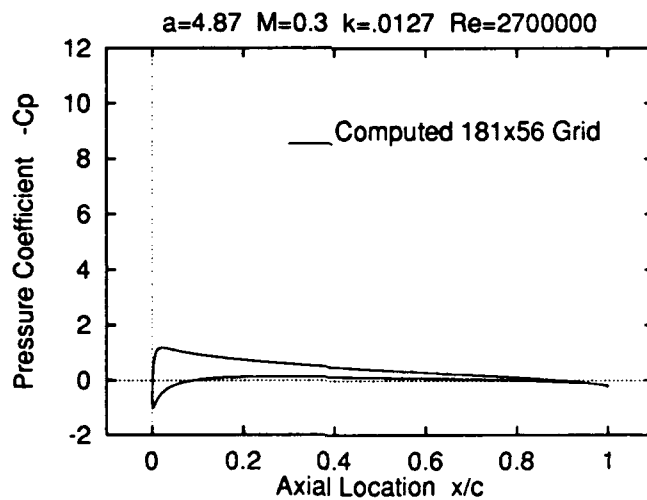


Figure 4.28: Computed ramp solution at $\alpha = 4.87^\circ$.

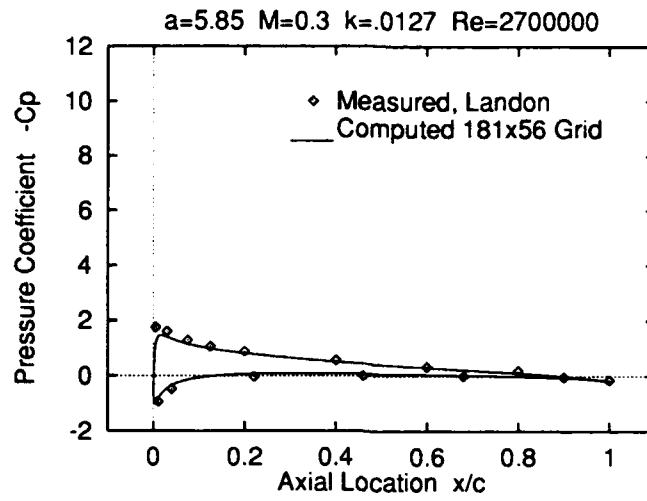


Figure 4.29: Computed ramp solution compared to experimental data at $\alpha = 5.85^\circ$.

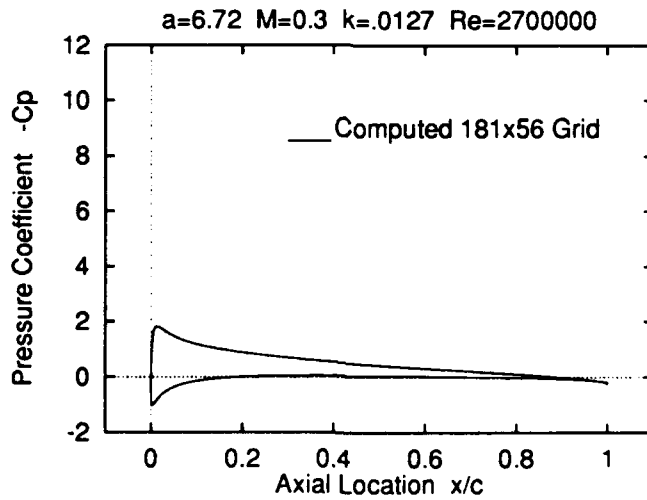


Figure 4.30: Computed ramp solution at $\alpha = 6.72^\circ$.

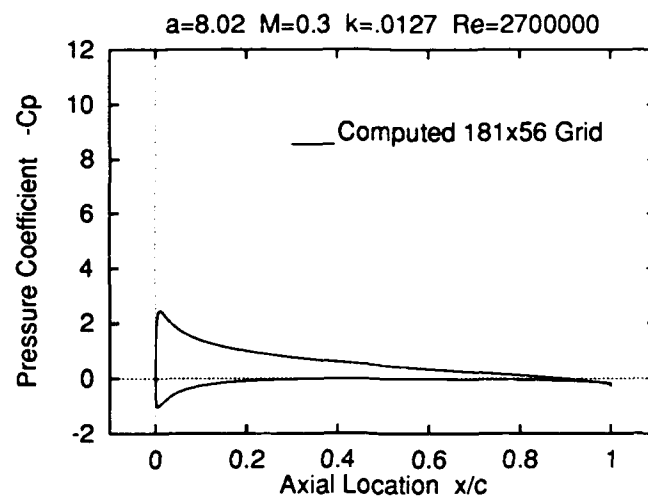


Figure 4.31: Computed ramp solution at $\alpha = 8.02^\circ$.

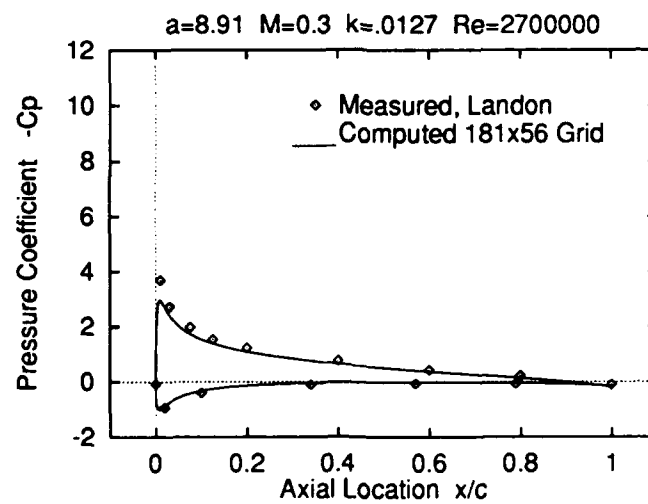


Figure 4.32: Computed ramp solution compared to experimental data at $\alpha = 8.91^\circ$.

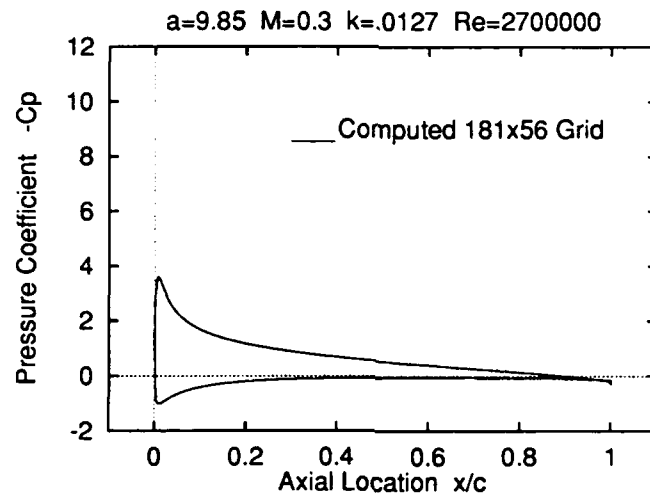


Figure 4.33: Computed ramp solution at $\alpha = 9.85^\circ$.

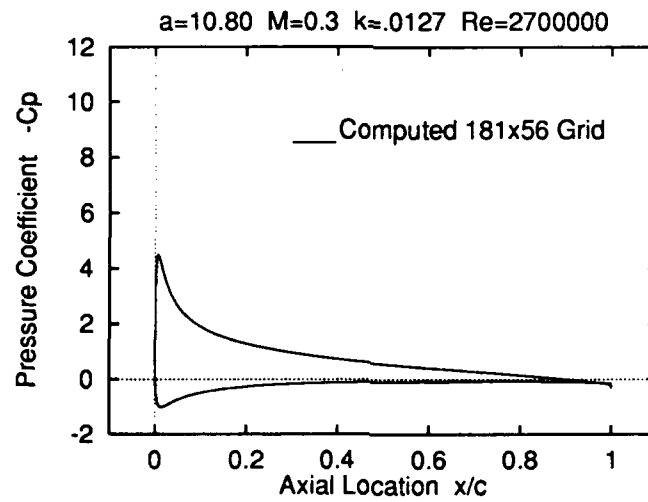


Figure 4.34: Computed ramp solution at $\alpha = 10.80^\circ$.

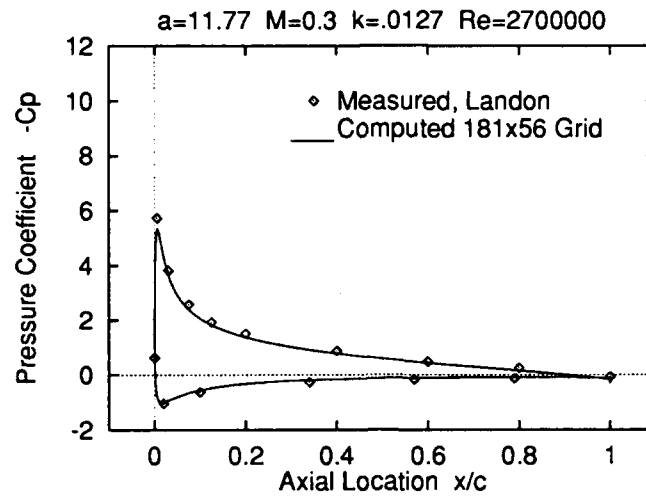


Figure 4.35: Computed ramp solution compared to experimental data at $\alpha = 11.77^\circ$.

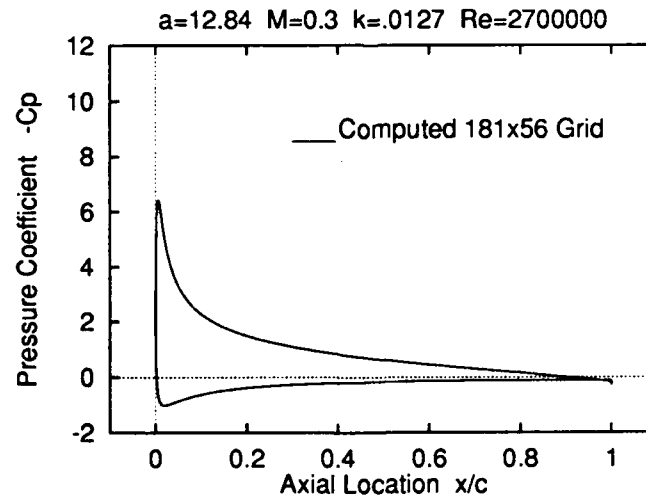


Figure 4.36: Computed ramp solution at $\alpha = 12.84^\circ$.

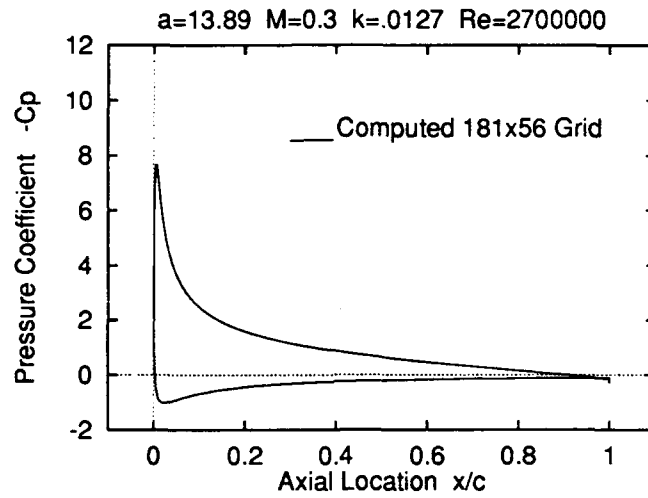


Figure 4.37: Computed ramp solution at $\alpha = 13.89^\circ$.

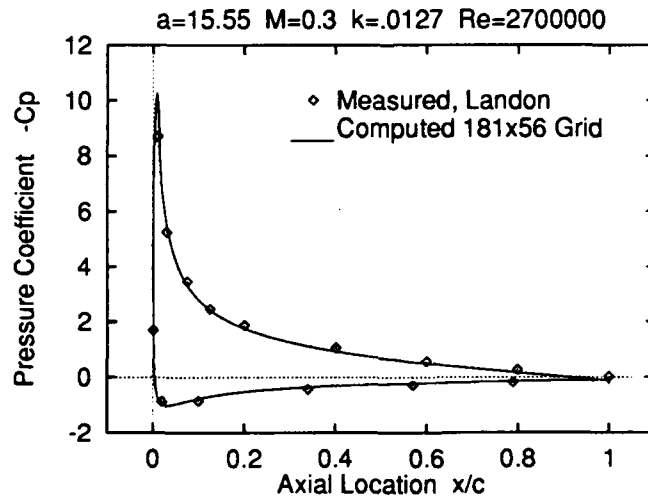


Figure 4.38: Computed ramp solution compared to experimental data at $\alpha = 15.55^\circ$.

1. Boundary Layer Comparisons For Ramp Motion

Early on in the development of the software, the computed pressure coefficients agreed quite well with the experimental data. As test cases at higher angles-of-attack were tested, it was discovered that the flow was not separating from the trailing edge of the airfoil. The problem was discovered by investigating the boundary layer profiles. A problem in the turbulence model was discovered and easily fixed. The lesson here is that although the computed and experimental pressure coefficients agree quite well it is important to check that the boundary layer profiles are reasonable. In figures 4.39 through 4.48 the computed boundary layers are compared to boundary layers computed by the interactive viscous inviscid boundary layer method of reference [22].

The comparisons are made at $x/c = .5$ and at $x/c = .9$ for angles-of-attack ranging from 2.94° to 15.5° . The computed boundary layer profiles compare quite well up to 15.5° . At $x/c = .9$ for the angle-of-attack of 15.5° , the comparisons diverge. This happens because of the different turbulence models used. At this angle-of attack, the flow is separating at the trailing edge so the turbulence models used become very important.

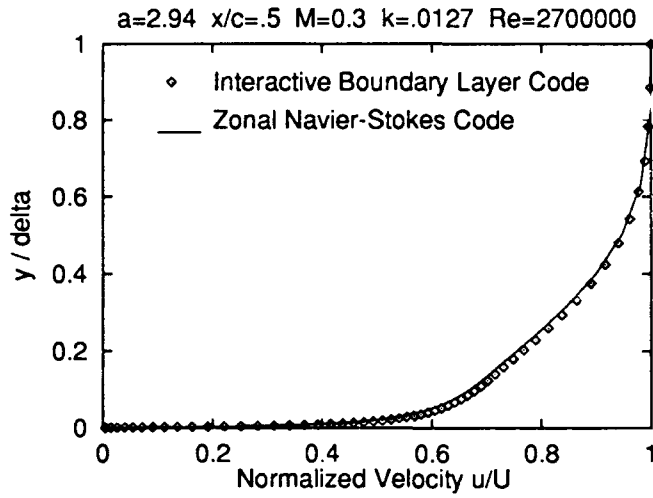


Figure 4.39: Comparison of computed boundary layer with an interactive boundary layer program at the 90% chord for $\alpha = 2.94$ degrees.

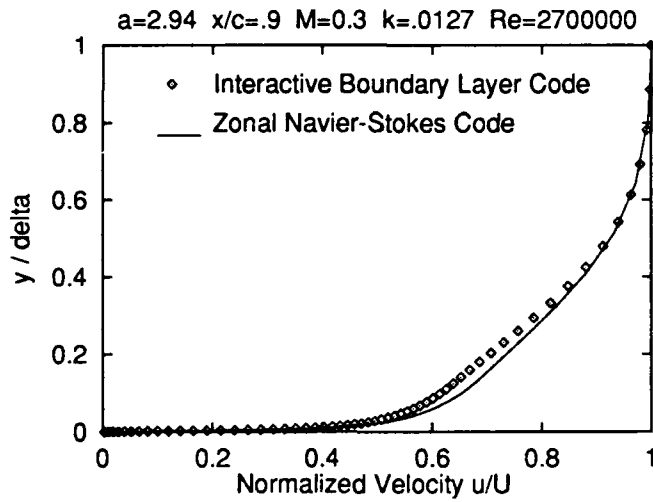


Figure 4.40: Comparison of computed boundary layer with an interactive boundary layer program at the 90% chord for $\alpha = 2.94$ degrees.

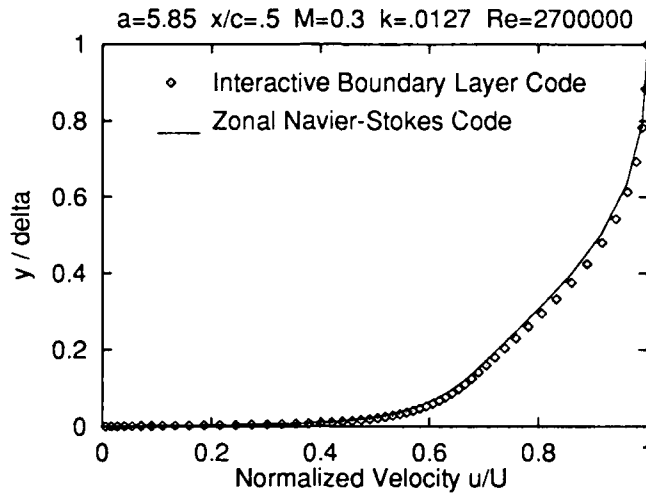


Figure 4.41: Comparison of computed boundary layer with an interactive boundary layer program at the 50% chord for $\alpha = 5.85$ degrees.

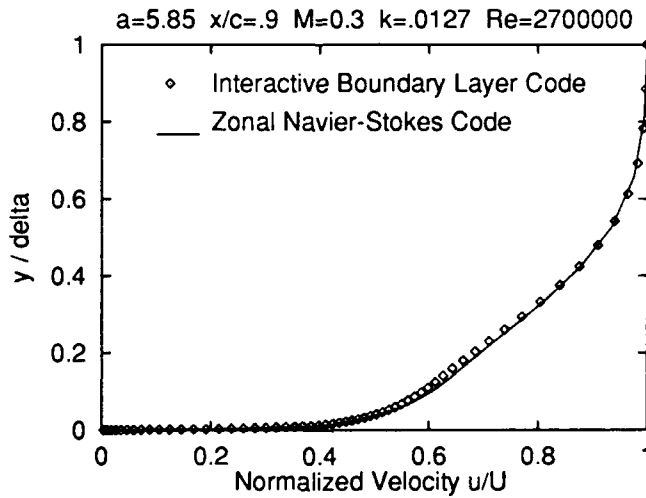


Figure 4.42: Comparison of computed boundary layer with an interactive boundary layer program at the 90% chord for $\alpha = 5.85$ degrees.

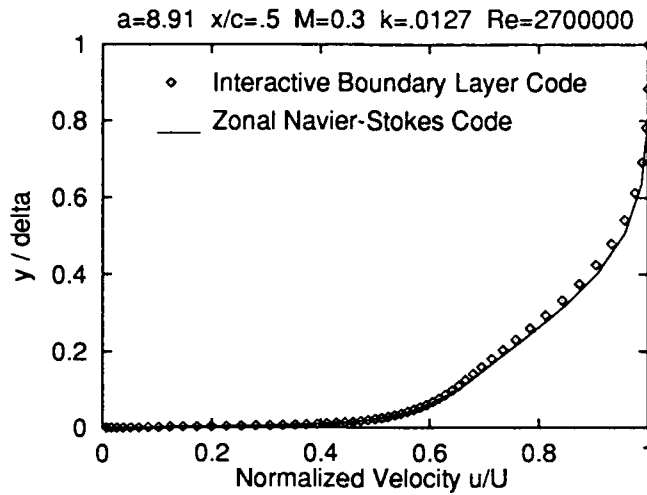


Figure 4.43: Comparison of computed boundary layer with an interactive boundary layer program at the 50% chord for $\alpha = 8.91$ degrees.

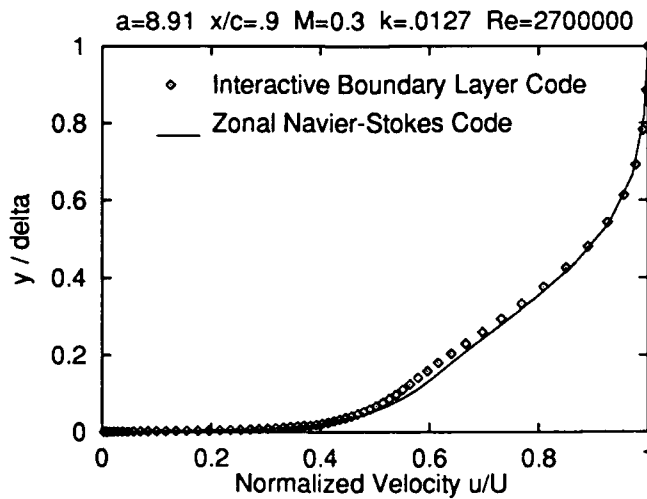


Figure 4.44: Comparison of computed boundary layer with an interactive boundary layer program at the 90% chord for $\alpha = 8.91$ degrees.

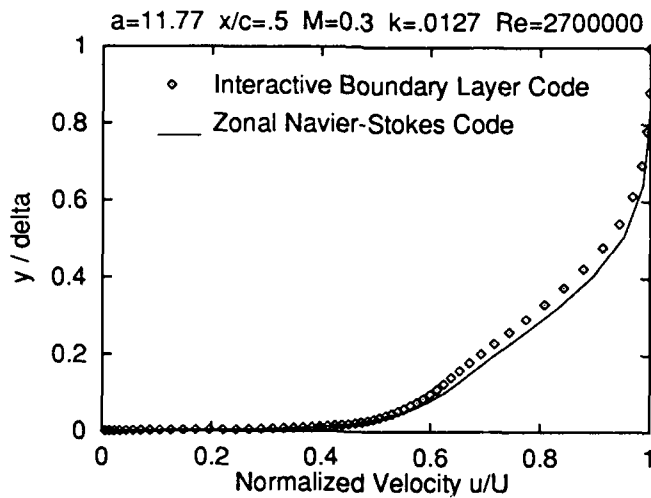


Figure 4.45: Comparison of computed boundary layer with an interactive boundary layer program at the 50% chord for $\alpha = 11.77$ degrees.

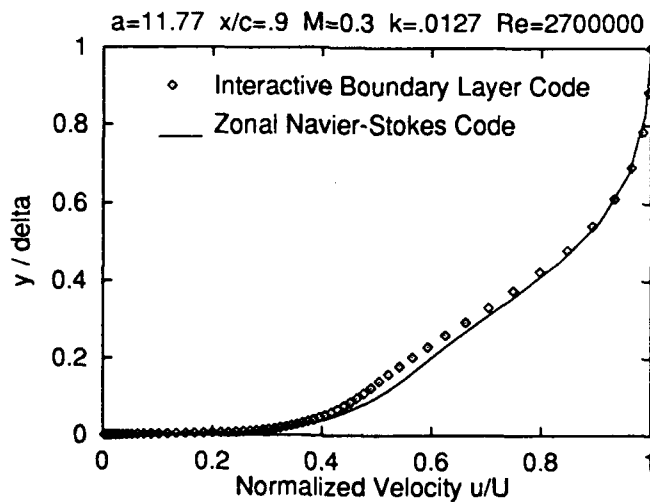


Figure 4.46: Comparison of computed boundary layer with an interactive boundary layer program at the 90% chord for $\alpha = 11.77$ degrees.

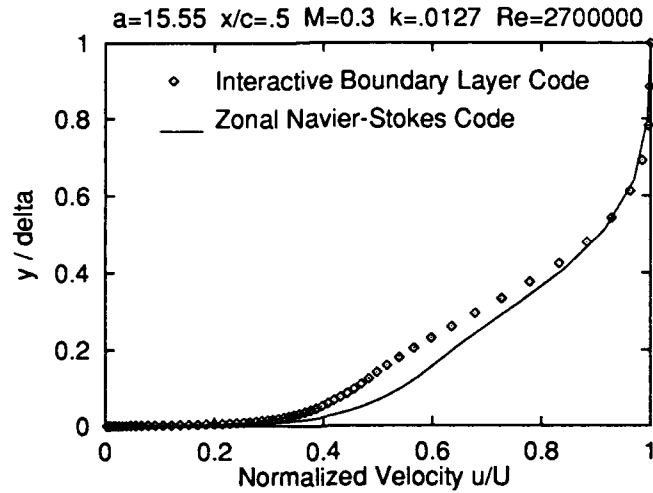


Figure 4.47: Comparison of computed boundary layer with an interactive boundary layer program at the 50% chord for $\alpha = 15.55$ degrees.

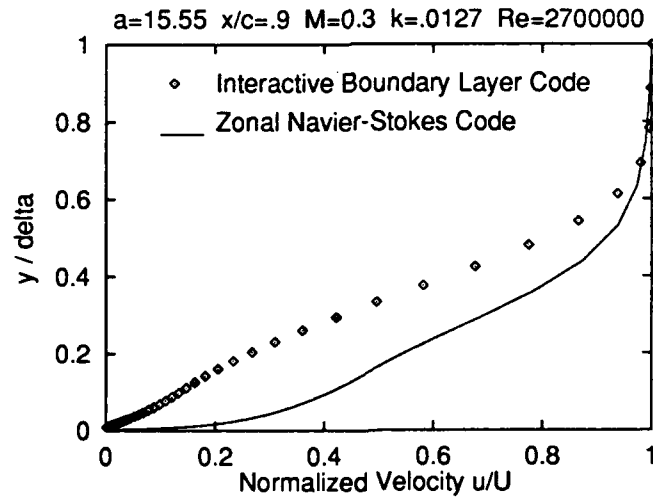


Figure 4.48: Comparison of computed boundary layer with an interactive boundary layer program at the 90% chord for $\alpha = 15.55$ degrees.

2. Computed Ramp Flow Details

In this section, flow features of the computed ramp motion are shown. These features are demonstrated by the density contour lines, Mach contour lines, vorticity contour lines and mass-flux contours. The contour lines represent areas of the flowfield, for which the parameter of interest, remains constant. Clustered contour lines represent areas where the parameter is rapidly changing.

In figures, 4.49 through 4.64, density, Mach number, vorticity and mass-flux contours are displayed for $\alpha = 1.86^\circ$ to $\alpha = 17.50^\circ$. In figures 4.65 through 4.110 the Mach number contours are replaced by pressure contours. This was done because the strong gradients, caused by the vortices, tend to not give clear Mach number information.

In figure 4.63, $\alpha = 16.50^\circ$, the beginning of a vortex is visible near the leading edge. At $\alpha = 17.00^\circ$, in figure 4.64 the vortex has moved 5% of chord downstream, and another vortex is starting at the leading edge. At $\alpha = 19.00^\circ$ the first two vortices merge into one stronger vortex located near the 50% chord point. Two smaller vortices are also clearly visible in the mass-flux contours of figure 4.68. The original vortex now detaches from the surface of the airfoil at 19.50° . At $\alpha = 20.50^\circ$, a second vortex is shed from the leading edge area, and the vortex shown at 19.5° has moved to the trailing edge. At $\alpha = 22.50^\circ$, the trailing edge vortex has been shed downstream. The whole process seems to repeat itself at a faster rate, as can be seen in the remaining figures as the airfoil ramps up to 30° . The dynamic stall phenomenon is observed in terms of density, pressure and vorticity. The nose-down pitching moment is caused by the vortex sitting at the trailing edge. It is important that the vortices do not dissipate and do not get distorted as they pass through the zonal interface.

Next the solution was continued to angles beyond stall. Traces of alternate vortex shedding from the trailing edge can be seen at $\alpha \approx 27^\circ$. At high angles of incidence the alternating vortex shedding is very well demonstrated in figures 4.91 through 4.110. These computed solutions are in general agreement with the findings of the experimental investigations of Chandrasekhar et al. Also it can be seen that the zonal method developed is capable of computing unsteady flows at very high angles-of-attack showing at least qualitative agreement with the experiment.

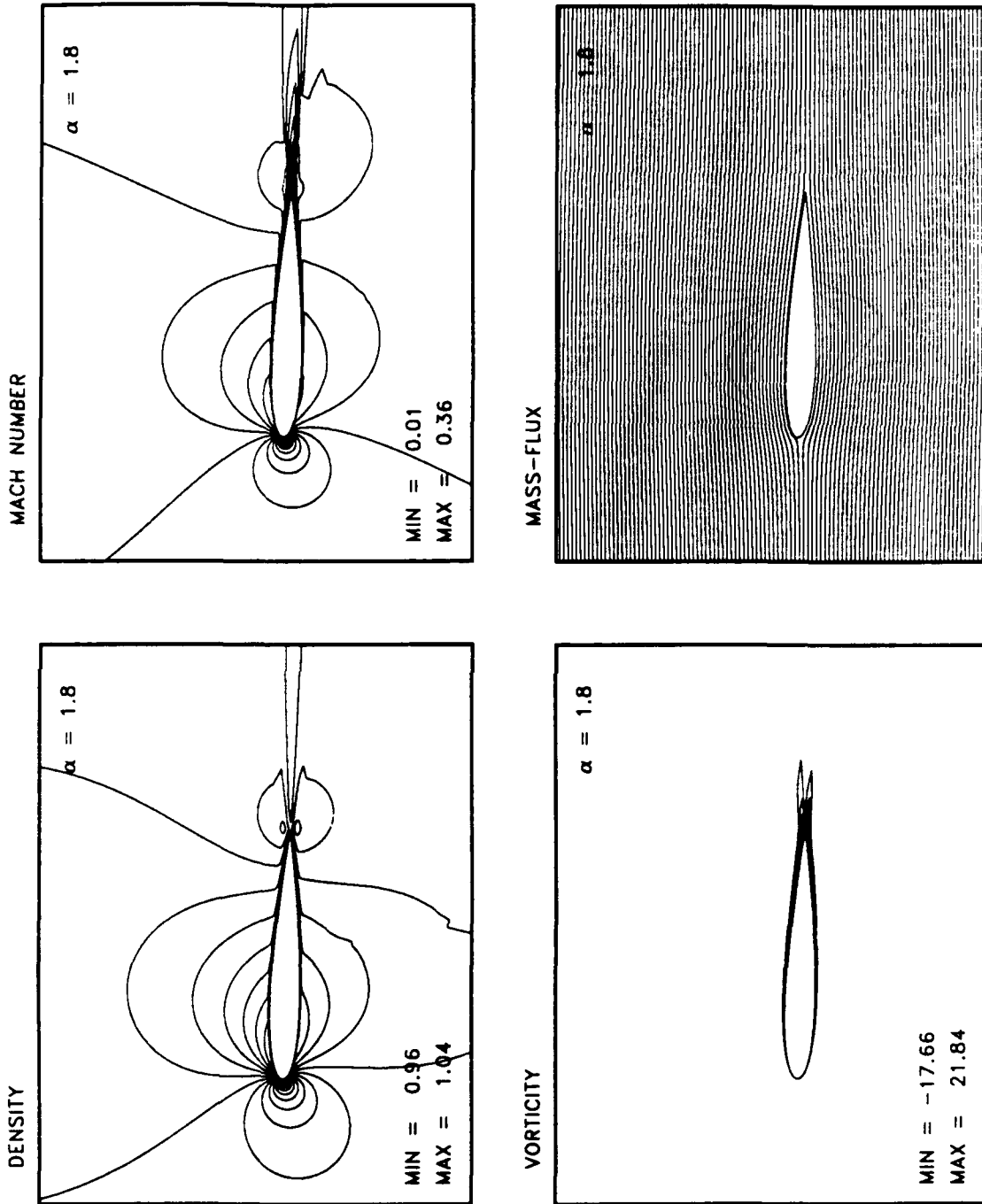


Figure 4.49: Ramp Motion Flow Details, $M_\infty = .3$, $k = .0127$, $Re = 2.7 \times 10^6$, $\alpha \approx 1.86^\circ$.

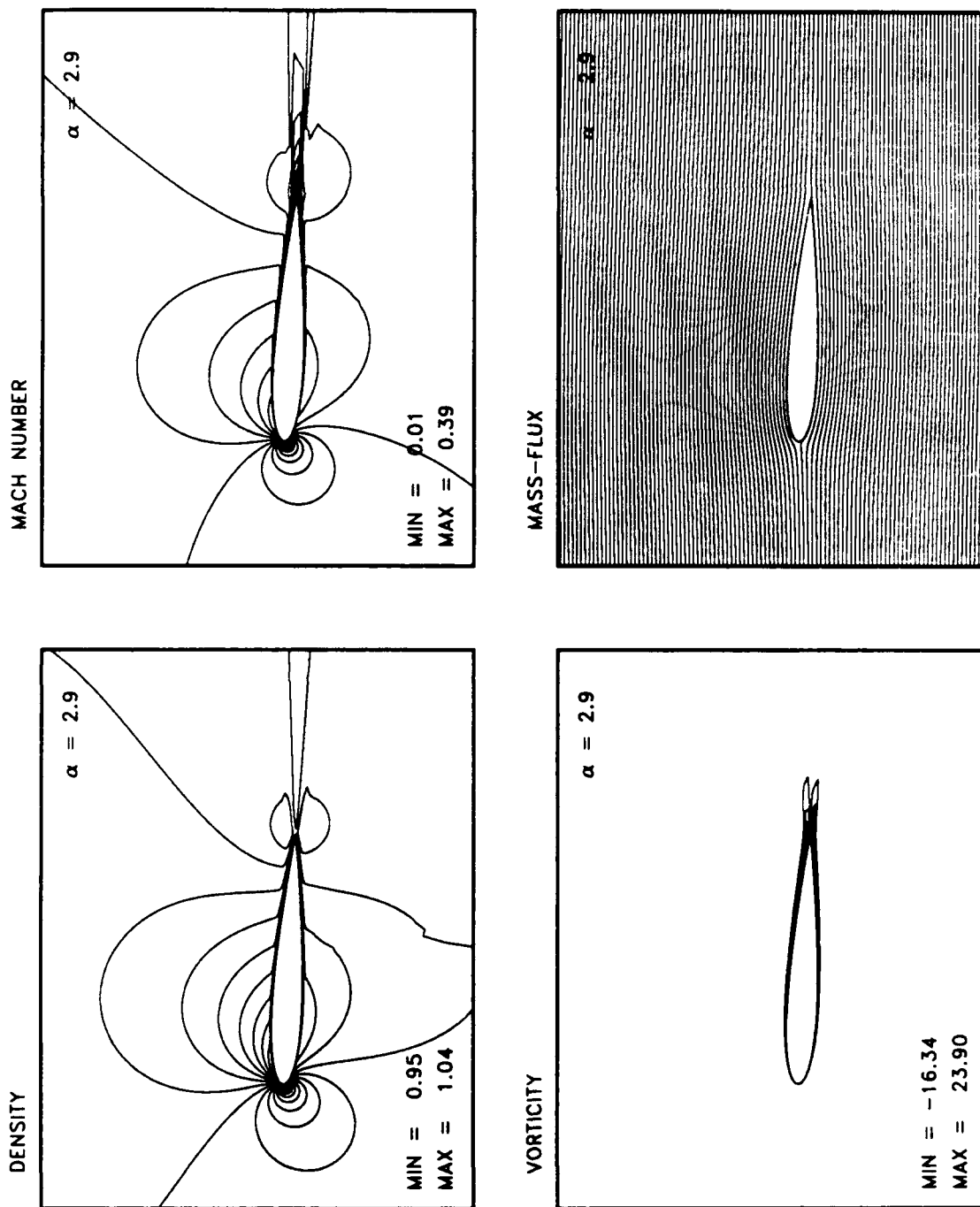


Figure 4.50: Ramp Motion Flow Details, $M_\infty = .3$, $k = .0127$, $Re = 2.7 \times 10^6$, $\alpha = 2.94^\circ$.

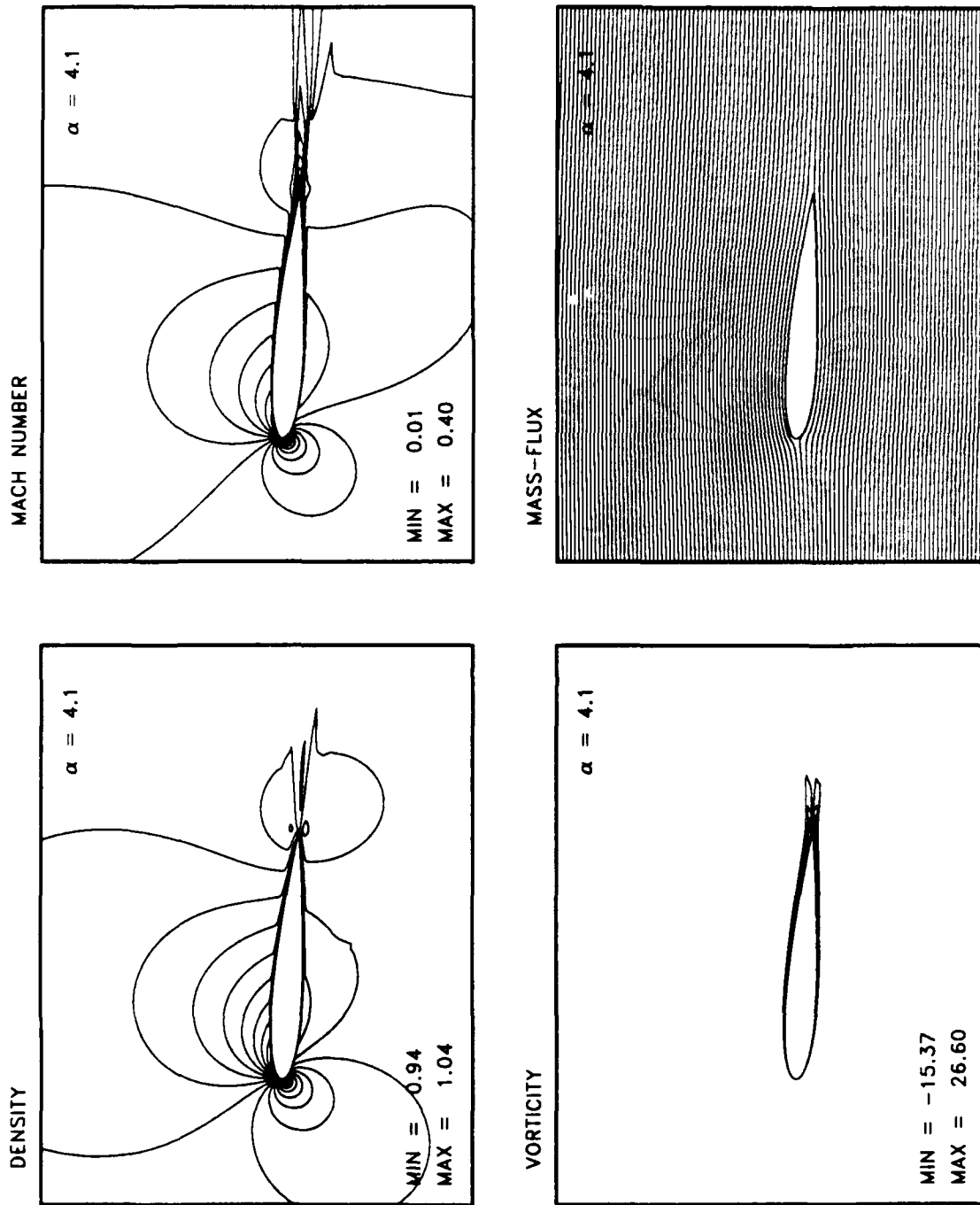


Figure 4.51: Ramp Motion Flow Details, $M_\infty = .3$, $k = .0127$, $Re = 2.7 \times 10^6$, $\alpha = 4.14^\circ$.

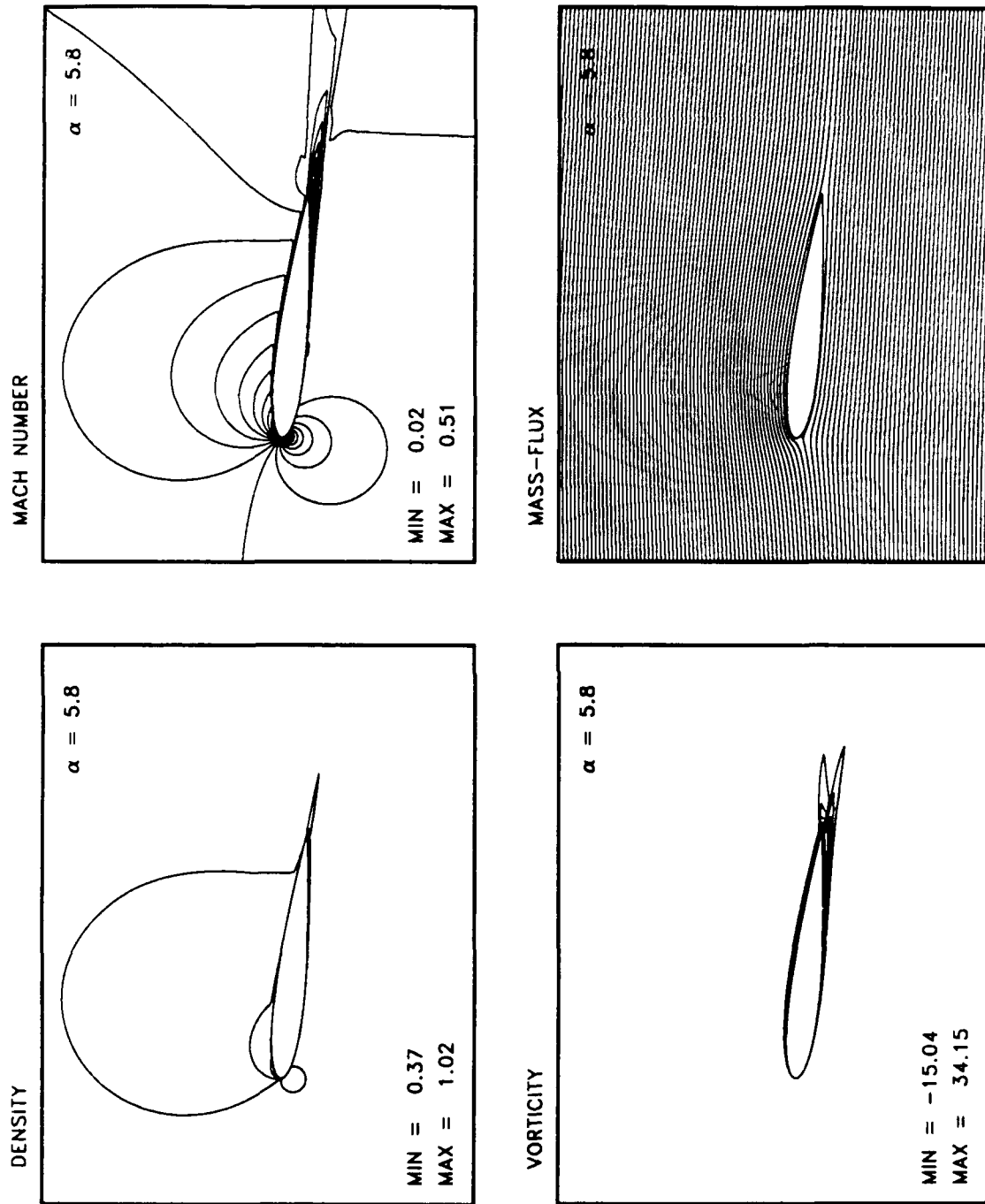


Figure 4.52: Ramp Motion Flow Details, $M_\infty = .3$, $k = .0127$, $Re = 2.7 \times 10^6$, $\alpha = 5.85^\circ$.

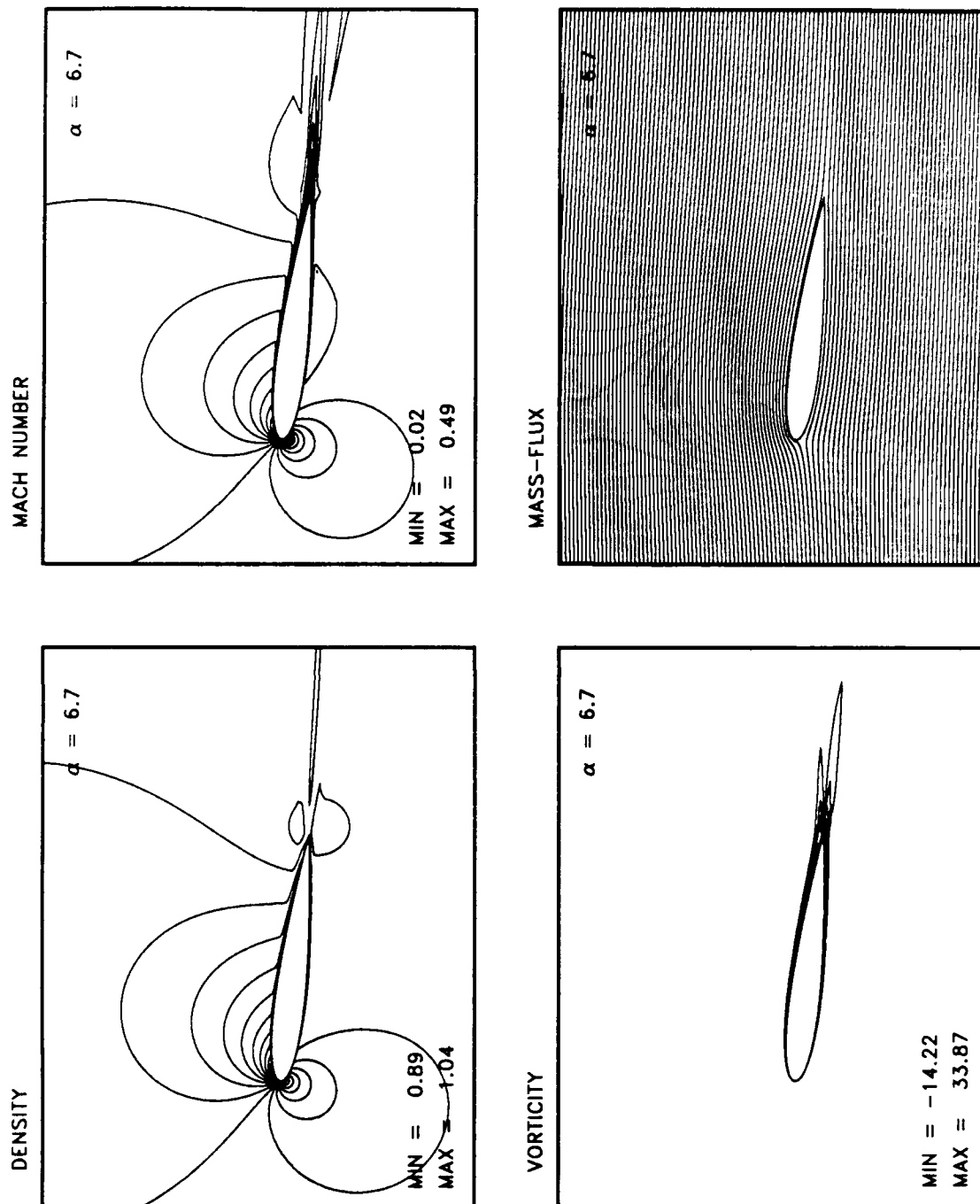


Figure 4.53: Ramp Motion Flow Details, $M_\infty = .3$, $k = .0127$, $Re = 2.7 \times 10^6$. $\alpha = 6.72^\circ$.

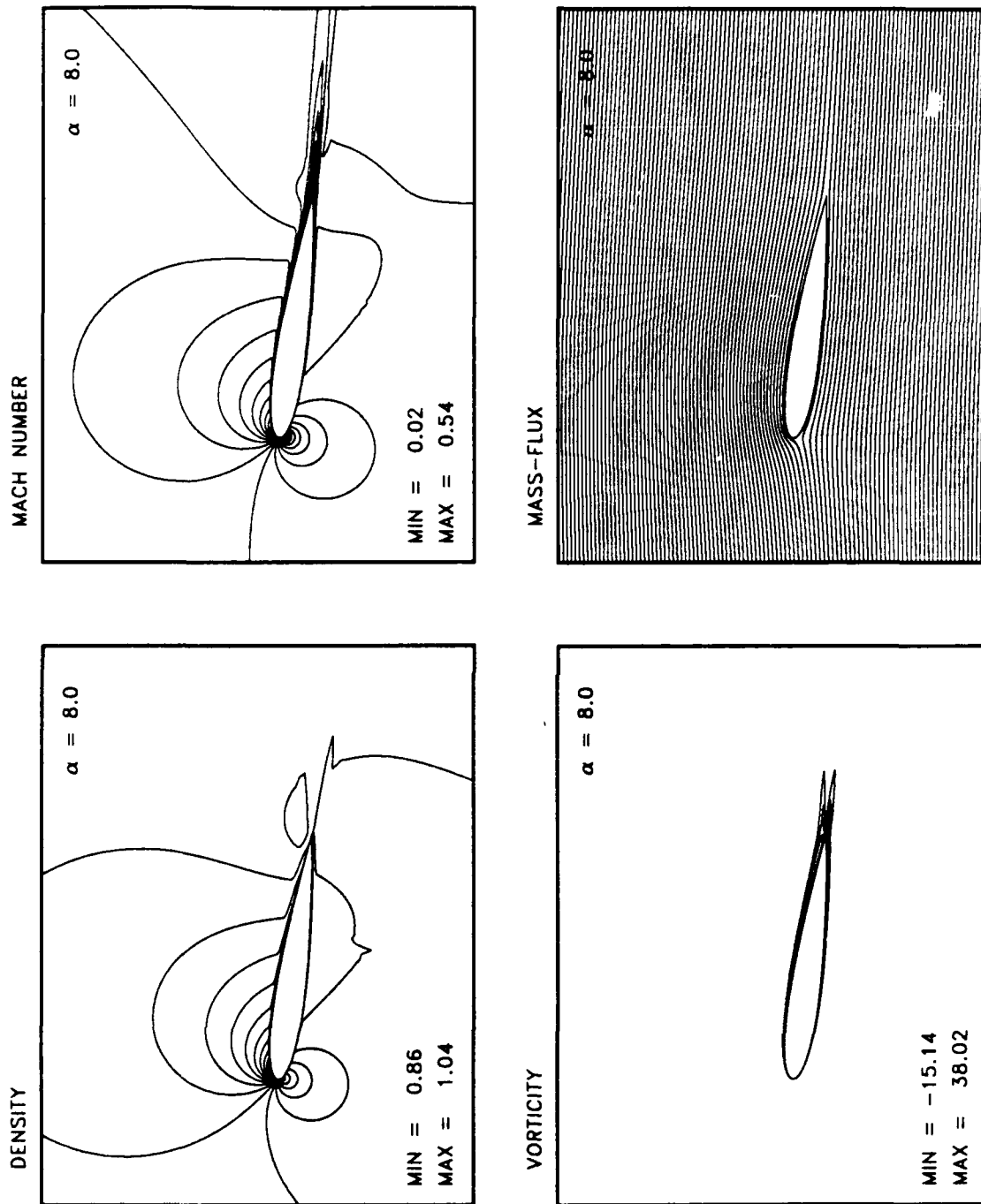


Figure 4.54: Ramp Motion Flow Details, $M_\infty = .3$, $k = .0127$, $Re = 2.7 \times 10^6$, $\alpha = 8.02^\circ$.

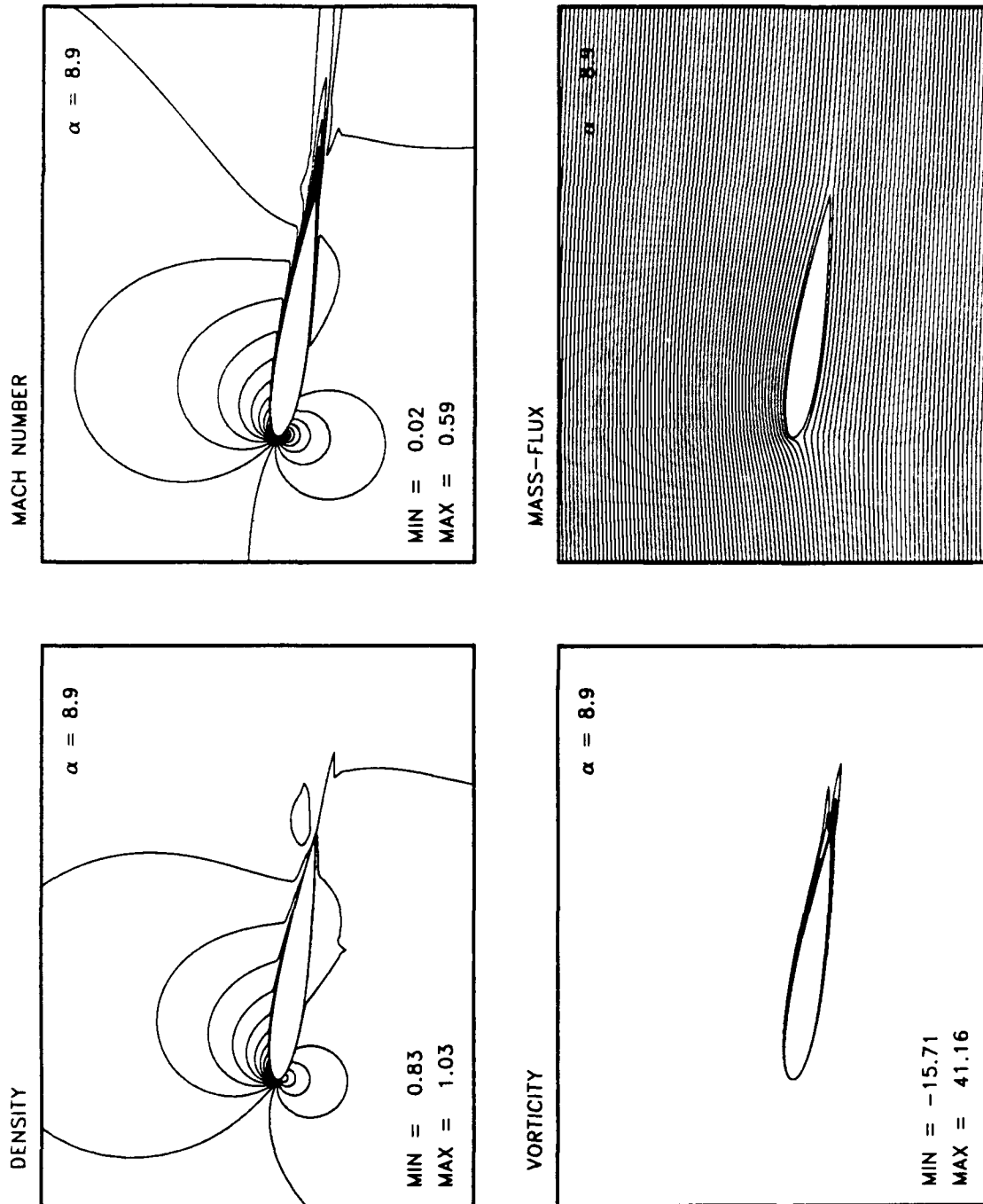


Figure 4.55: Ramp Motion Flow Details, $M_\infty = .3$, $k = .0127$, $Re = 2.7 \times 10^6$. $\alpha = 8.91^\circ$.

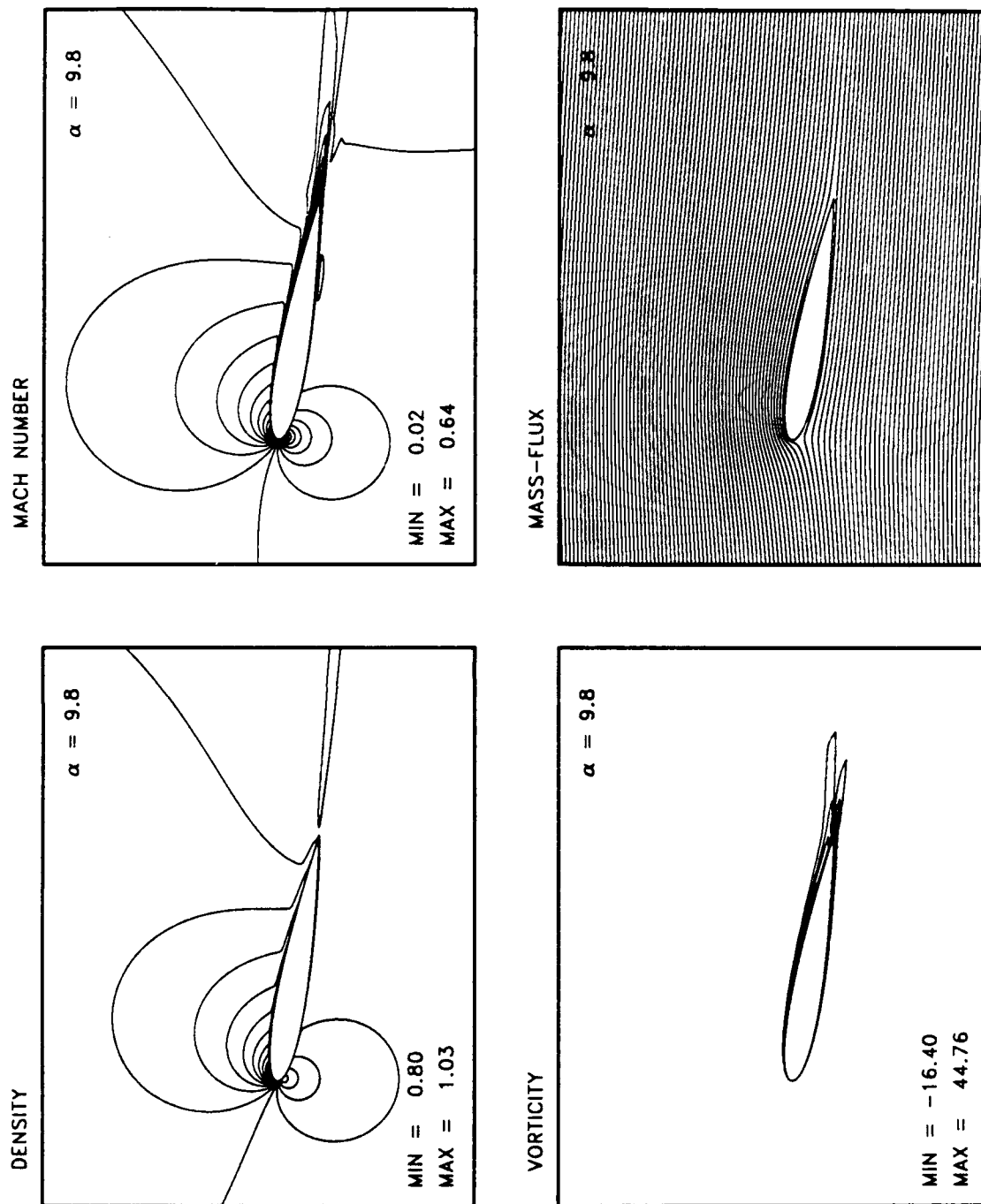


Figure 4.56: Ramp Motion Flow Details, $M_\infty = .3$, $k = .0127$, $Re = 2.7 \times 10^6$. $\alpha = 9.85^\circ$.

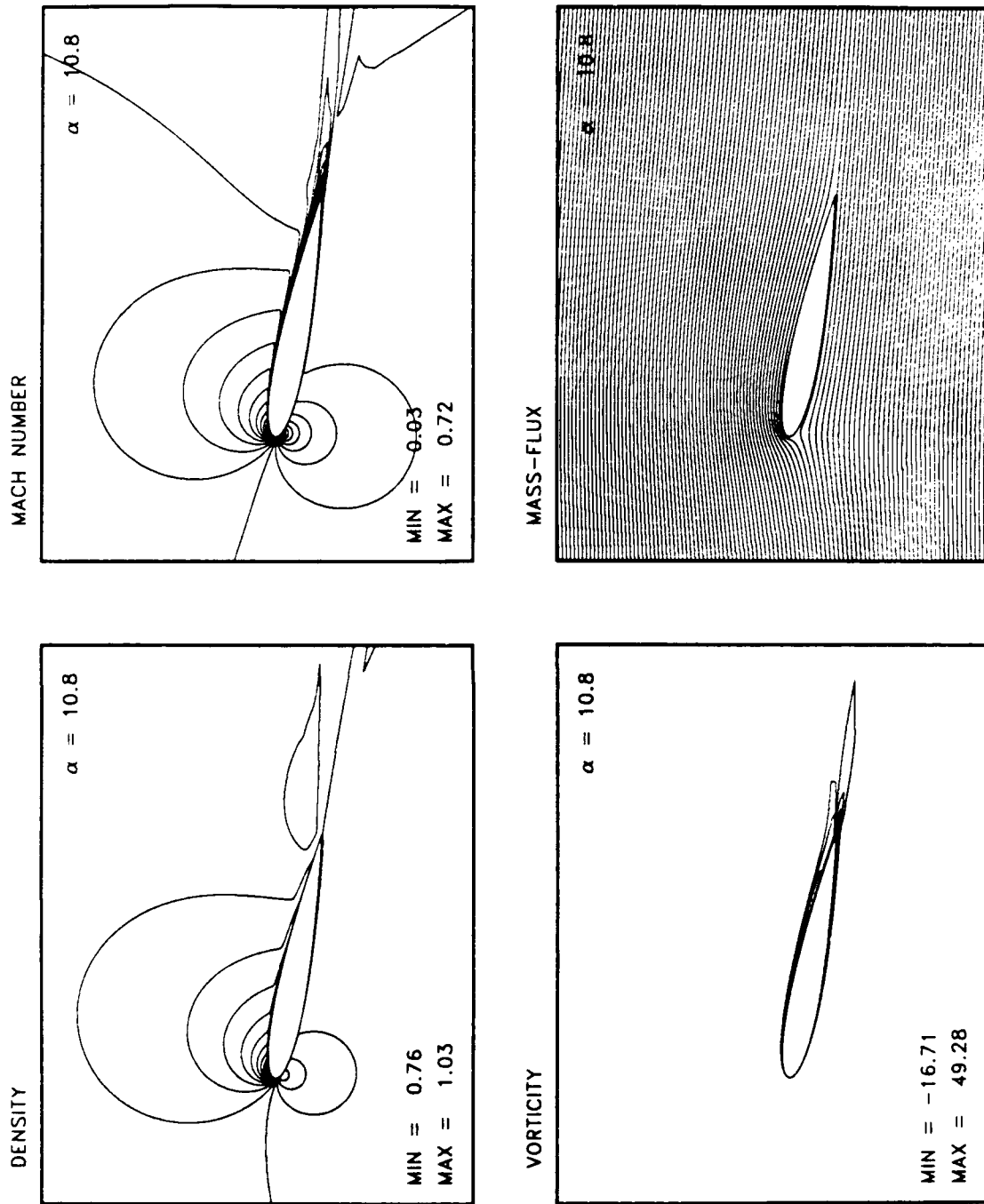


Figure 4.57: Ramp Motion Flow Details, $M_\infty = .3$, $k = .0127$, $Re = 2.7 \times 10^6$, $\alpha = 10.80^\circ$.

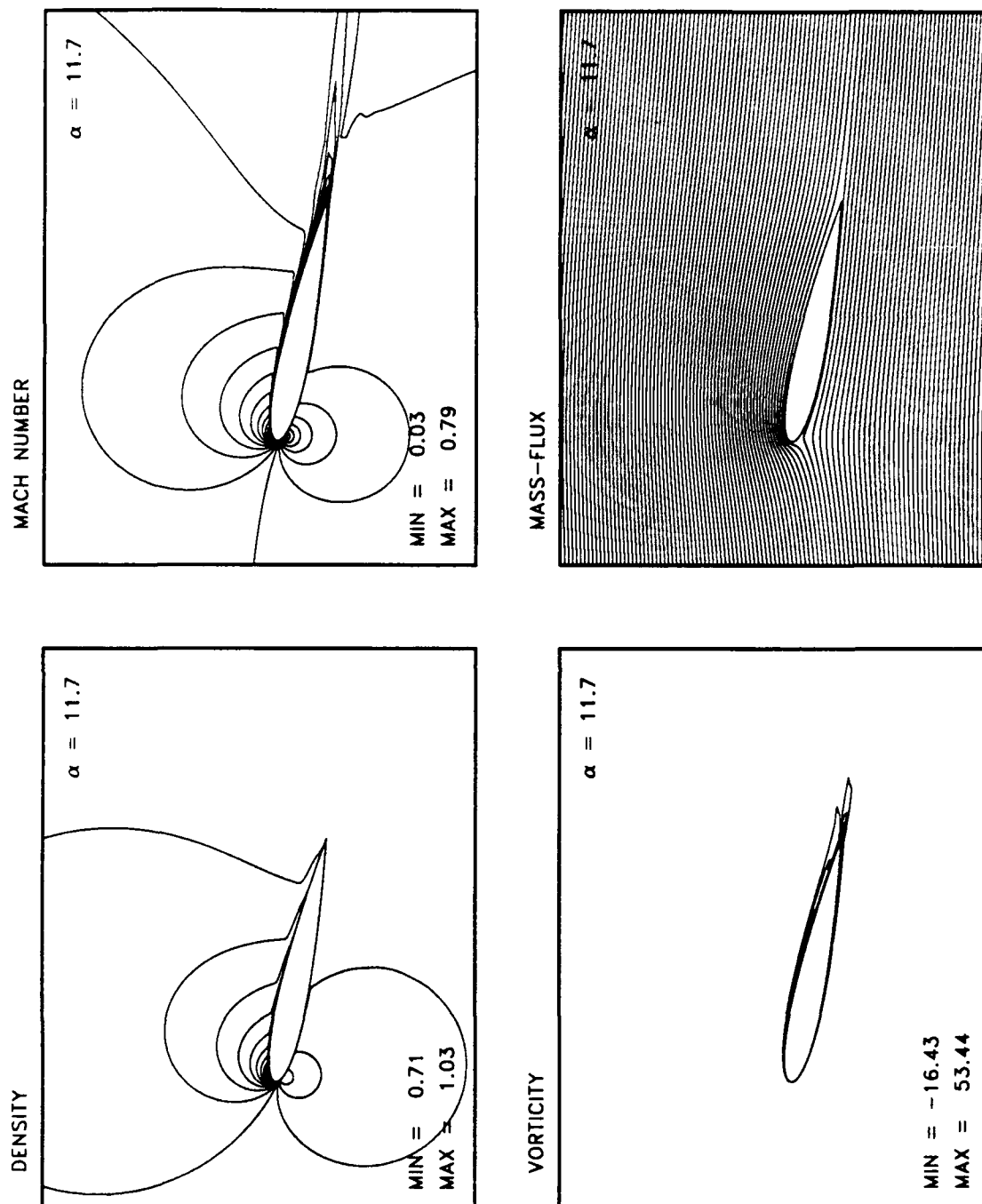


Figure 4.58: Ramp Motion Flow Details, $M_\infty = .3$, $k = .0127$, $Re = 2.7 \times 10^6$, $\alpha = 11.77^\circ$.

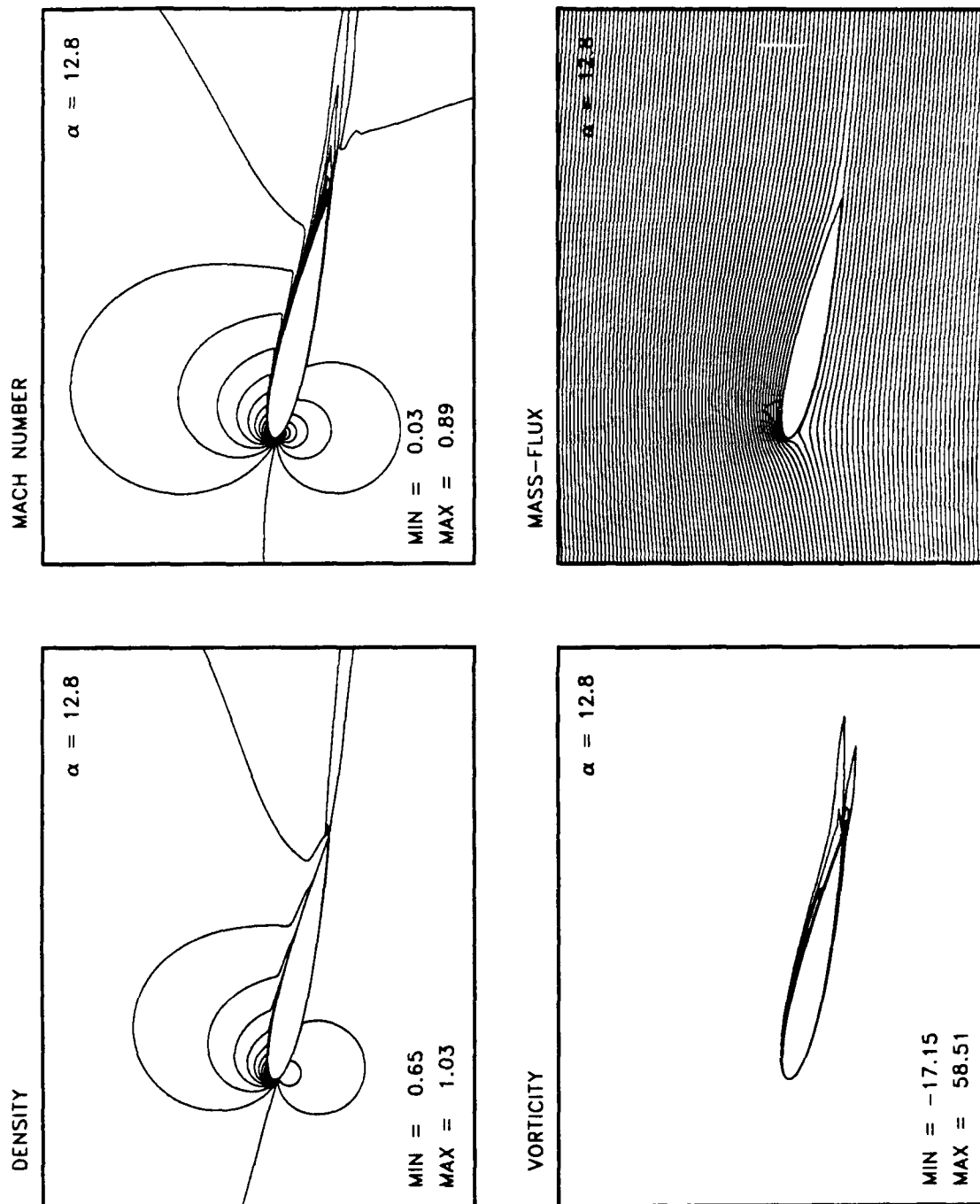


Figure 4.59: Ramp Motion Flow Details, $M_\infty = .3$, $k = .0127$, $Re = 2.7 \times 10^6$, $\alpha = 12.84^\circ$.

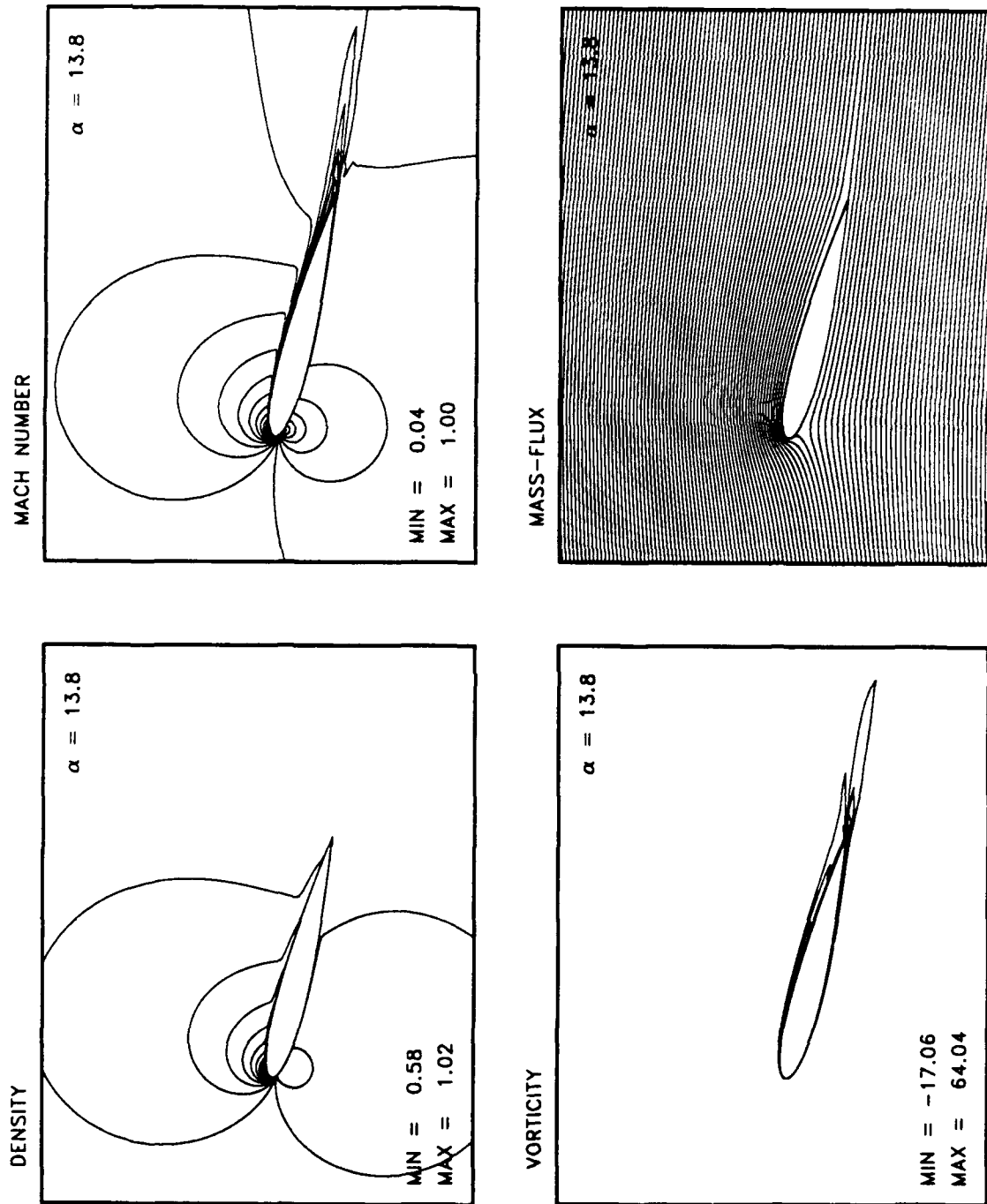


Figure 4.60: Ramp Motion Flow Details, $M_\infty = .3$, $k = .0127$, $Re = 2.7 \times 10^6$, $\alpha = 13.89^\circ$.

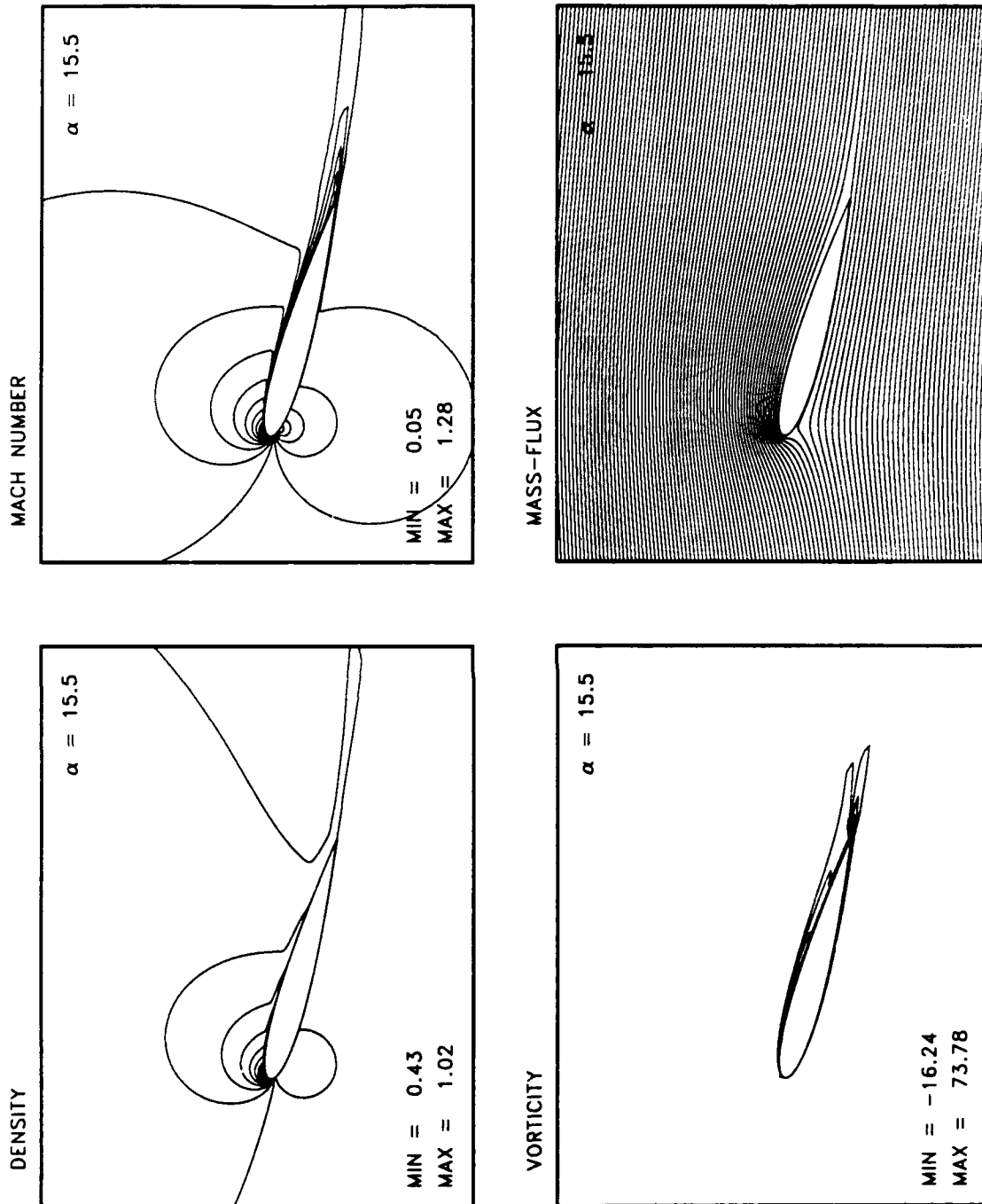


Figure 4.61: Ramp Motion Flow Details, $M_\infty = .3$, $k = .0127$, $Re = 2.7 \times 10^6$, $\alpha = 15.55^\circ$.

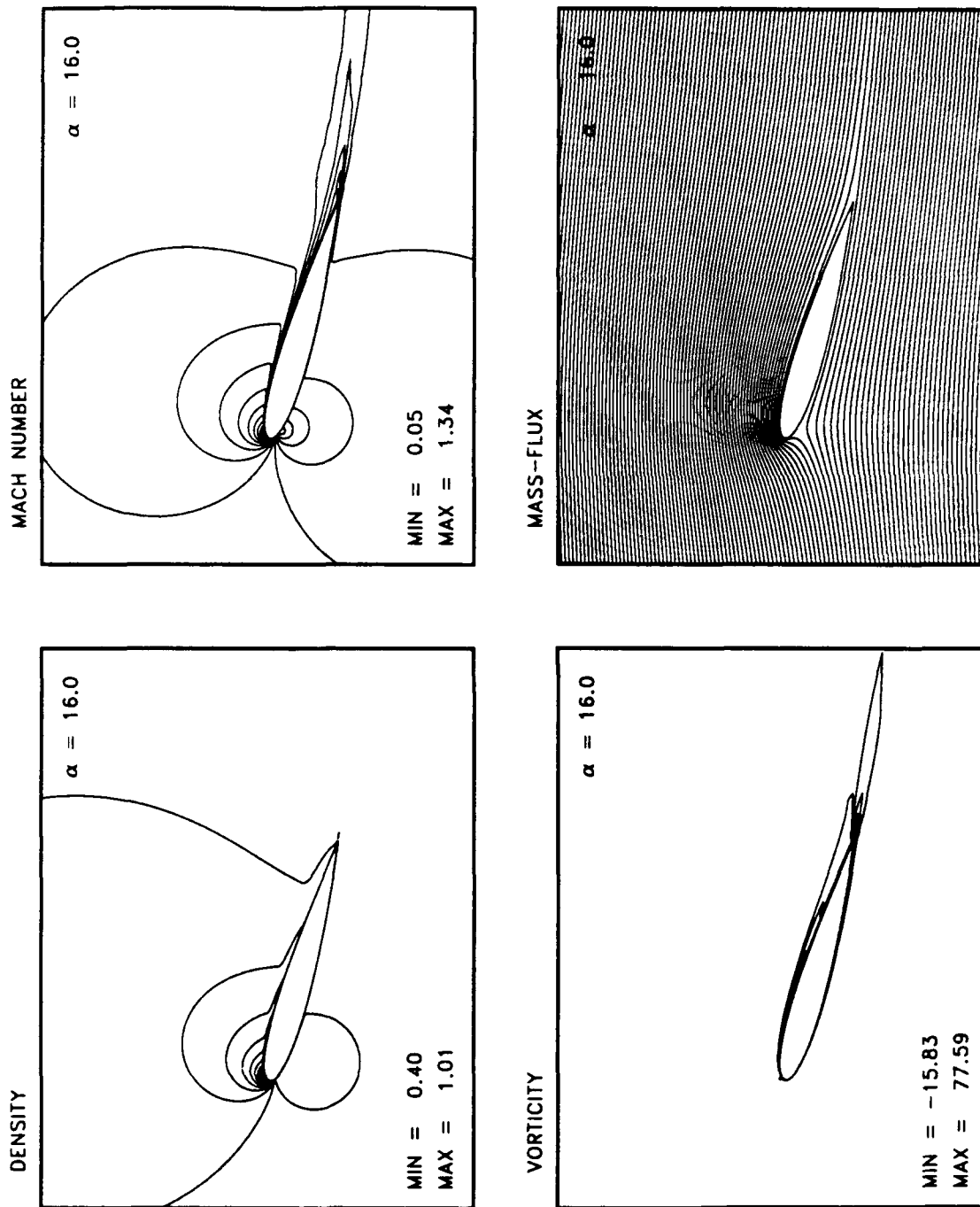


Figure 4.62: Ramp Motion Flow Details, $M_\infty = .3$, $k = .0127$, $Re = 2.7 \times 10^6$, $\alpha = 16.00^\circ$.

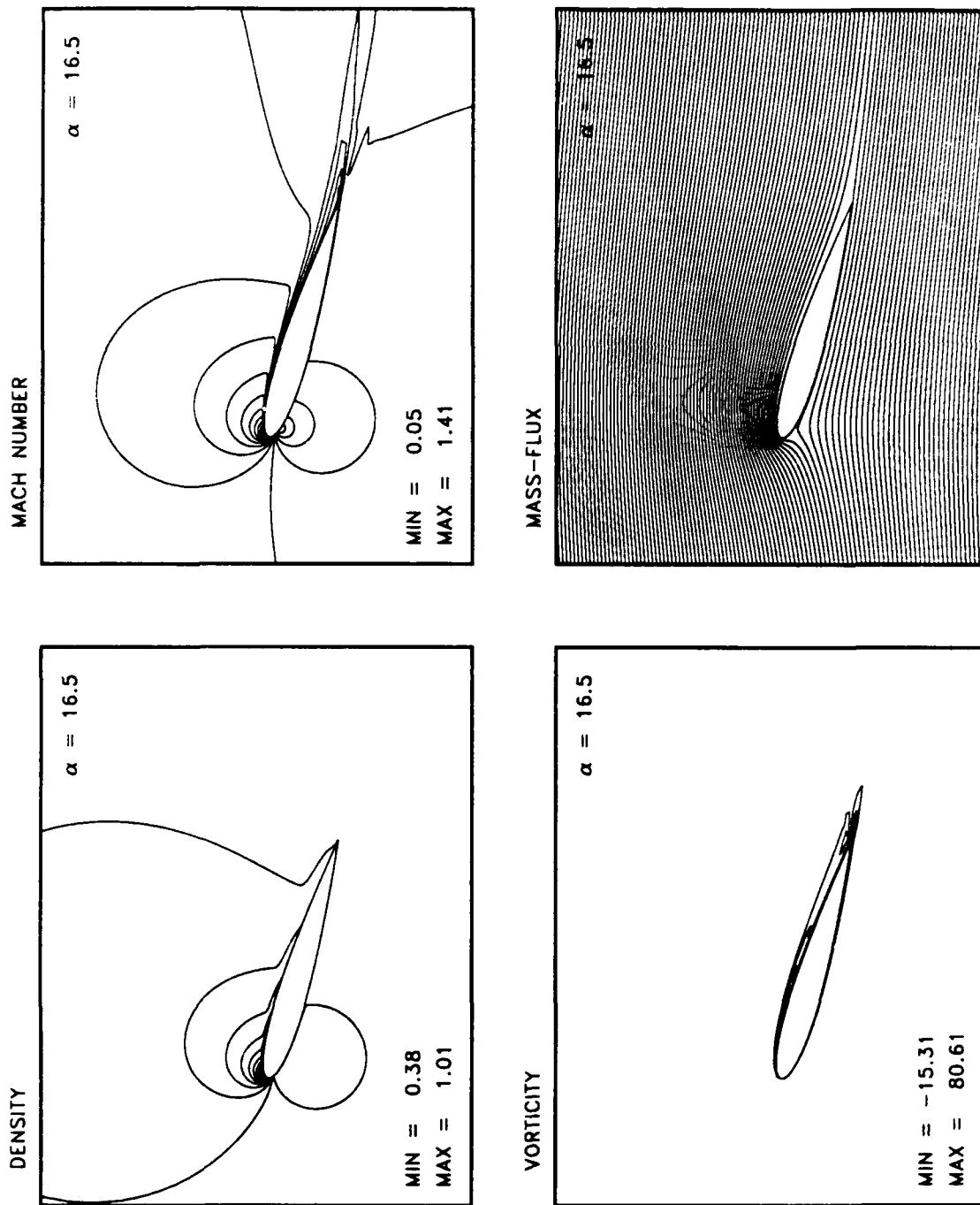


Figure 4.63: Ramp Motion Flow Details. $M_\infty = .3$, $k = .0127$, $Re = 2.7 \times 10^6$. $\alpha = 16.50^\circ$.

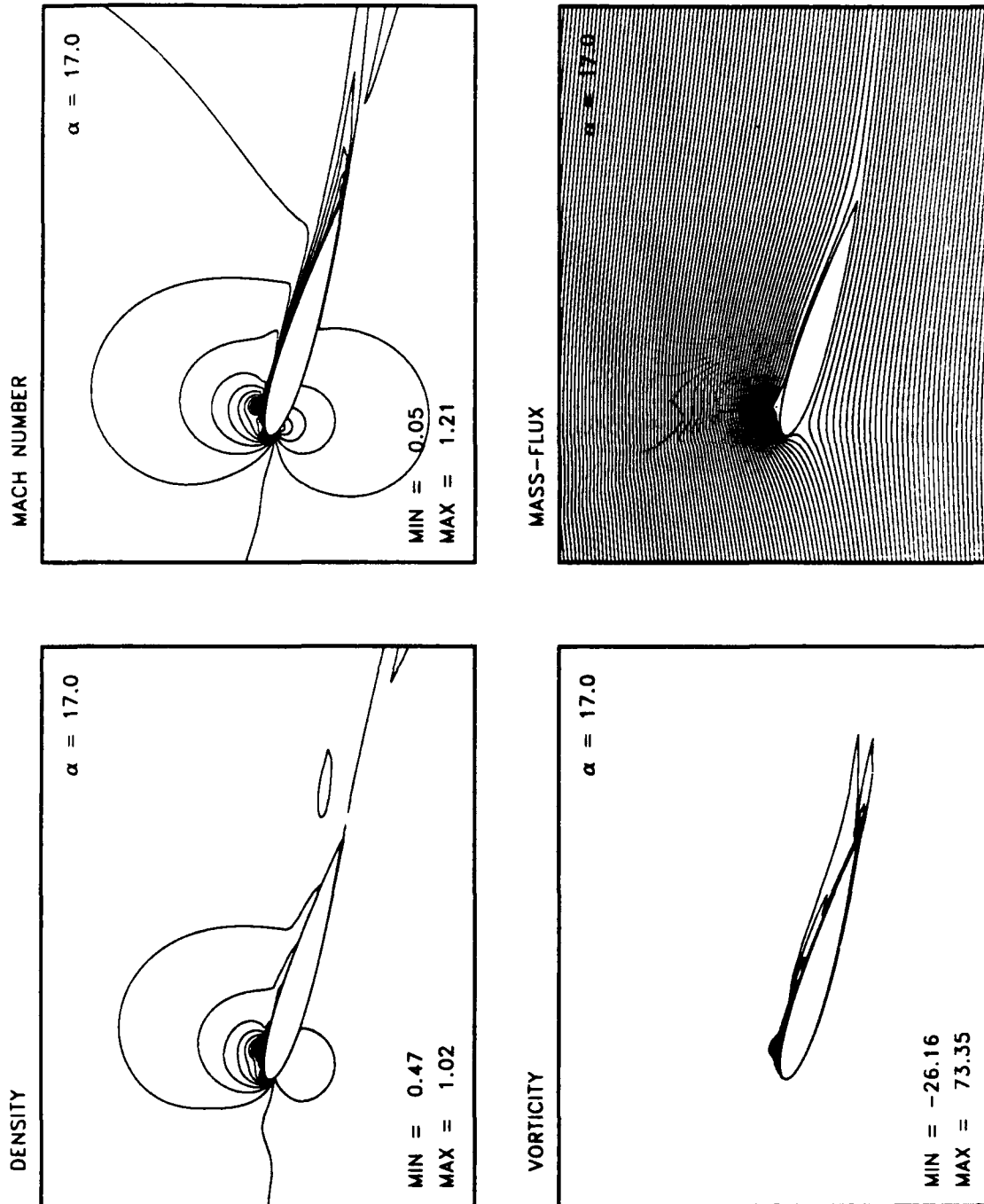


Figure 4.64: Ramp Motion Flow Details, $M_\infty = .3$, $k = .0127$, $Re = 2.7 \times 10^6$, $\alpha = 17.00^\circ$.

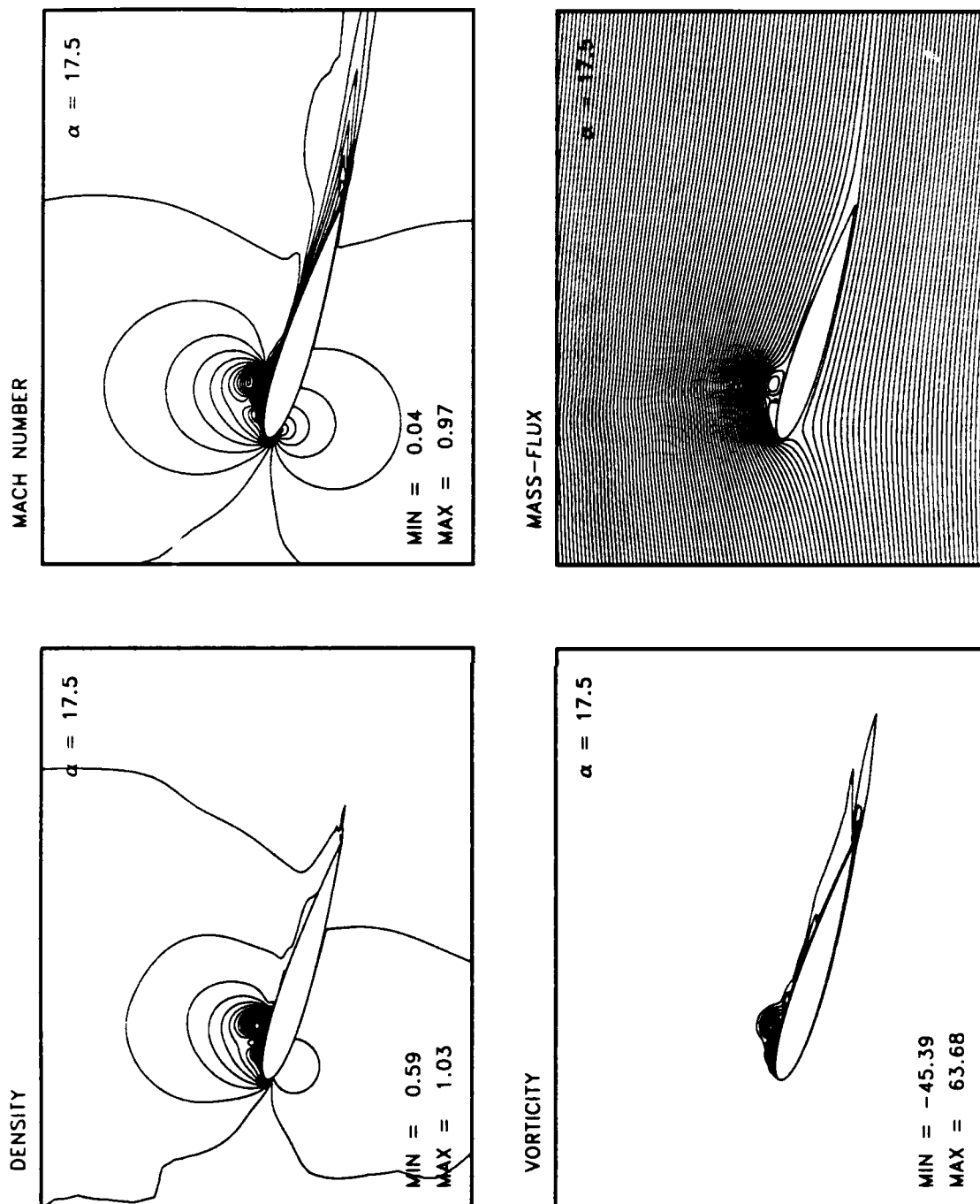


Figure 4.65: Ramp Motion Flow Details, $M_\infty = .3$, $k = .0127$, $Re = 2.7 \times 10^6$, $\alpha = 17.50^\circ$.

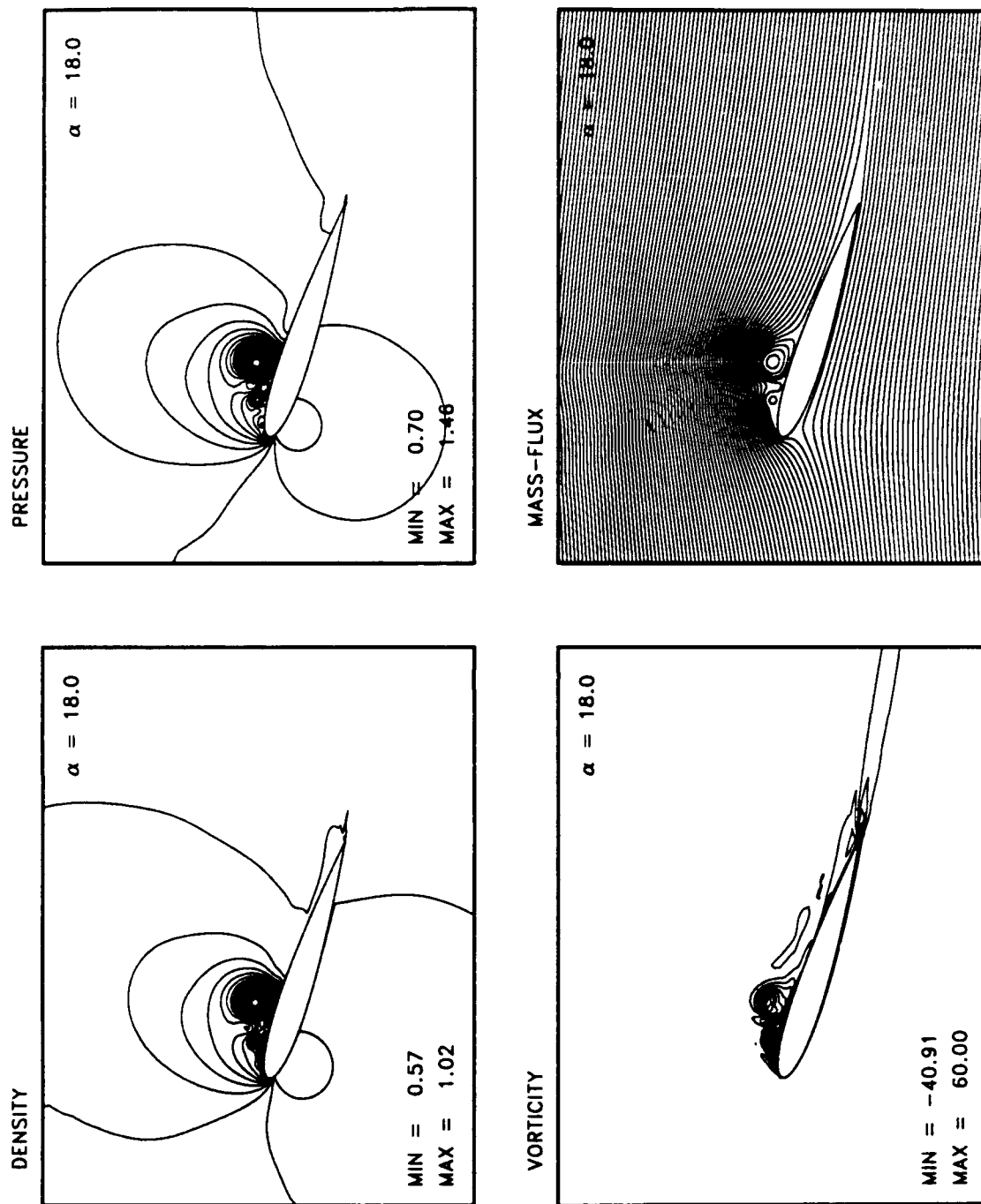


Figure 4.66: Ramp Motion Flow Details, $M_\infty = .3$, $k = .0127$, $Re = 2.7 \times 10^6$, $\alpha = 18.00^\circ$.

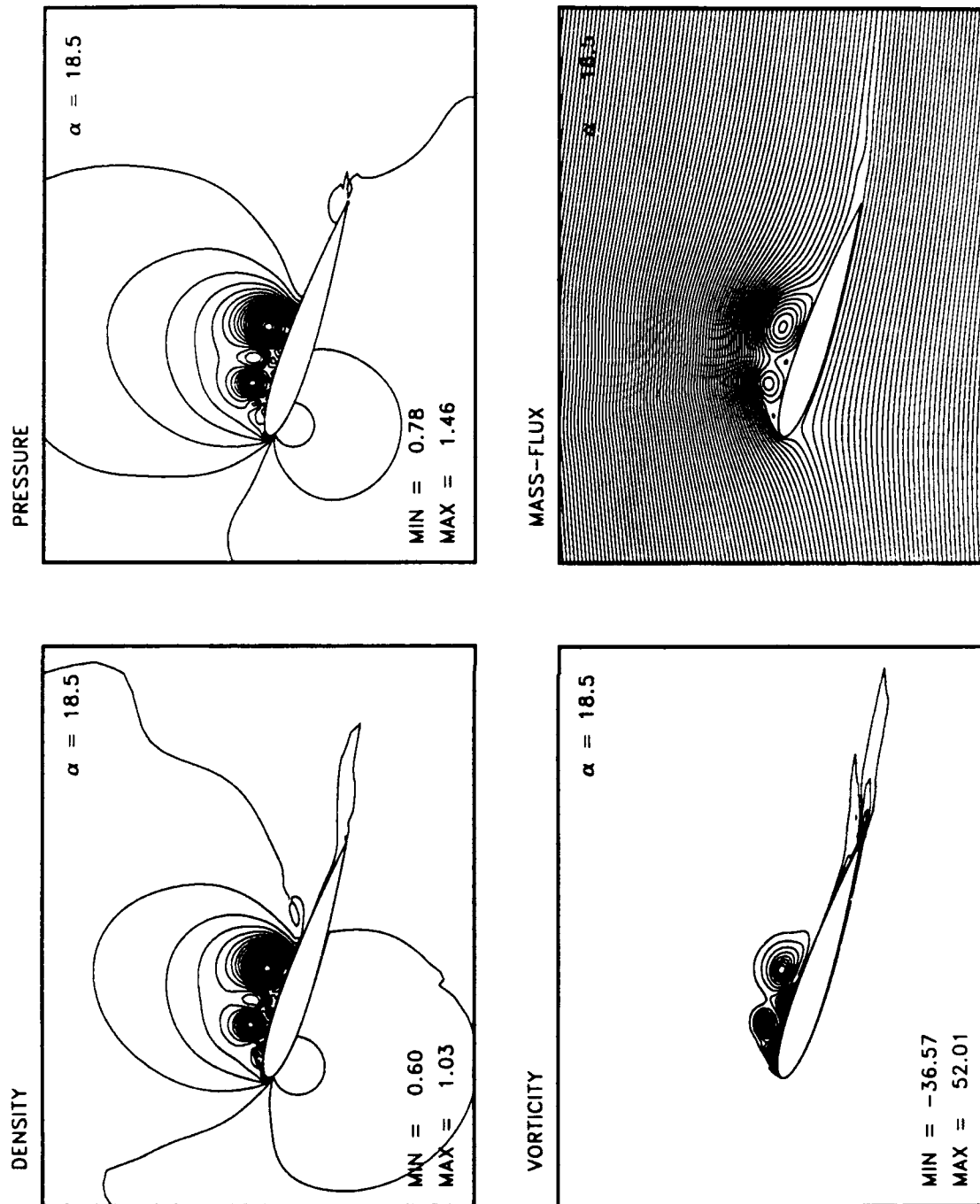


Figure 4.67: Ramp Motion Flow Details, $M_\infty = .3$, $k = .0127$, $Re = 2.7 \times 10^6$. $\alpha = 18.50^\circ$.

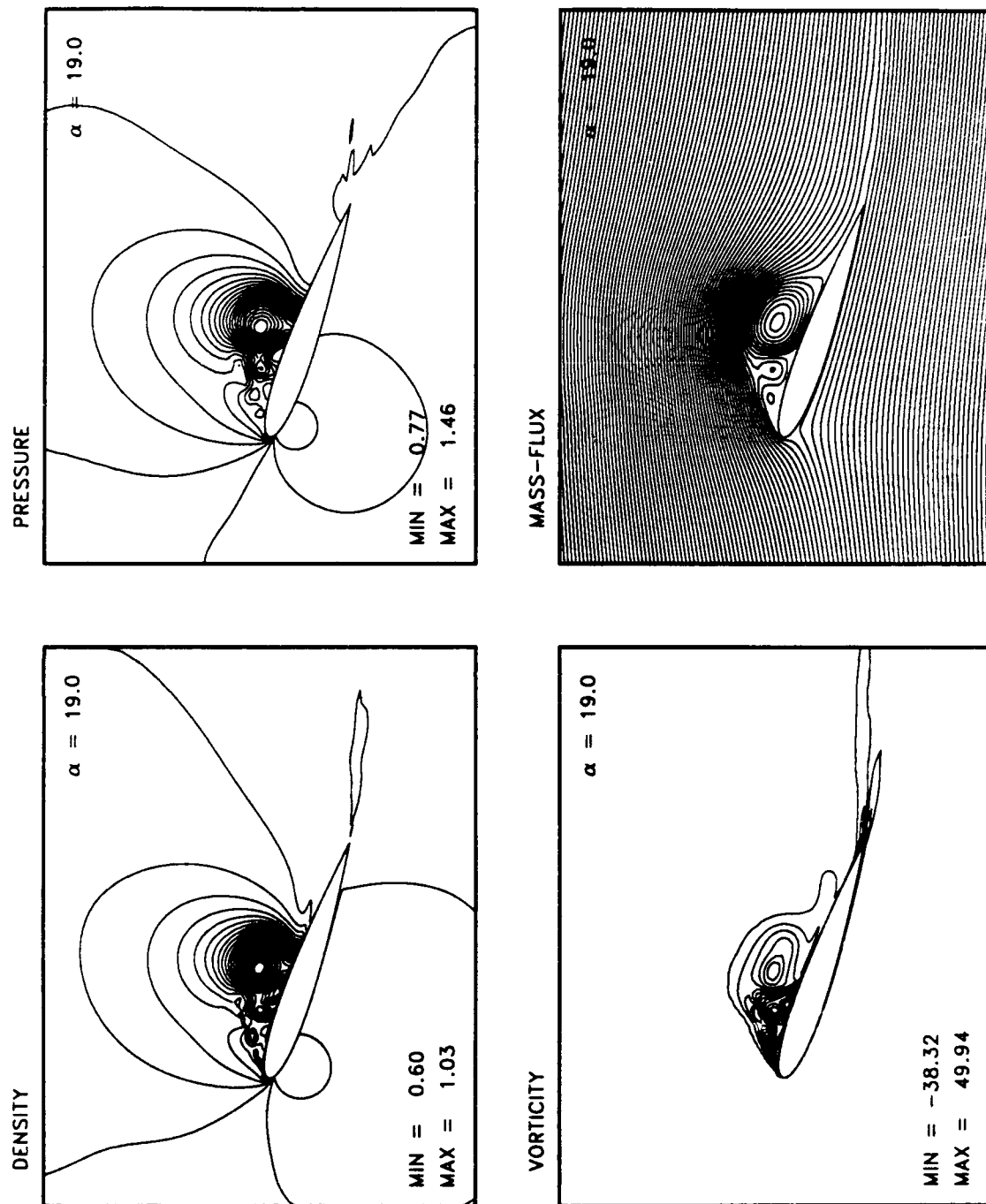


Figure 4.68: Ramp Motion Flow Details, $M_\infty = .3$, $k = .0127$, $Re = 2.7 \times 10^6$, $\alpha = 19.00^\circ$.

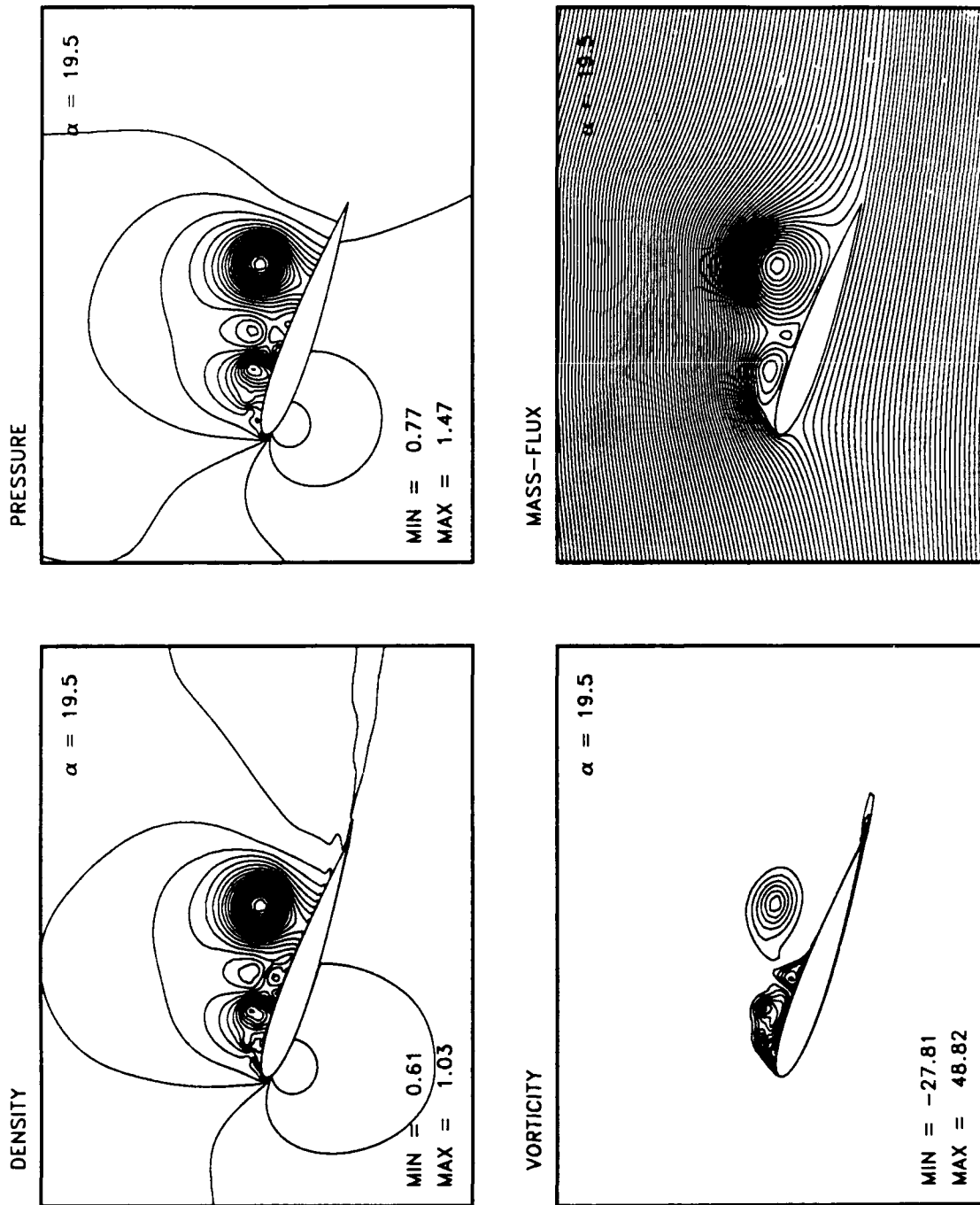


Figure 4.69: Ramp Motion Flow Details, $M_\infty = .3$, $k = .0127$, $Re = 2.7 \times 10^6$. $\alpha = 19.50^\circ$.

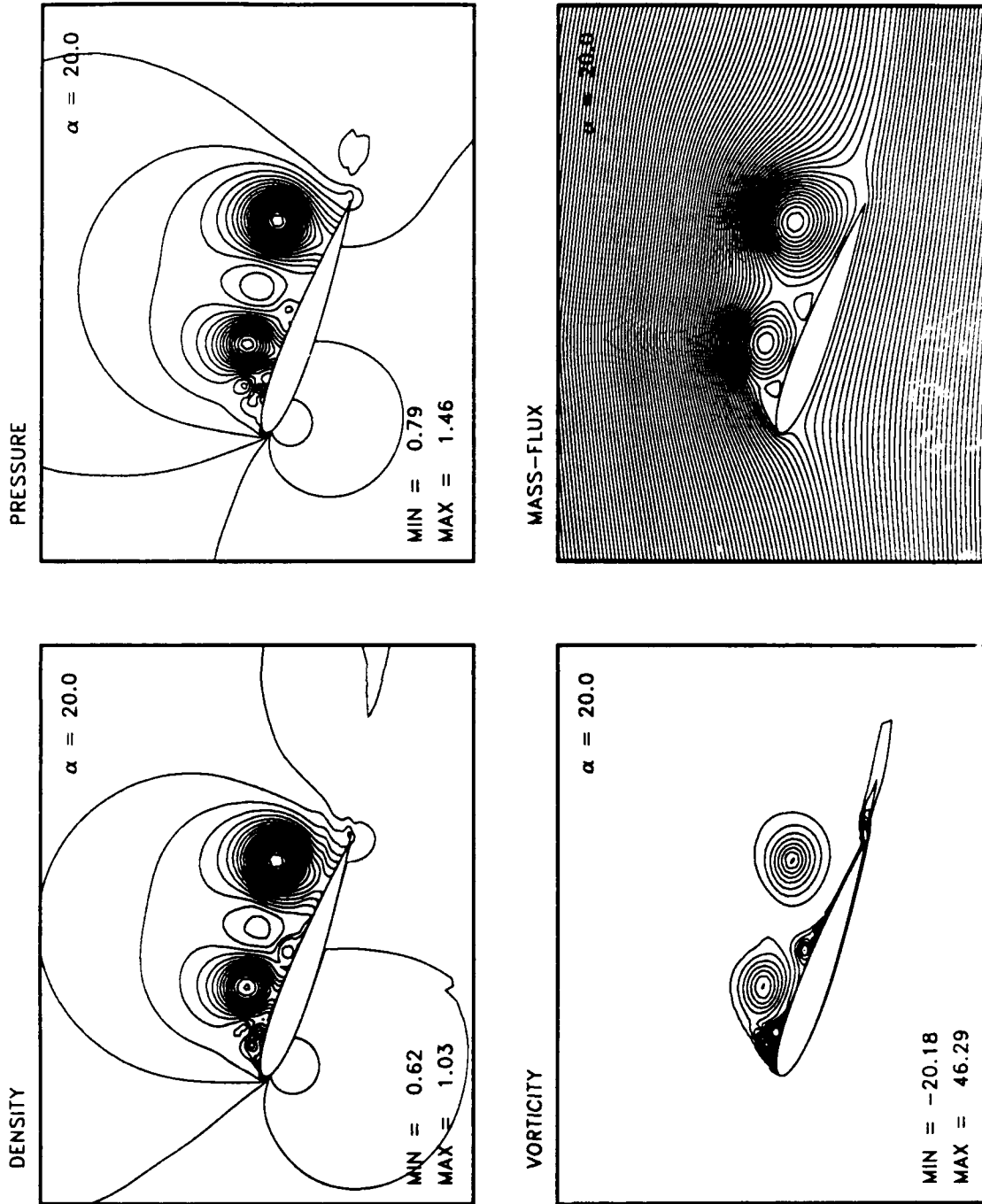


Figure 4.70: Ramp Motion Flow Details, $M_\infty = .3$, $k = .0127$, $Re = 2.7 \times 10^6$. $\alpha = 20.00^\circ$.

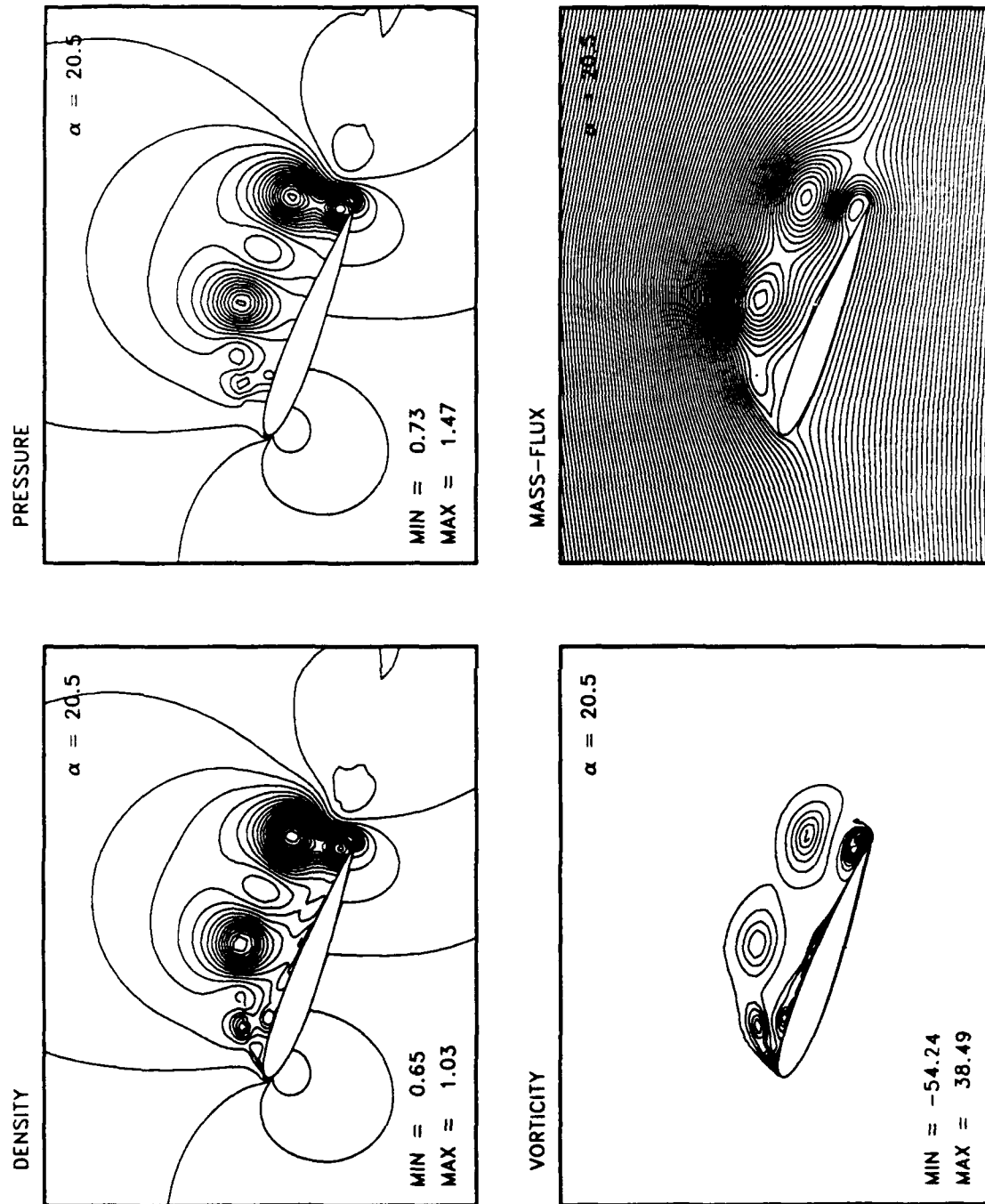


Figure 4.71: Ramp Motion Flow Details, $M_\infty = .3$, $k = .0127$, $Re = 2.7 \times 10^6$, $\alpha = 20.50^\circ$.

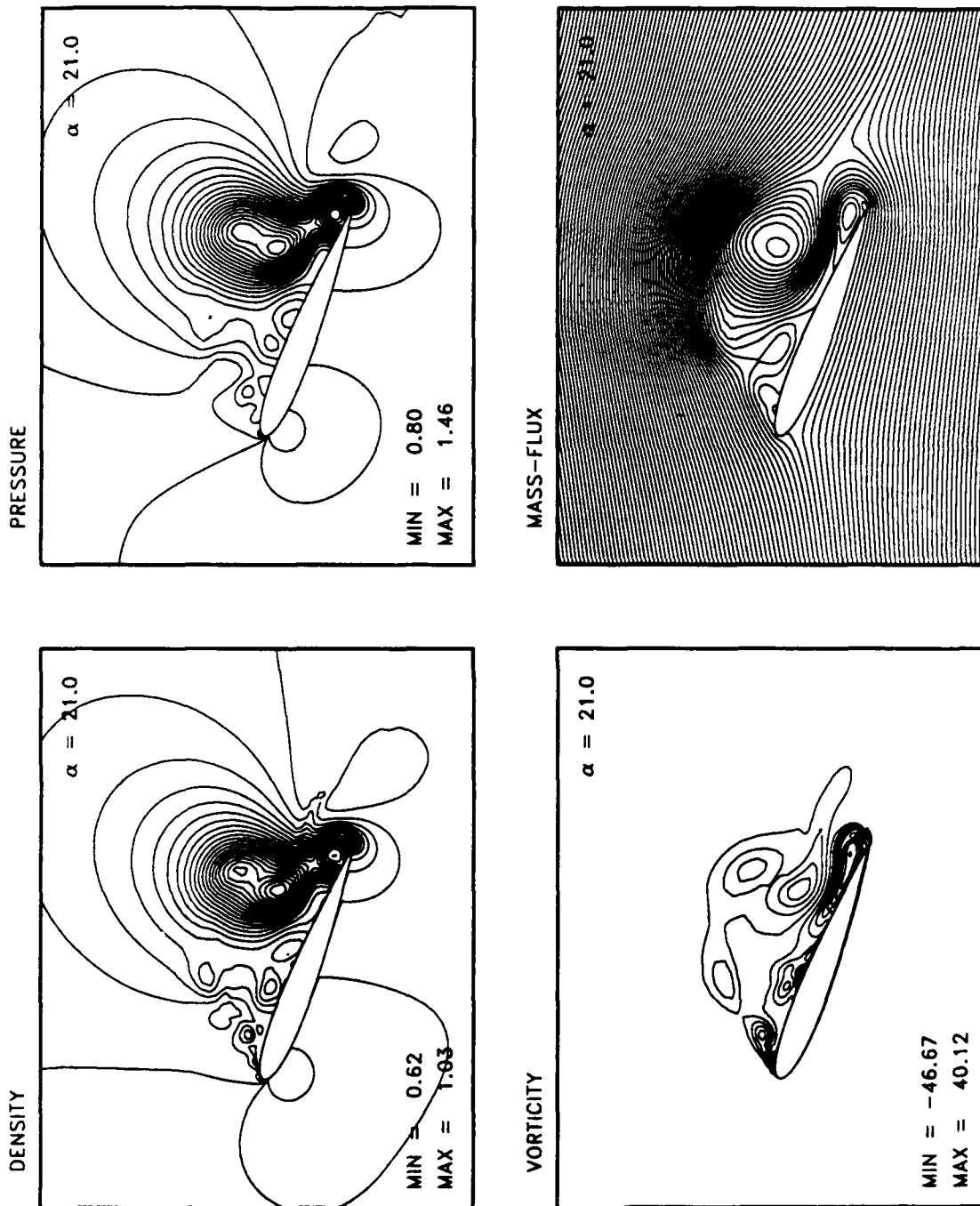


Figure 4.72: Ramp Motion Flow Details, $M_\infty = .3$, $k = .0127$, $Re = 2.7 \times 10^6$. $\alpha = 21.00^\circ$.

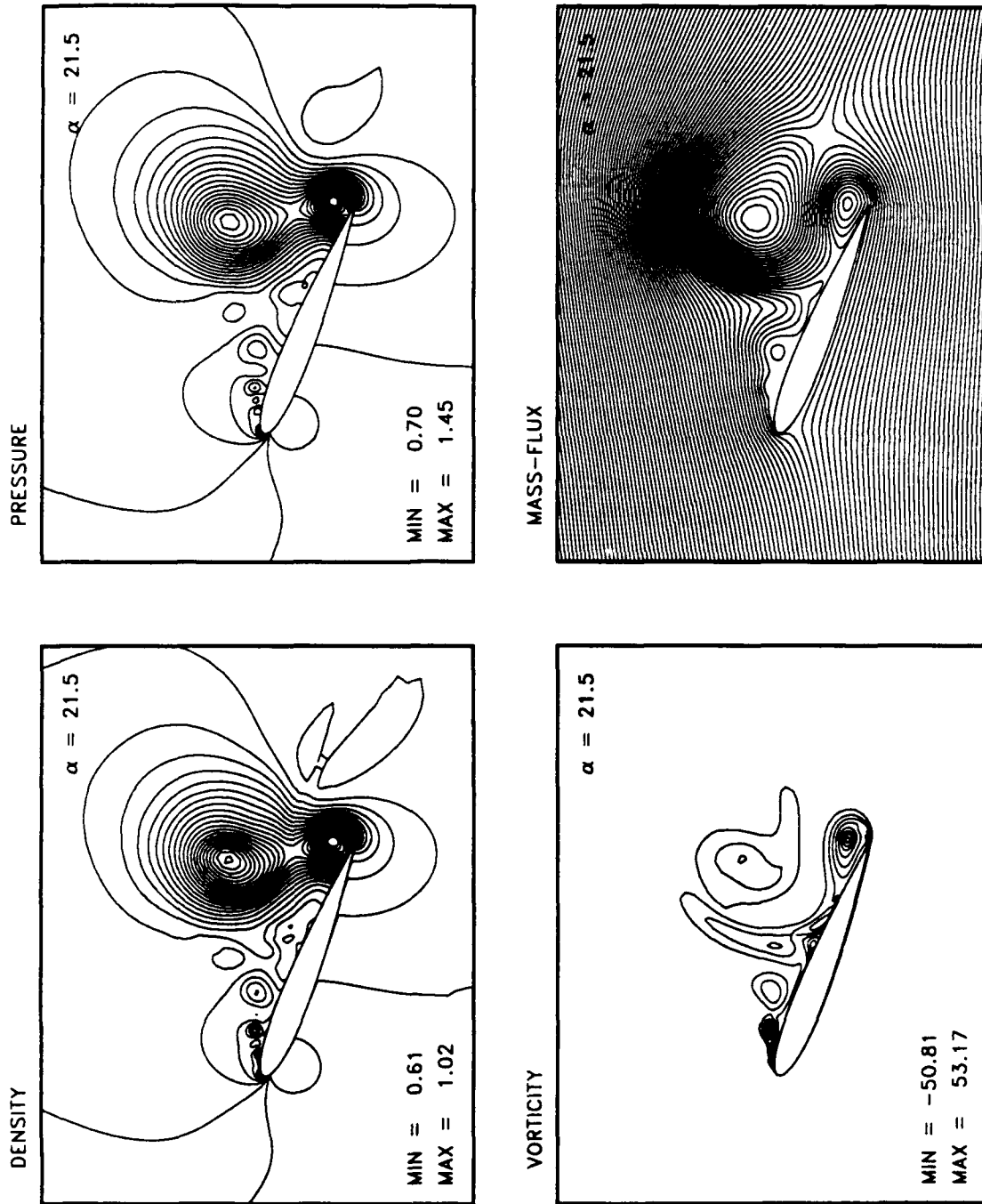


Figure 4.73: Ramp Motion Flow Details, $M_\infty = .3$, $k = .0127$, $Re = 2.7 \times 10^6$, $\alpha = 21.50^\circ$.

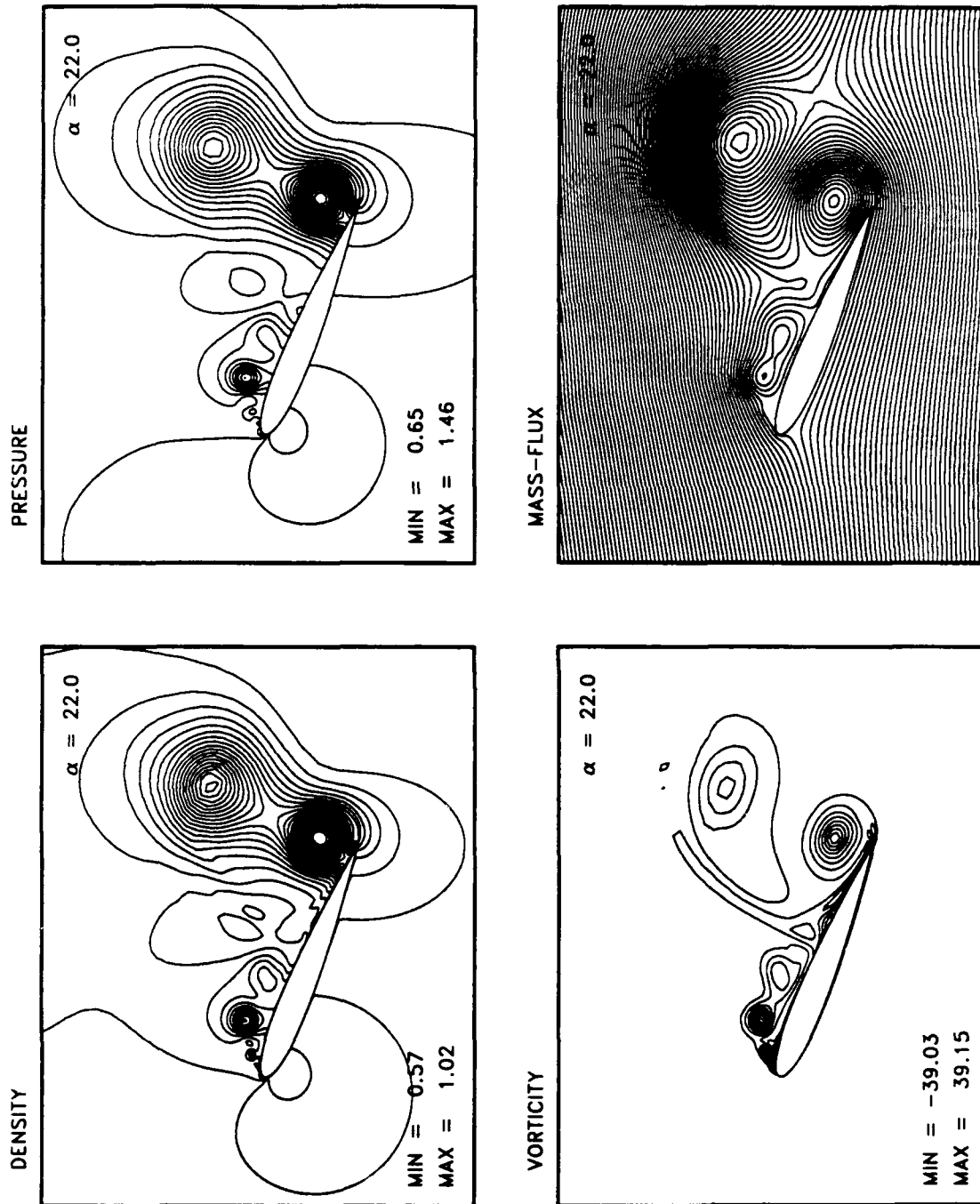


Figure 4.74: Ramp Motion Flow Details, $M_\infty = .3$, $k = .0127$, $Re = 2.7 \times 10^6$.
 $\alpha = 22.00^\circ$.

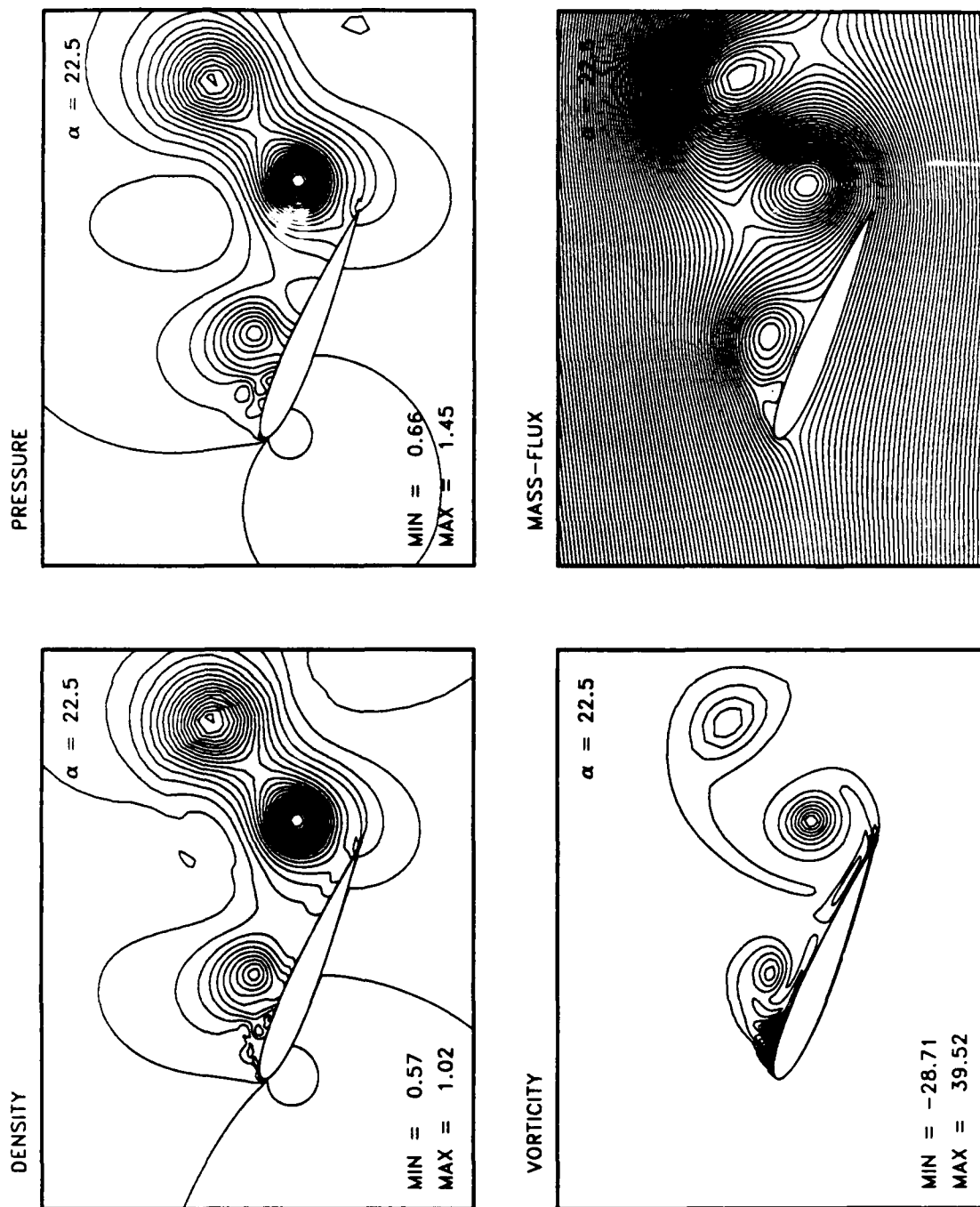


Figure 4.75: Ramp Motion Flow Details, $M_\infty = .3$, $k = .0127$, $Re = 2.7 \times 10^6$, $\alpha = 22.50^\circ$.

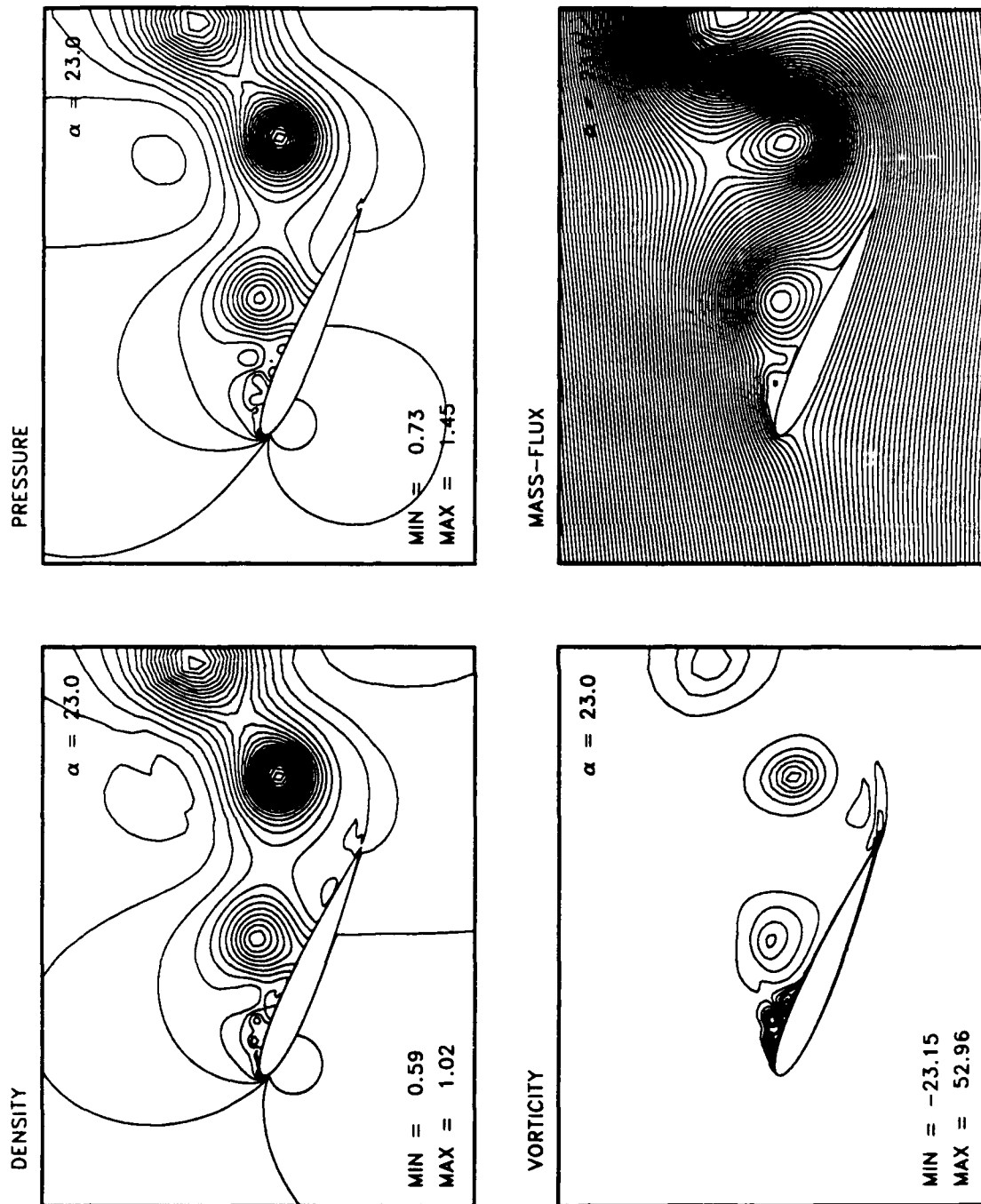


Figure 4.76: Ramp Motion Flow Details, $M_\infty = .3$, $k = .0127$, $Re = 2.7 \times 10^6$, $\alpha = 23.00^\circ$.

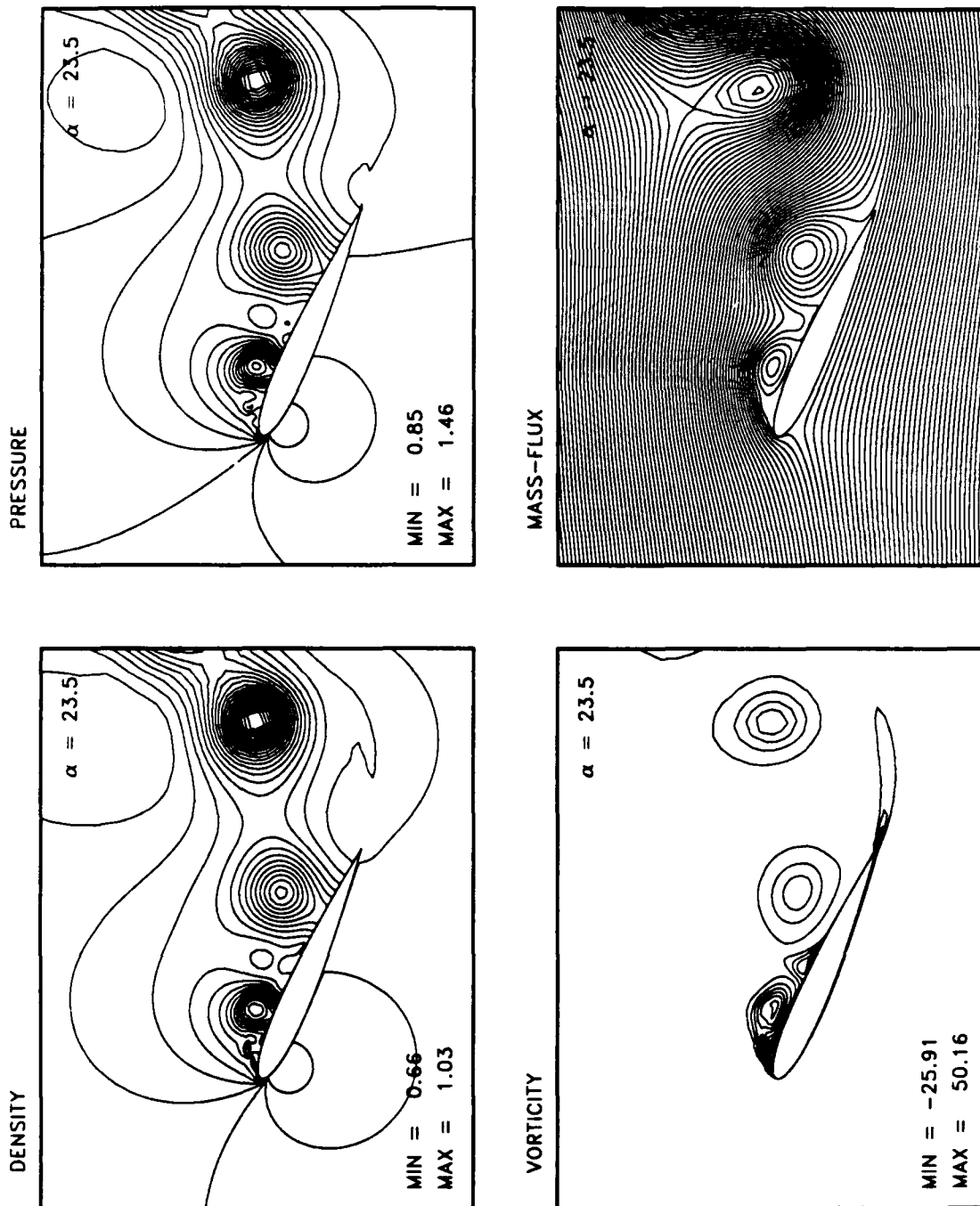


Figure 4.77: Ramp Motion Flow Details, $M_\infty = .3$, $k = .0127$, $Re = 2.7 \times 10^6$. $\alpha = 23.50^\circ$.

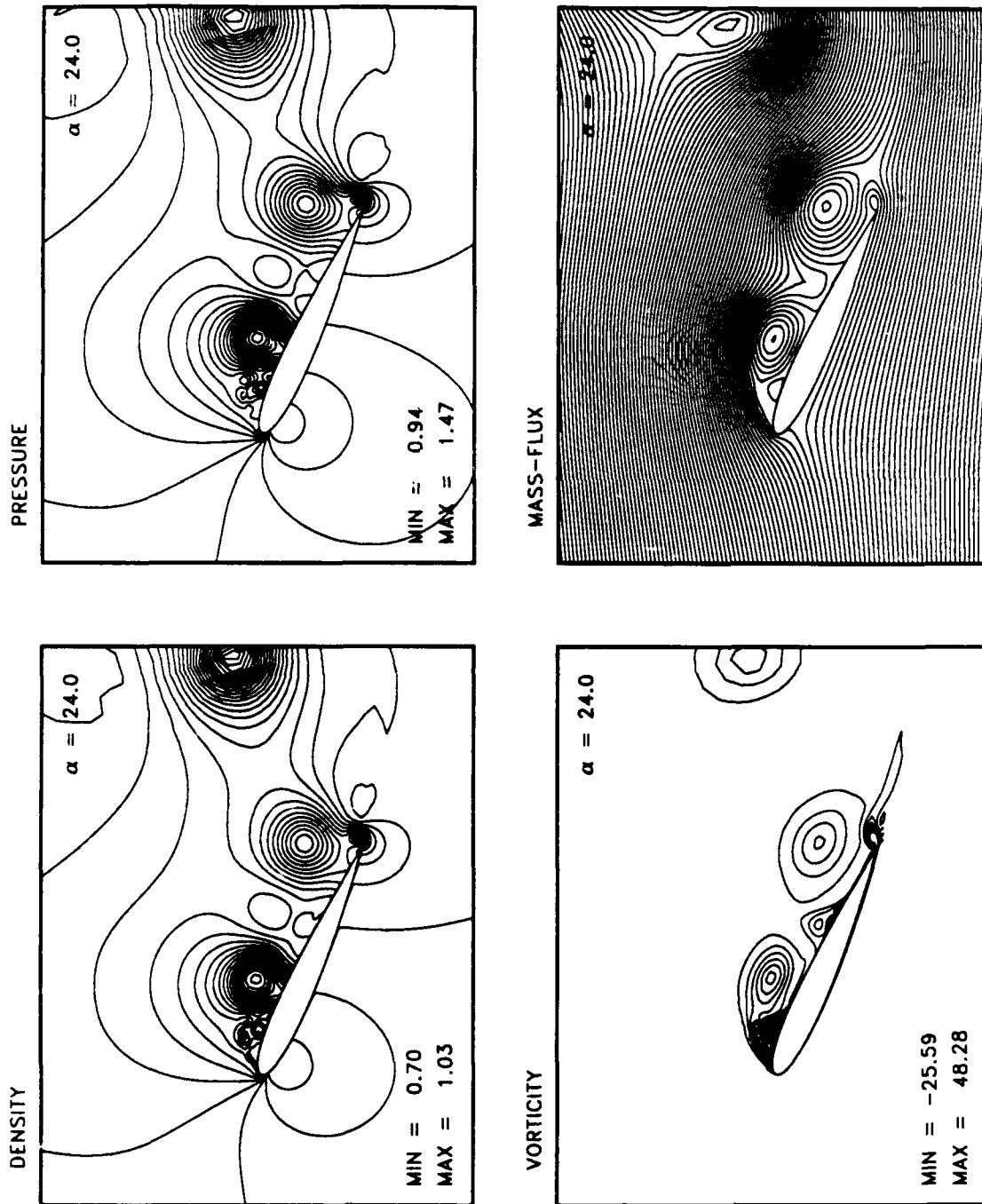


Figure 4.78: Ramp Motion Flow Details, $M_\infty = .3$, $k = .0127$, $Re = 2.7 \times 10^6$. $\alpha = 24.00^\circ$.

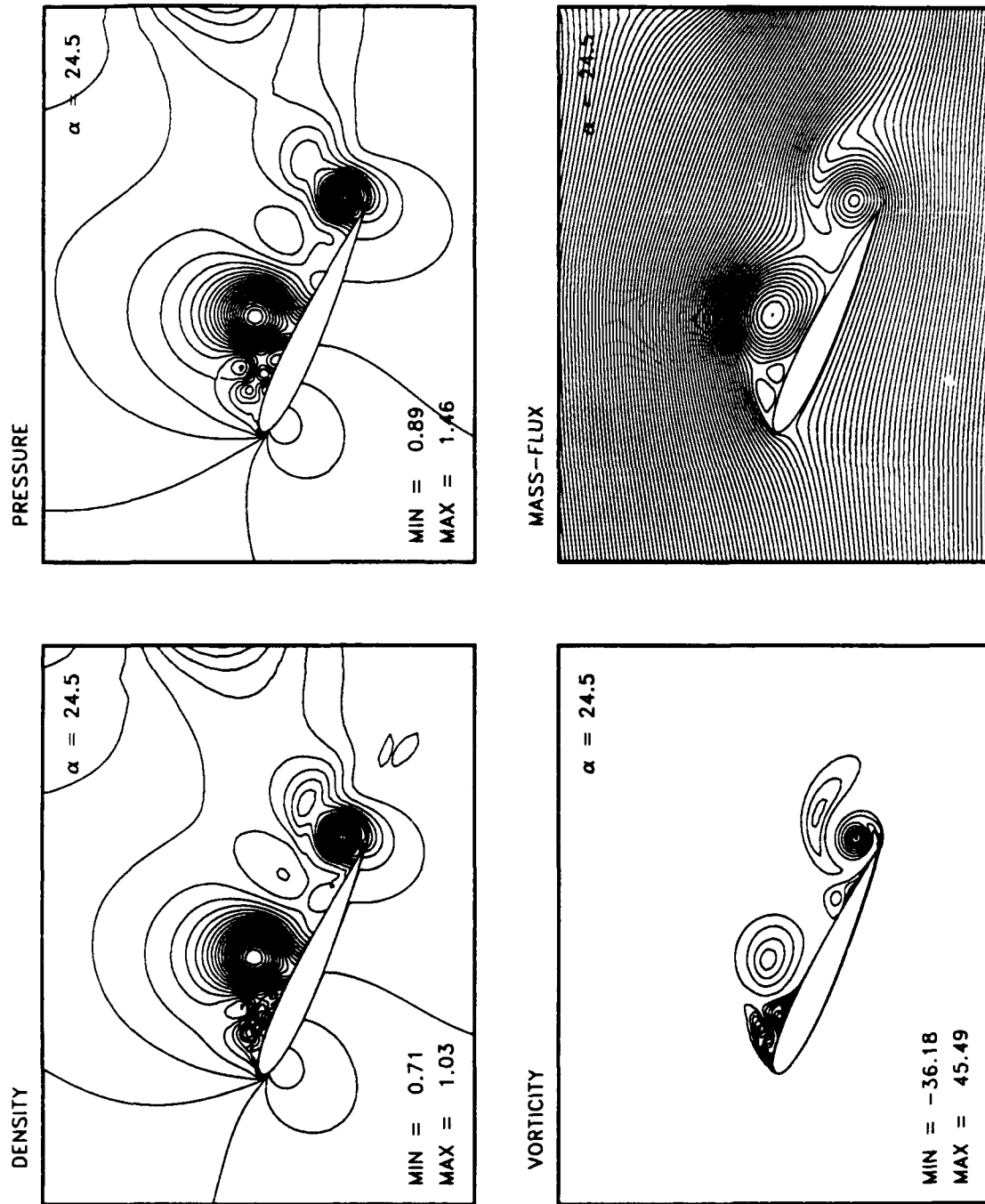


Figure 4.79: Ramp Motion Flow Details, $M_\infty = .3$, $k = .0127$, $Re = 2.7 \times 10^6$, $\alpha = 24.50^\circ$.

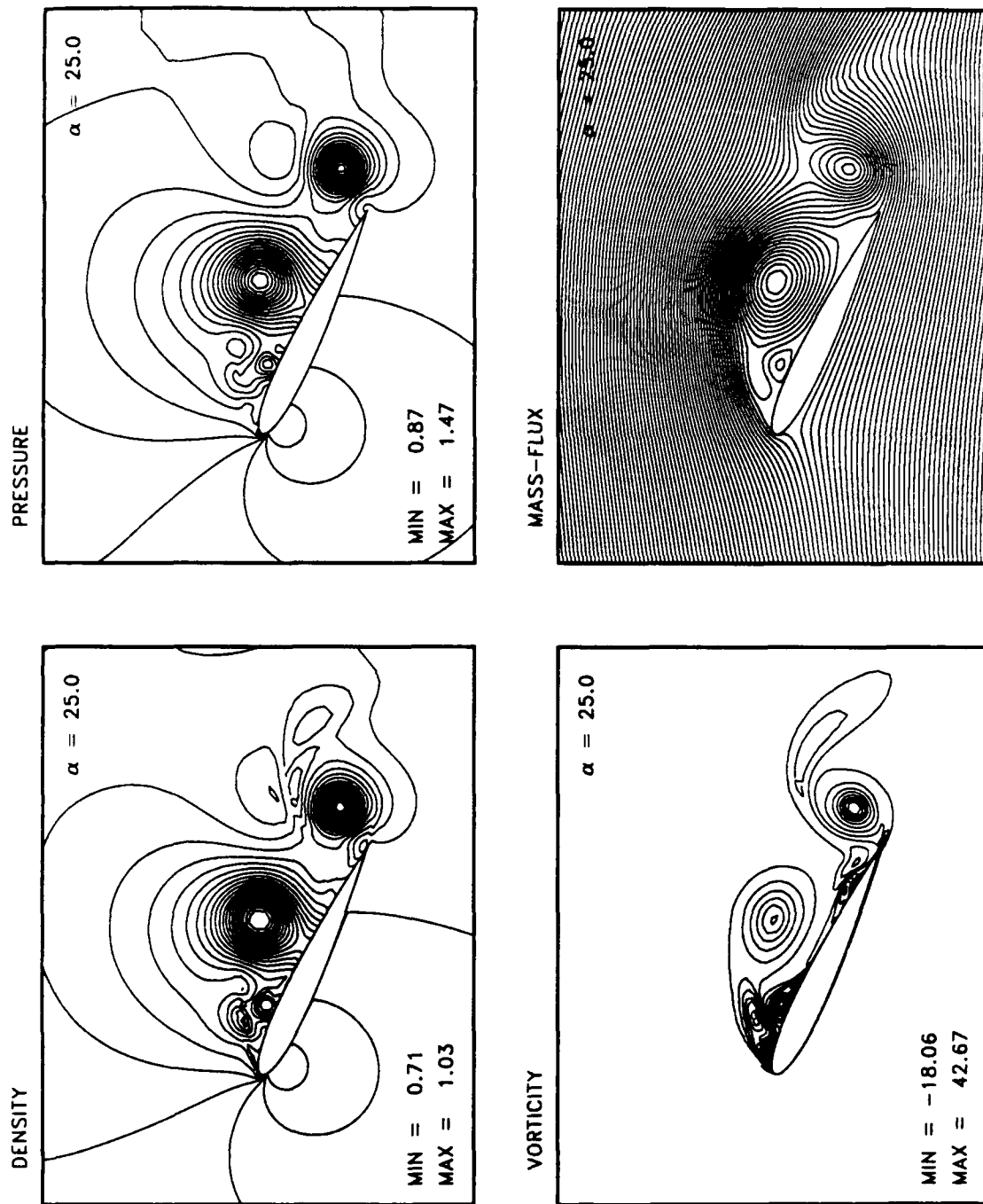


Figure 4.80: Ramp Motion Flow Details, $M_\infty = .3$, $k = .0127$, $Re = 2.7 \times 10^6$, $\alpha = 25.00^\circ$.

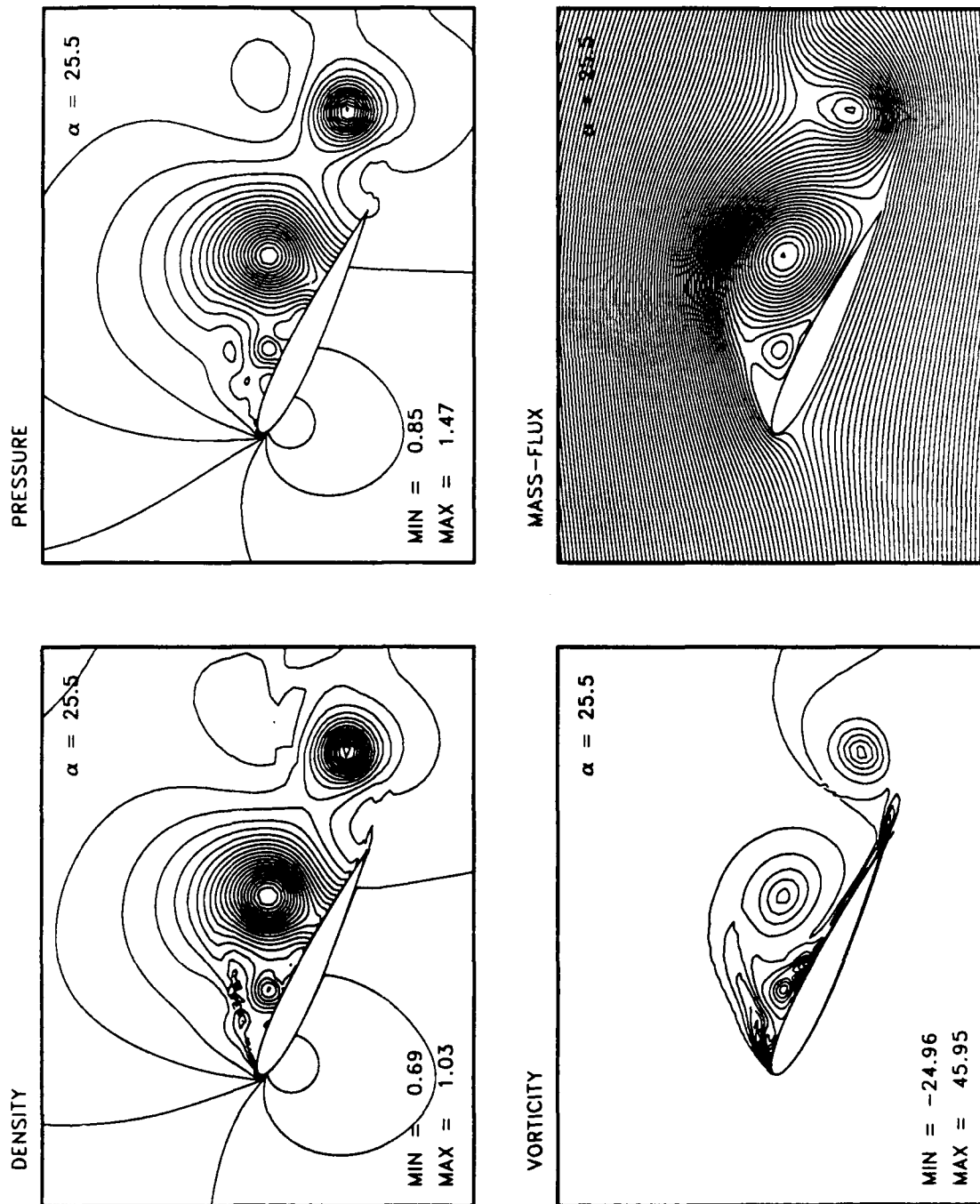


Figure 4.81: Ramp Motion Flow Details, $M_\infty = .3$, $k = .0127$, $Re = 2.7 \times 10^6$, $\alpha = 25.50^\circ$.

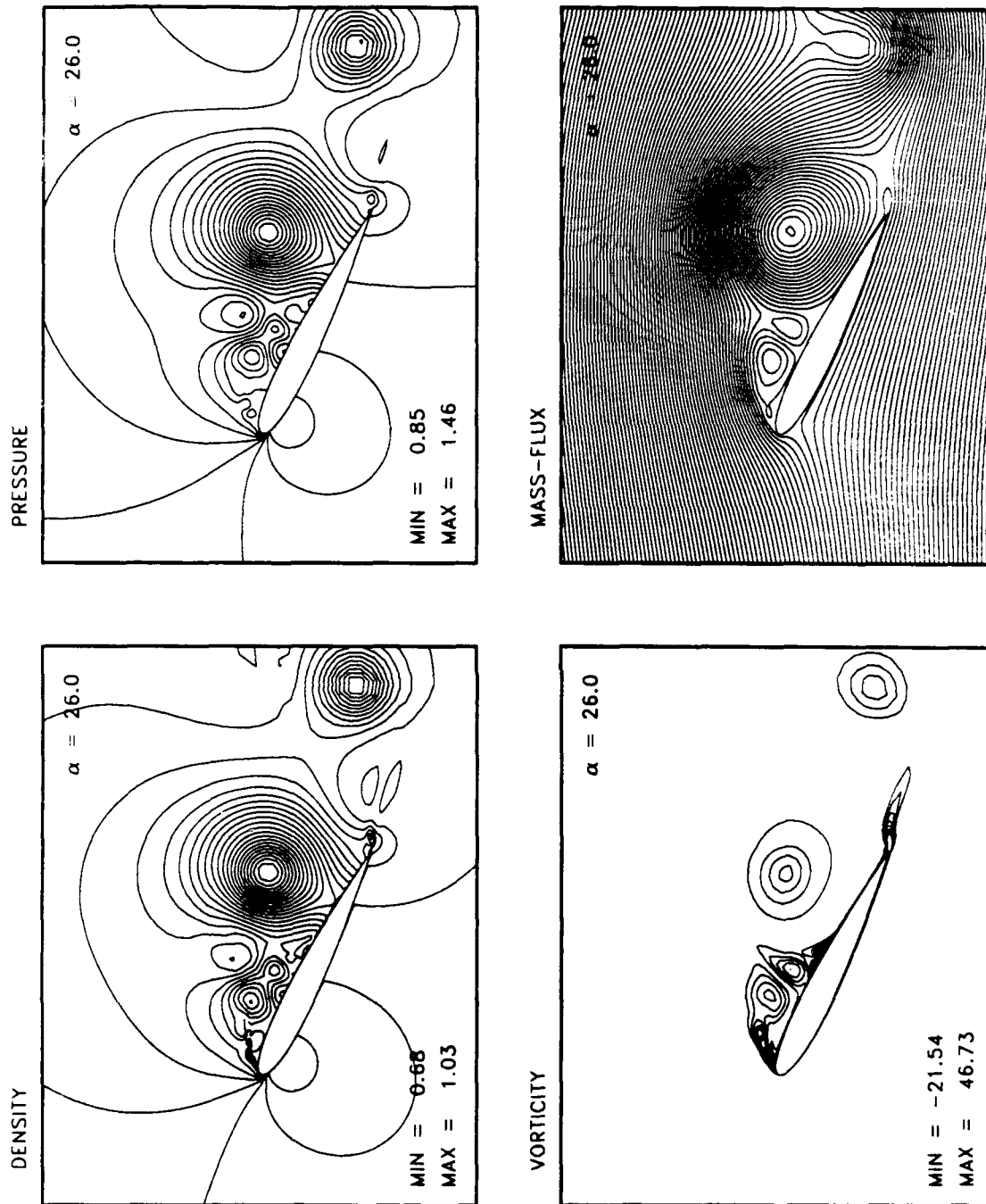


Figure 4.82: Ramp Motion Flow Details, $M_\infty = .3$, $k = .0127$, $Re = 2.7 \times 10^6$, $\alpha = 26.00^\circ$.

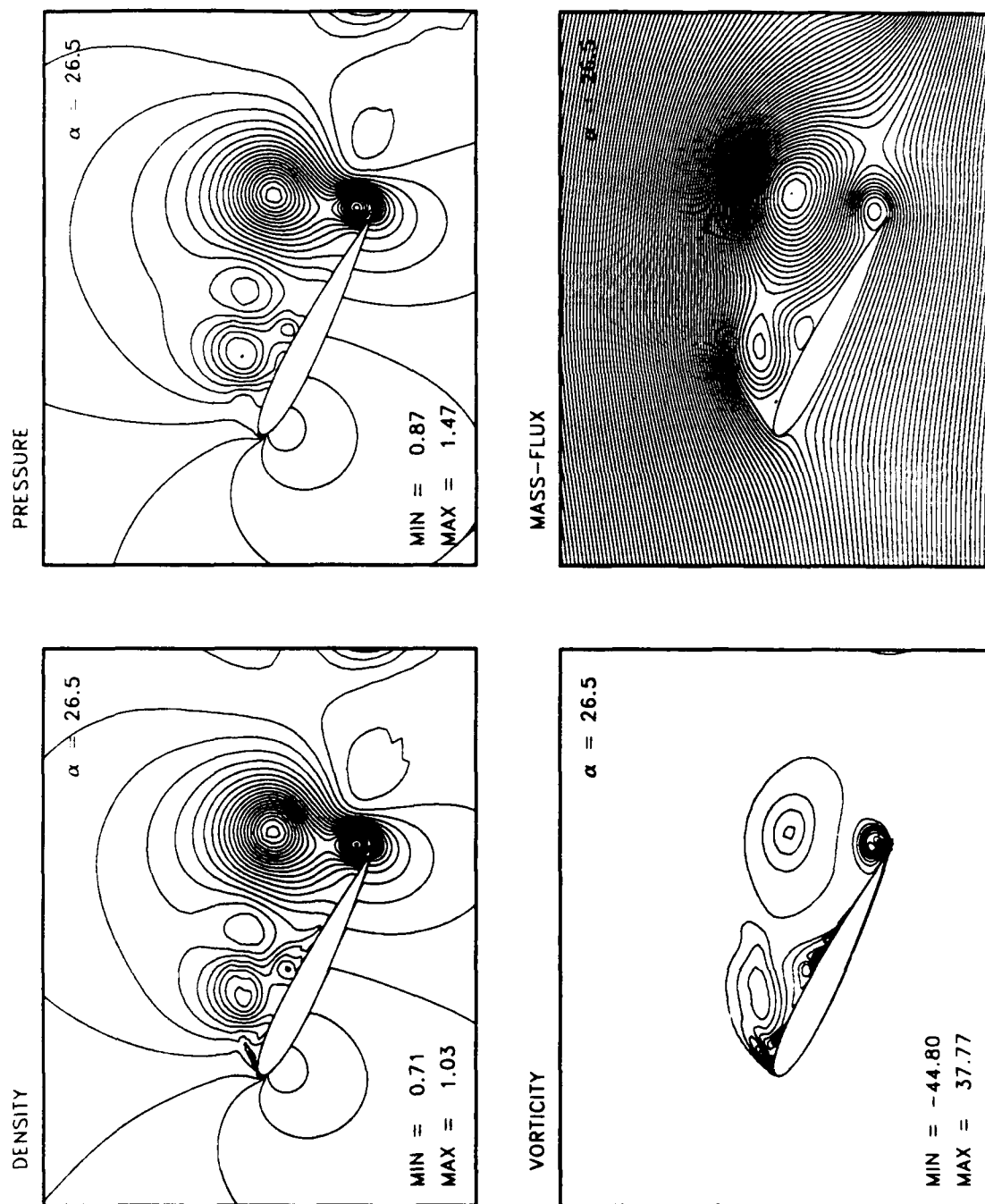


Figure 4.83: Ramp Motion Flow Details. $M_\infty = .3$, $k = .0127$, $Re = 2.7 \times 10^6$, $\alpha = 26.50^\circ$.

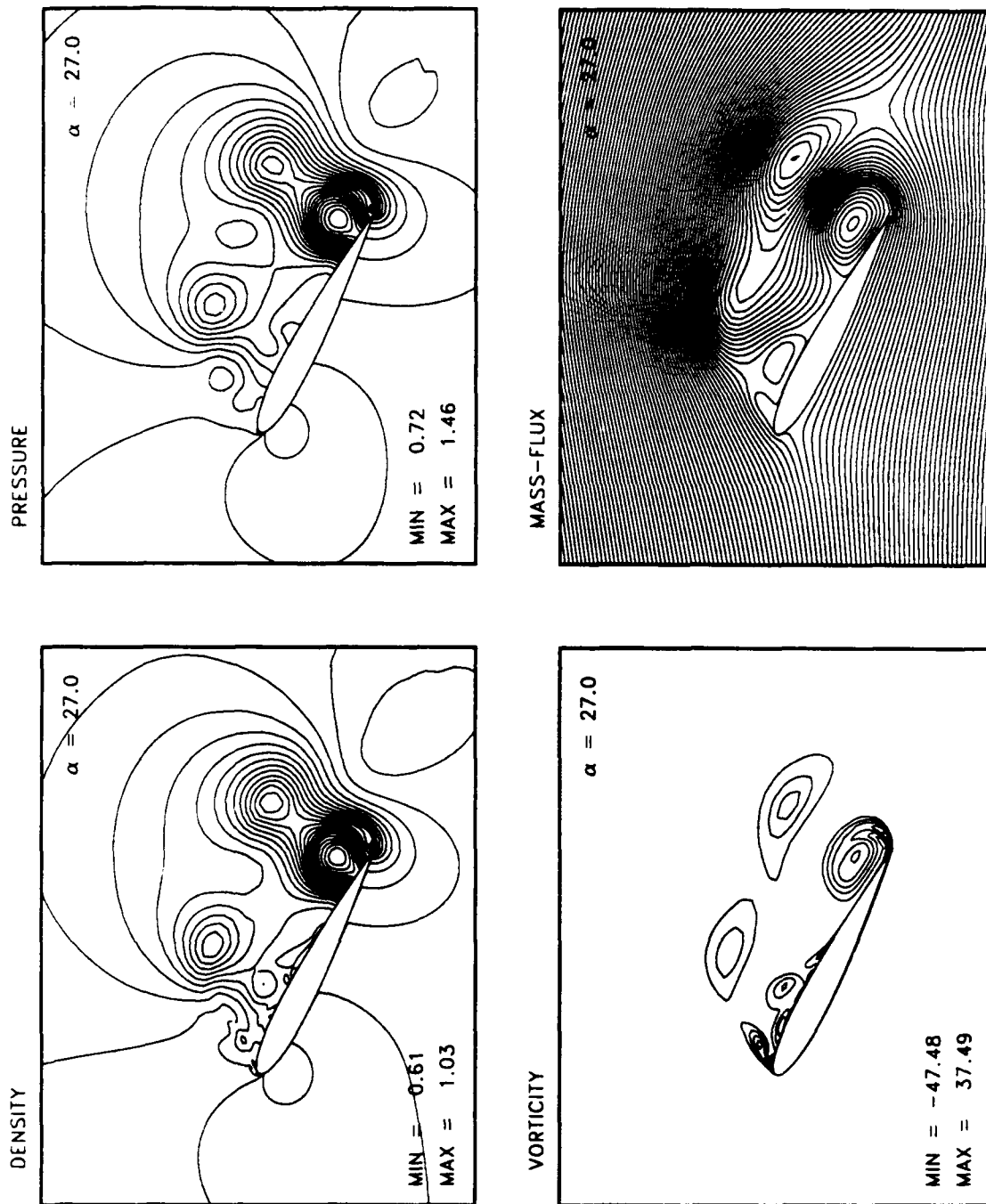


Figure 4.84: Ramp Motion Flow Details, $M_\infty = .3$, $k = .0127$, $Re = 2.7 \times 10^6$, $\alpha = 27.00^\circ$.

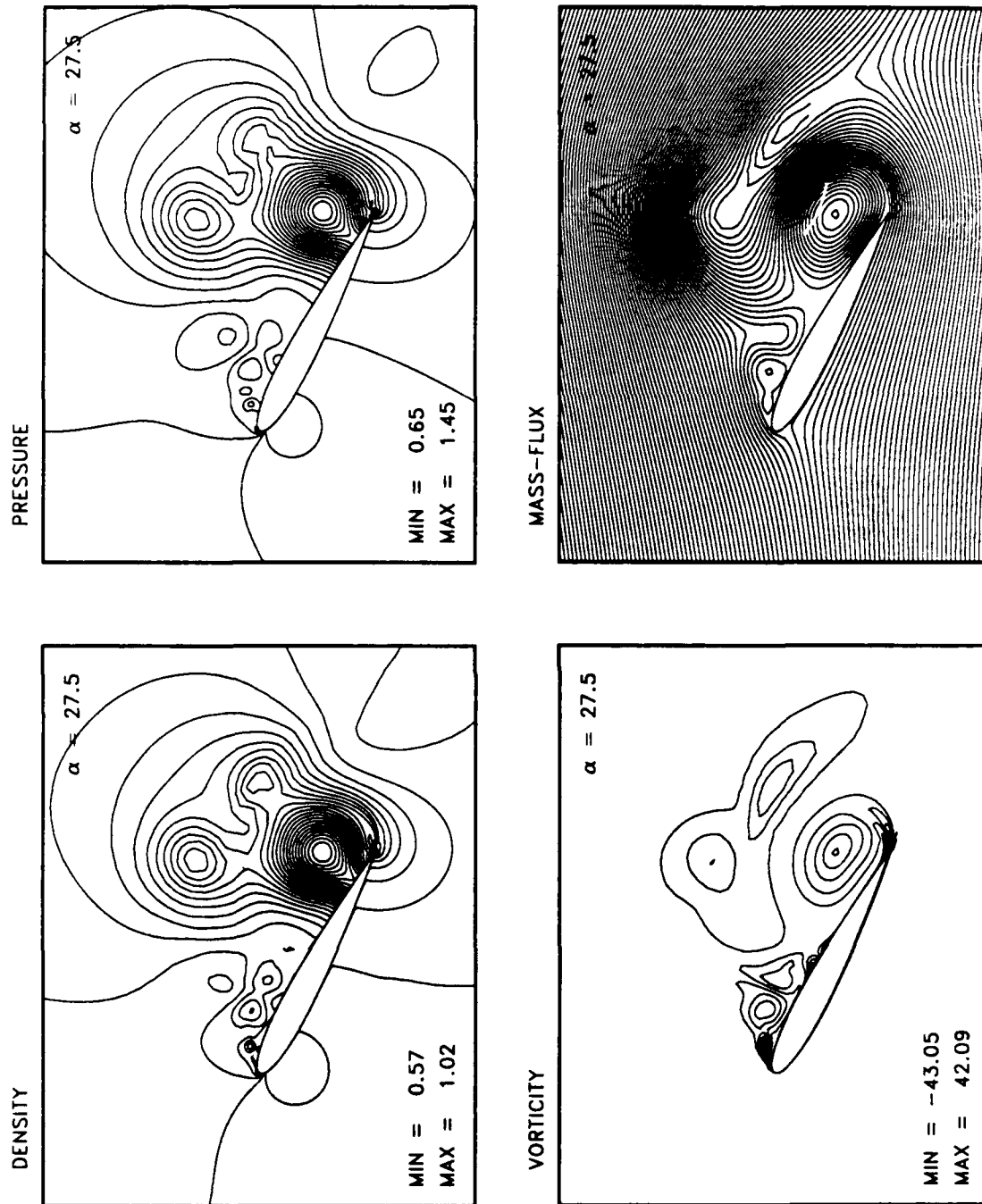


Figure 4.85: Ramp Motion Flow Details, $M_\infty = .3$, $k = .0127$, $Re = 2.7 \times 10^6$, $\alpha = 27.50^\circ$.

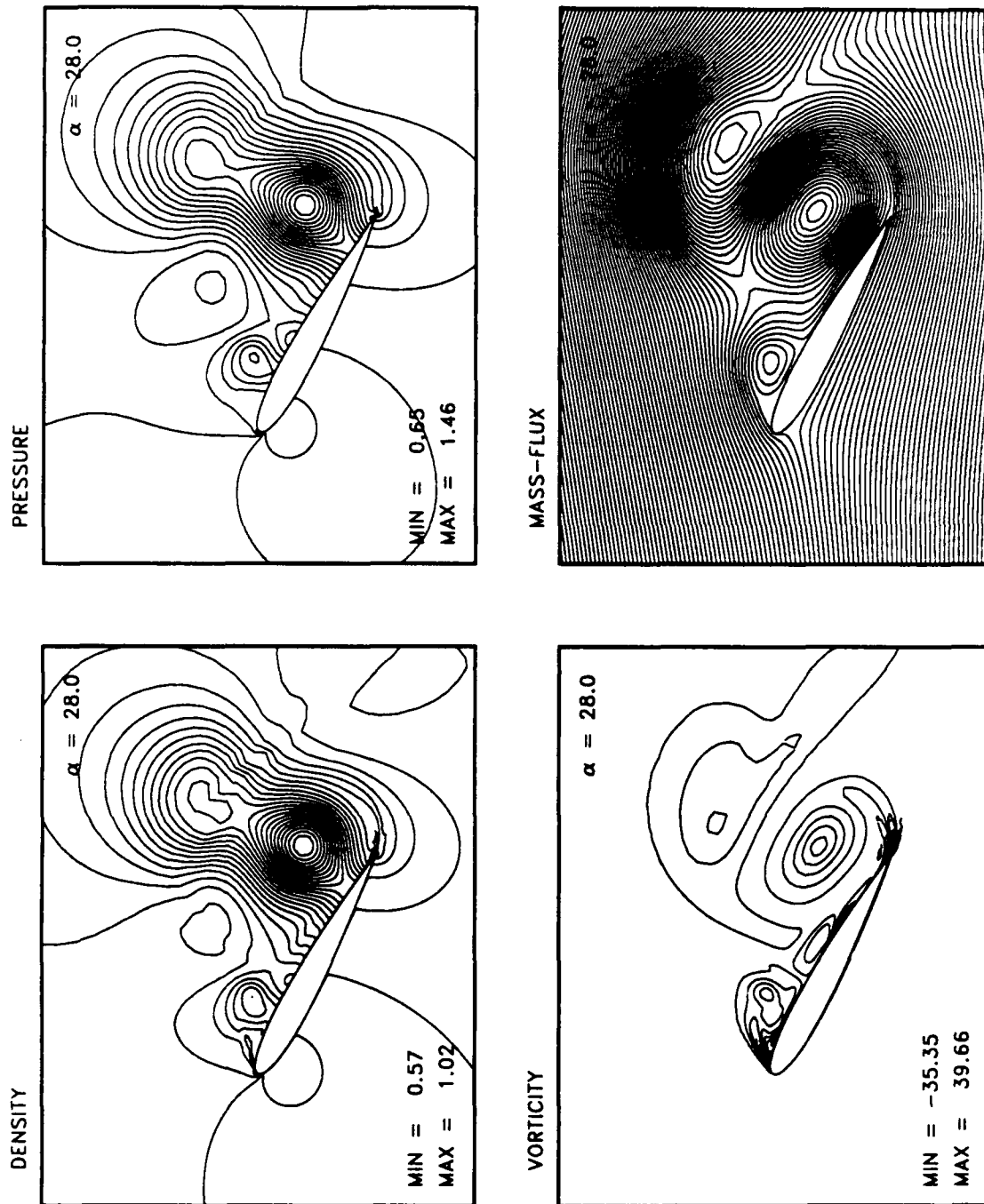


Figure 4.86: Ramp Motion Flow Details, $M_\infty = .3$, $k = .0127$, $Re = 2.7 \times 10^6$, $\alpha = 28.00^\circ$.

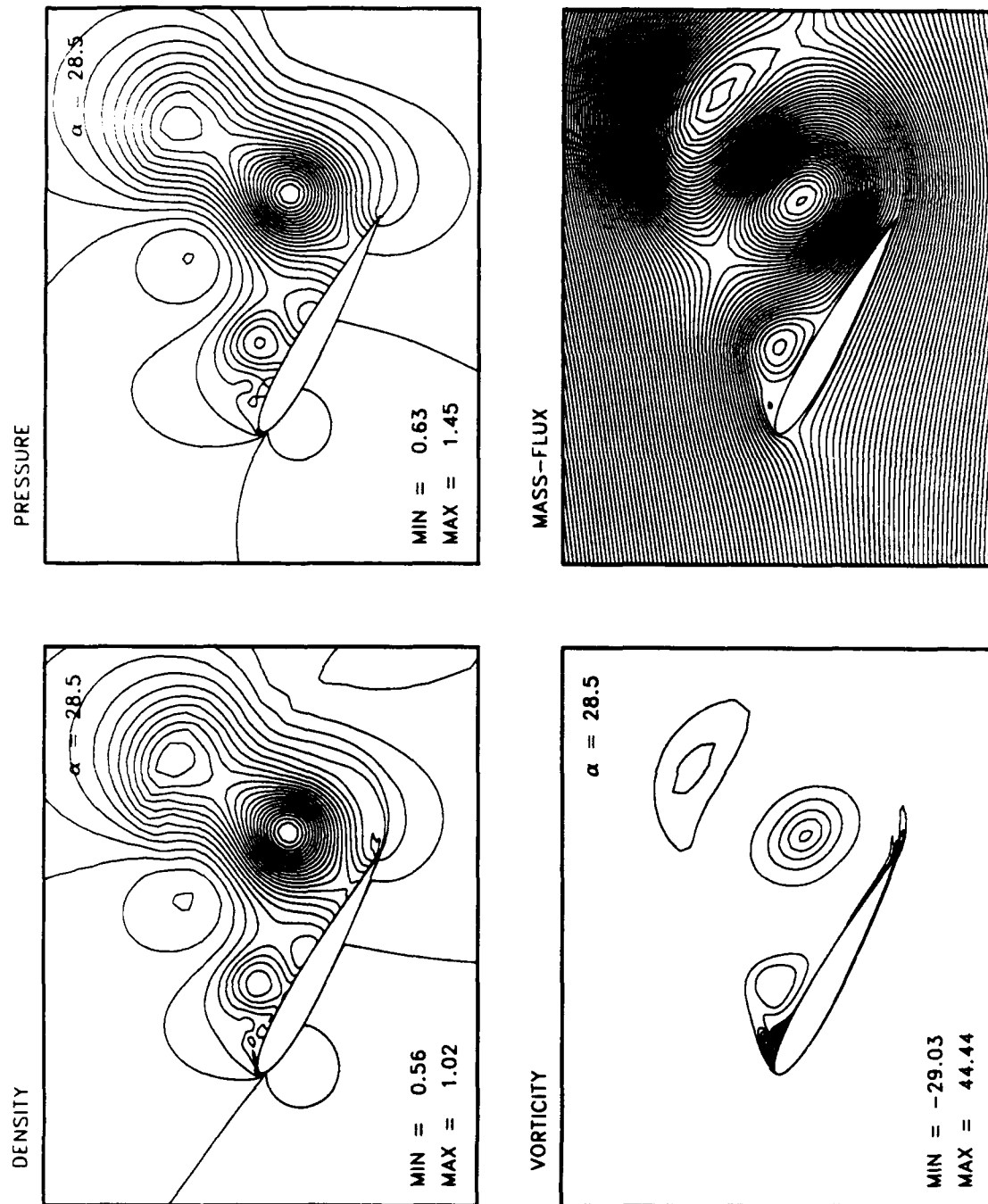


Figure 4.87: Ramp Motion Flow Details. $M_\infty = .3$, $k = .0127$, $Re = 2.7 \times 10^6$, $\alpha = 28.50^\circ$.

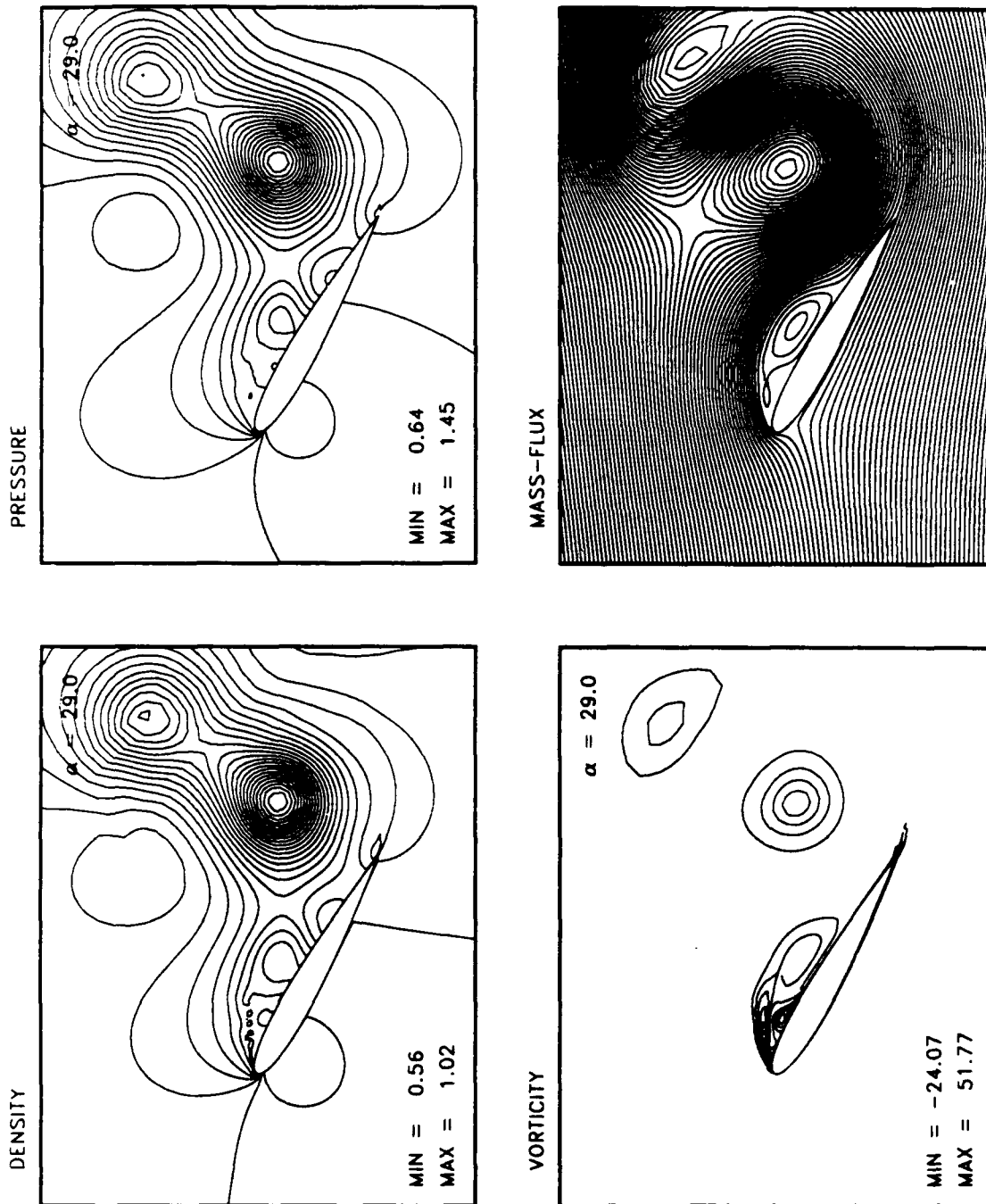


Figure 4.88: Ramp Motion Flow Details. $M_\infty = .3$, $k = .0127$, $Re = 2.7 \times 10^6$, $\alpha = 29.00^\circ$.

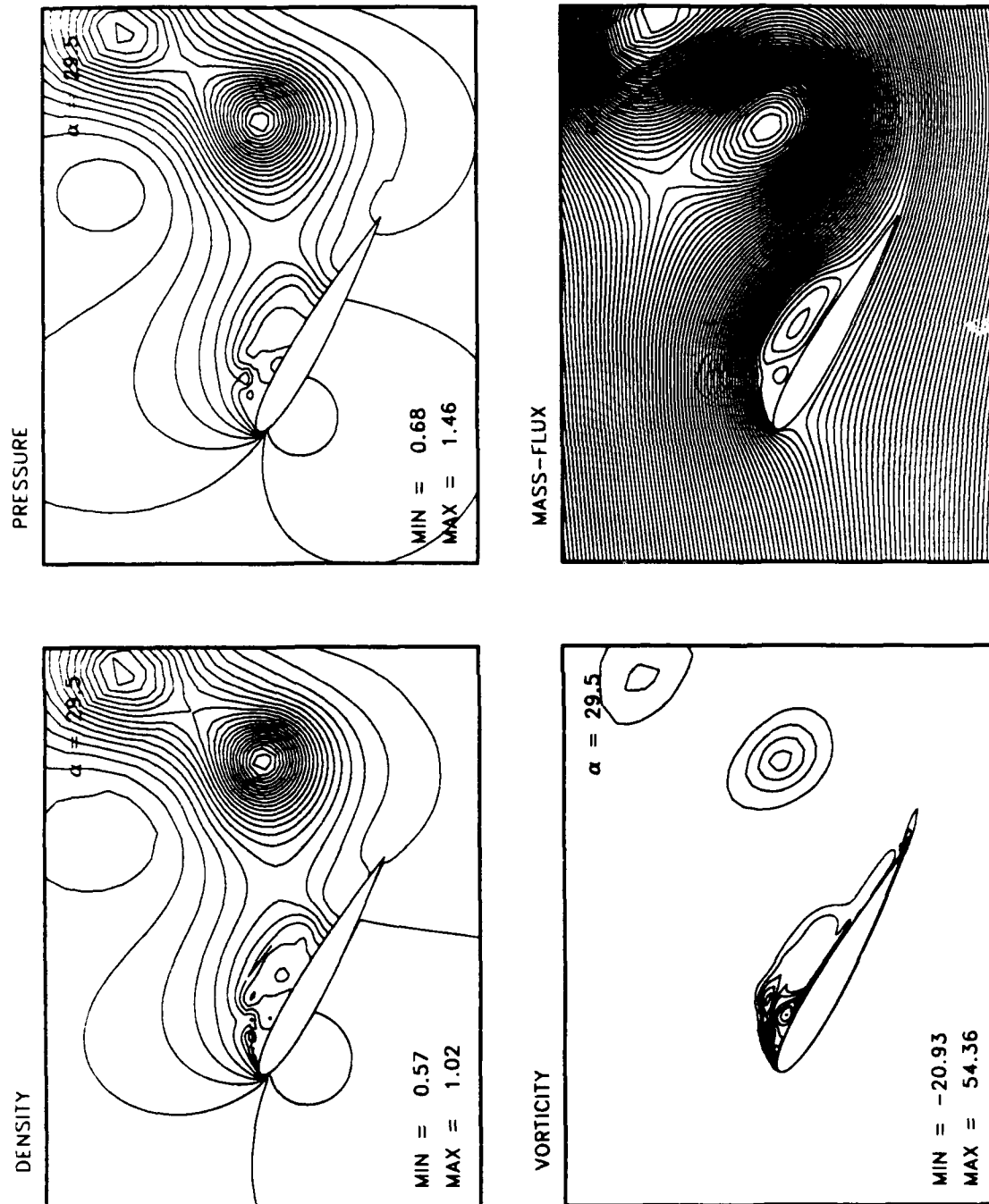


Figure 4.89: Ramp Motion Flow Details, $M_\infty = .3$, $k = .0127$, $Re = 2.7 \times 10^6$, $\alpha = 29.50^\circ$.

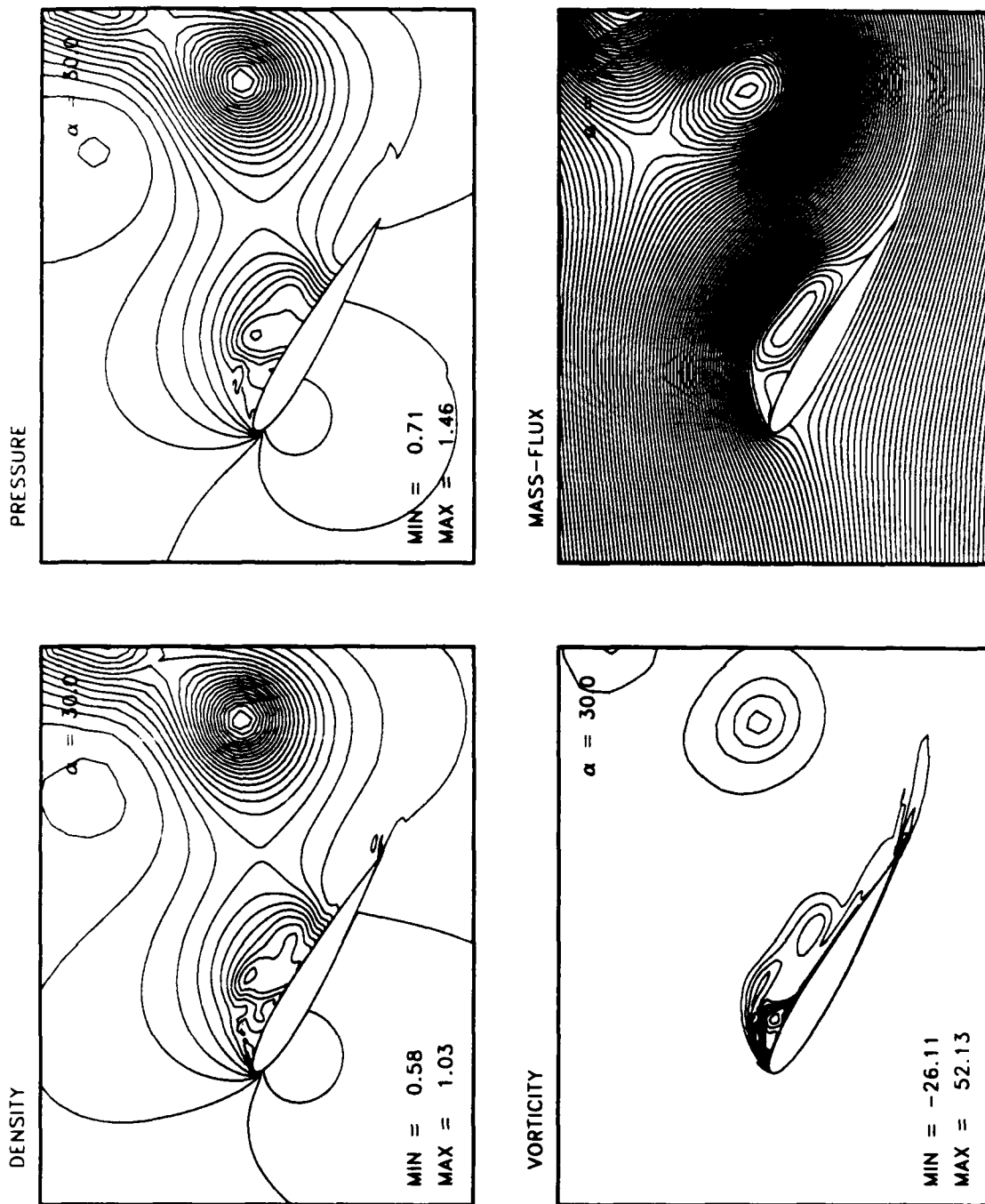


Figure 4.90: Ramp Motion Flow Details. $M_\infty = .3$, $k = .0127$, $Re = 2.7 \times 10^6$, $\alpha = 30.00^\circ$.

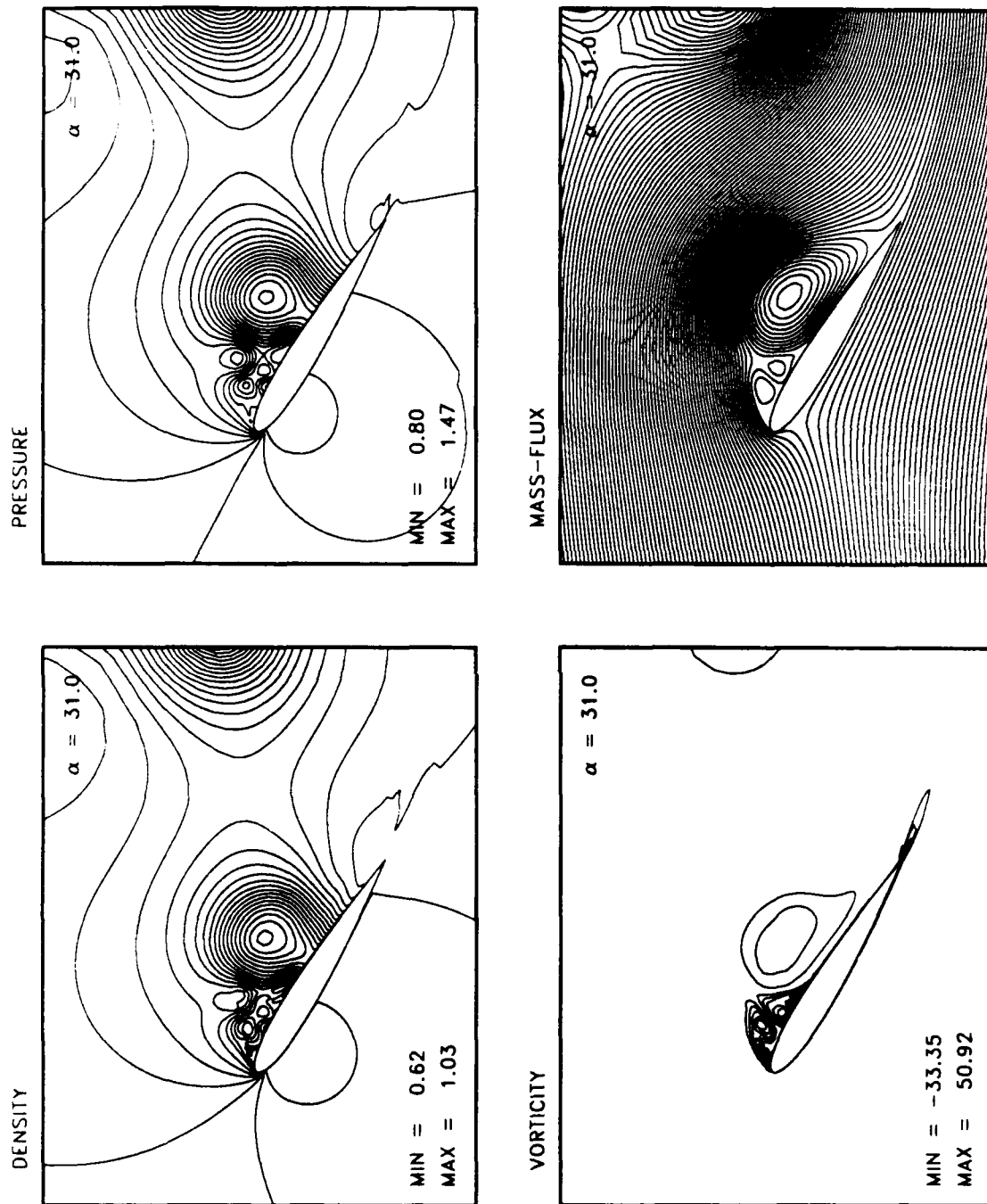


Figure 4.91: Ramp Motion Flow Details, $M_\infty = .3$, $k = .0127$, $Re = 2.7 \times 10^6$, $\alpha = 31.00^\circ$.

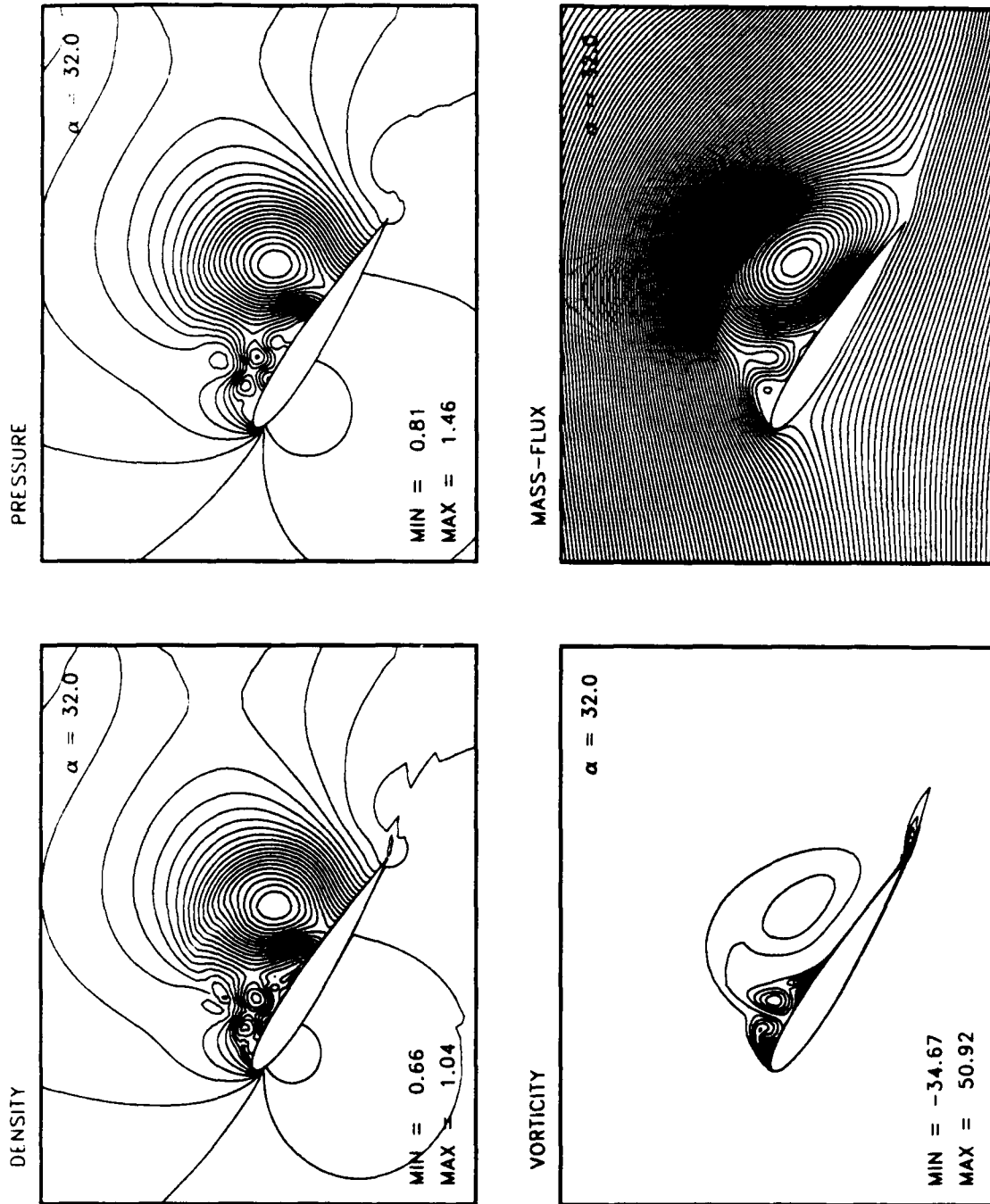


Figure 4.92: Ramp Motion Flow Details, $M_\infty = .3$, $k = .0127$, $Re = 2.7 \times 10^6$, $\alpha = 32.00^\circ$.

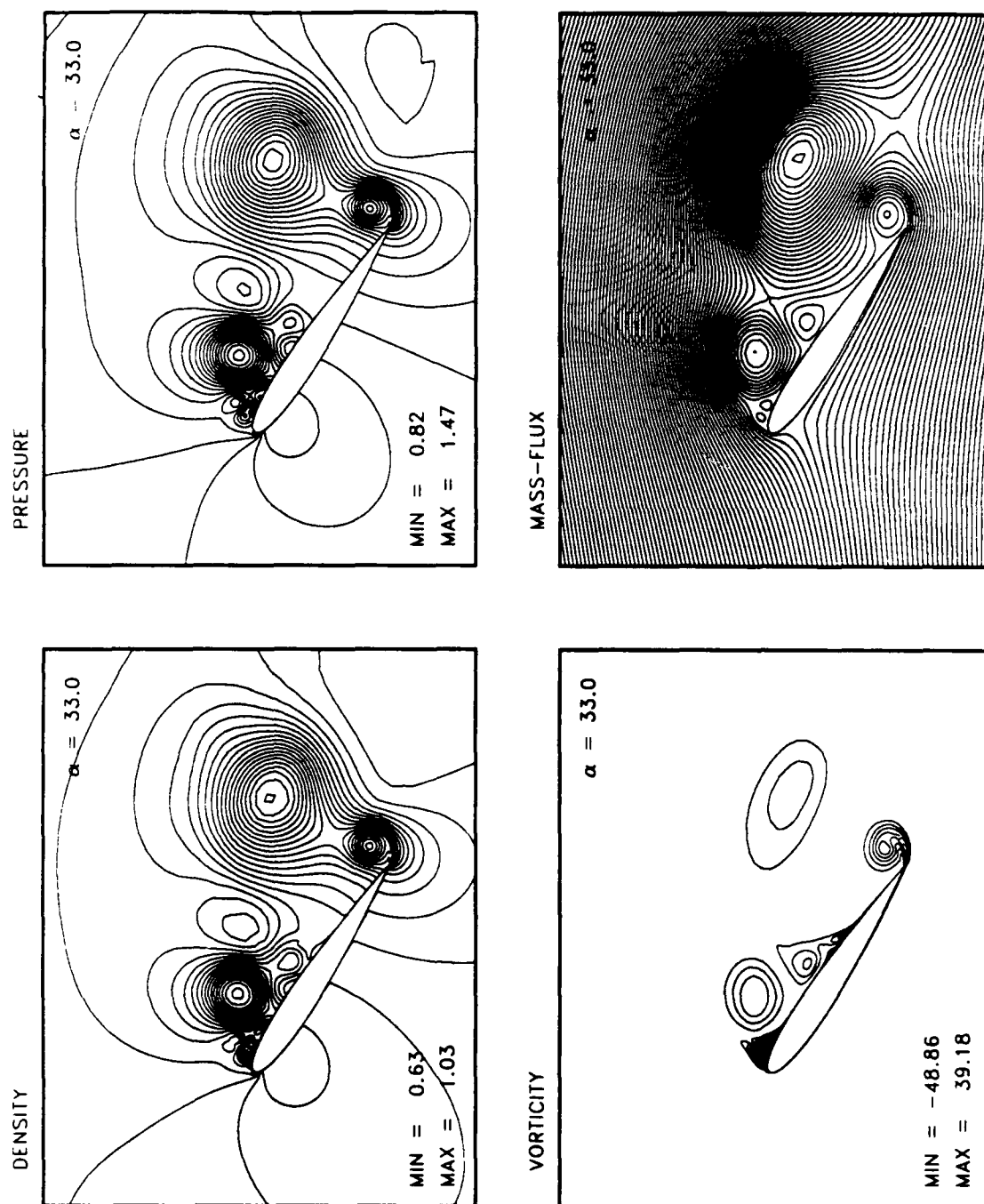


Figure 4.93: Ramp Motion Flow Details. $M_\infty = .3$, $k = .0127$, $Re = 2.7 \times 10^6$, $\alpha = 33.00^\circ$.

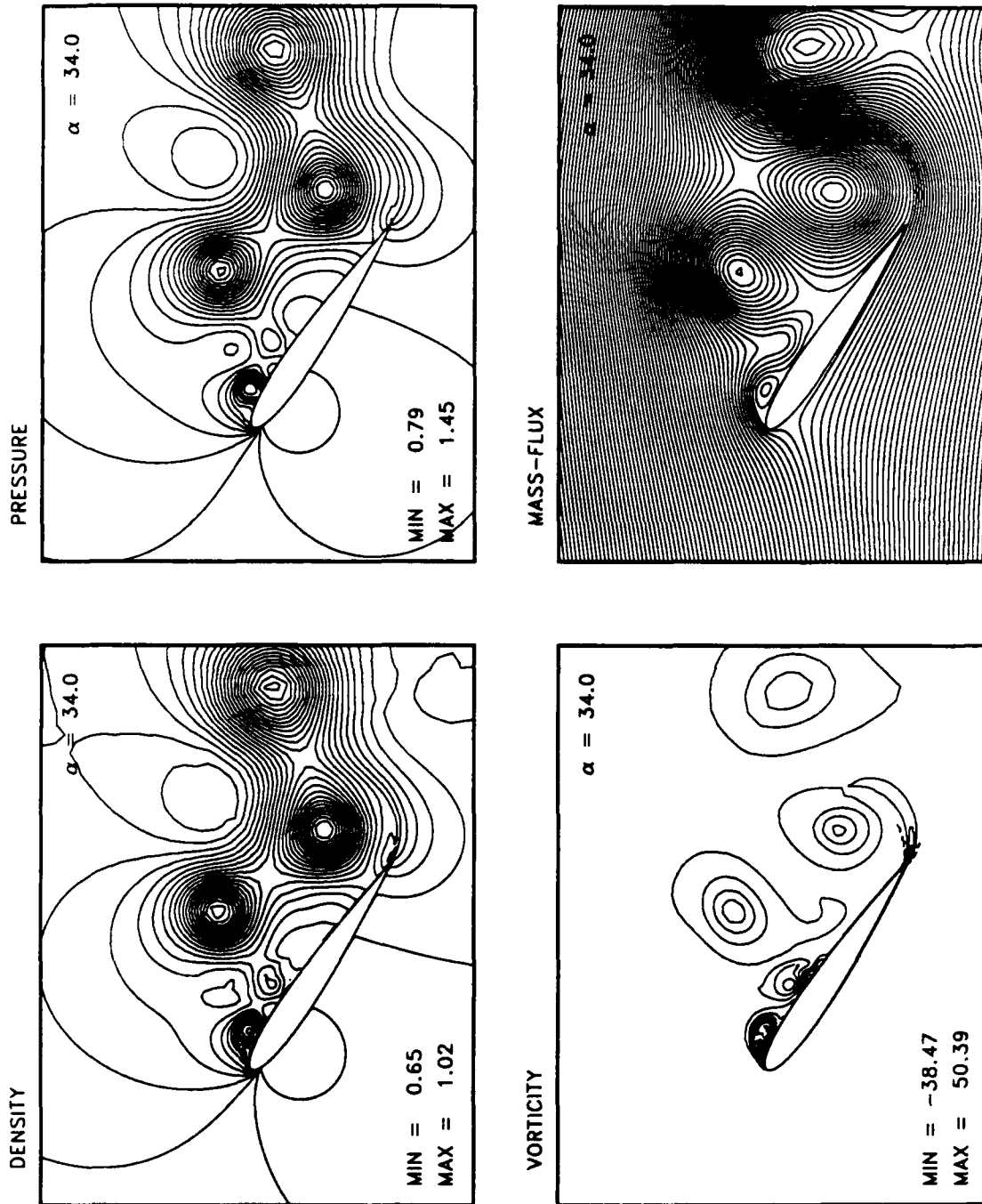


Figure 4.94: Ramp Motion Flow Details, $M_\infty = .3$, $k = .0127$, $Re = 2.7 \times 10^6$, $\alpha = 34.00^\circ$.

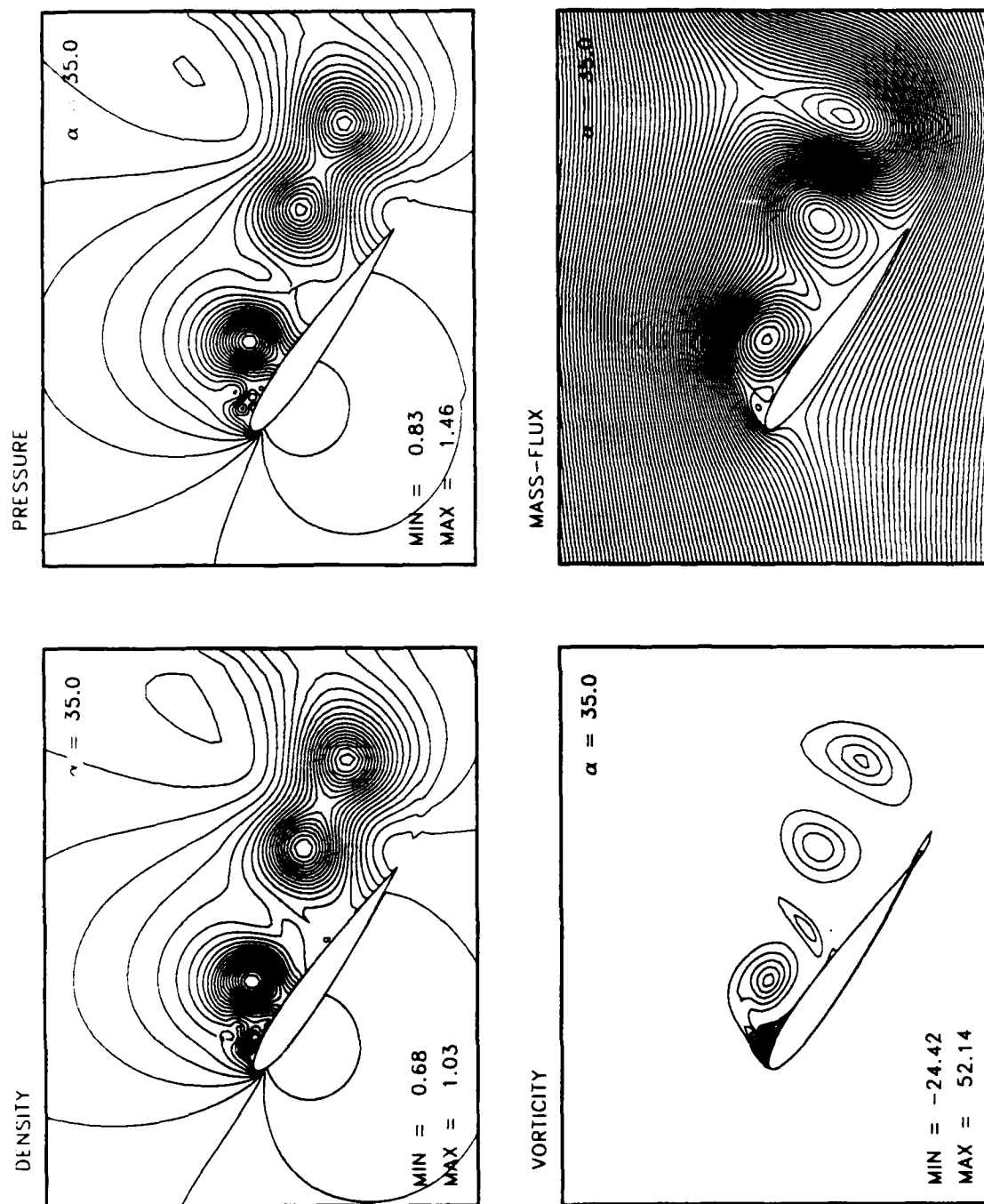


Figure 4.95: Ramp Motion Flow Details. $M_\infty = .3$, $k = .0127$, $Re = 2.7 \times 10^6$. $\alpha = 35.00^\circ$.

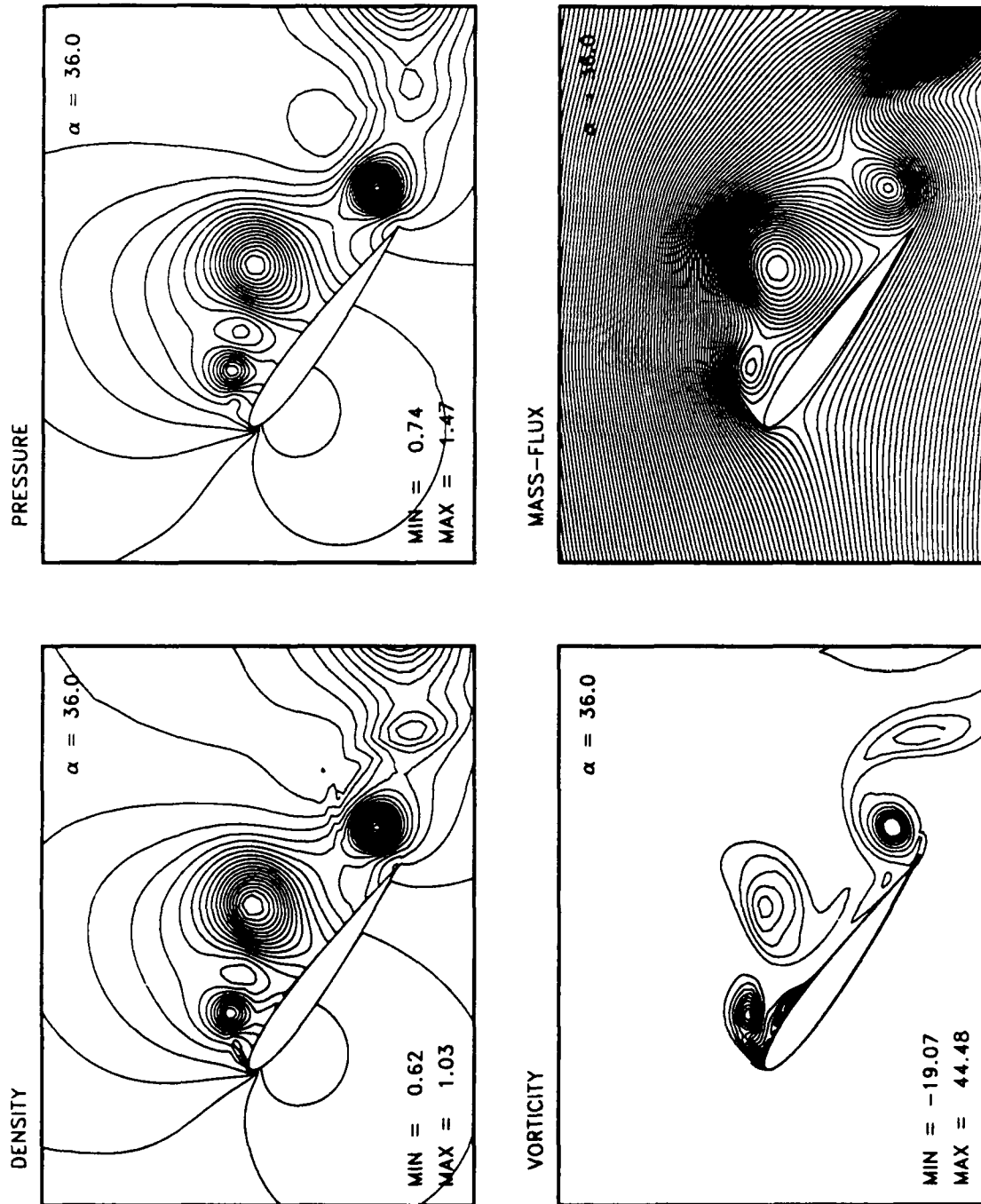


Figure 4.96: Ramp Motion Flow Details, $M_\infty = .3$, $k = .0127$, $Re = 2.7 \times 10^6$, $\alpha = 36.00^\circ$.

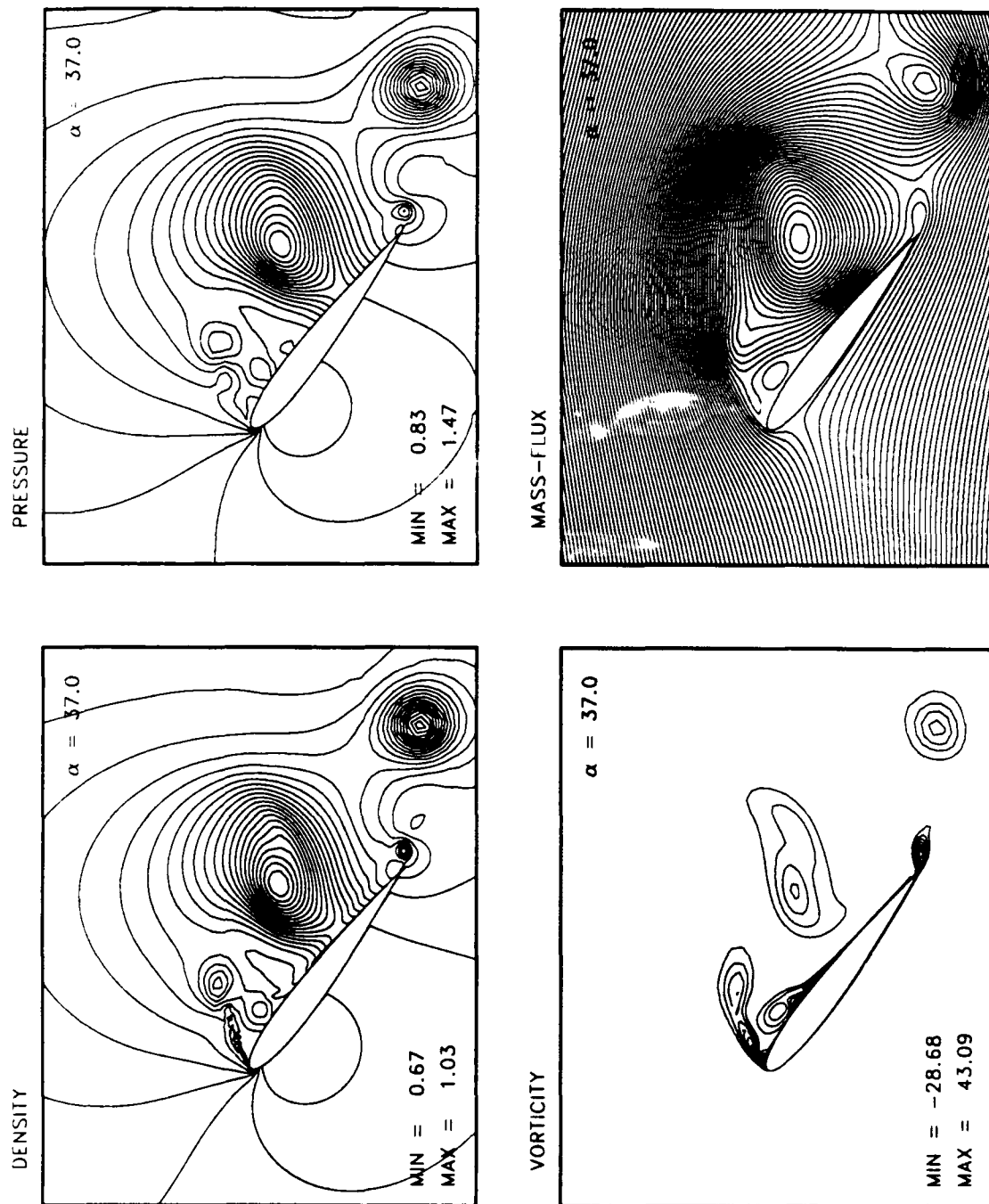


Figure 4.97: Ramp Motion Flow Details. $M_\infty = .3$, $k = .0127$, $Re = 2.7 \times 10^6$, $\alpha = 37.00^\circ$.

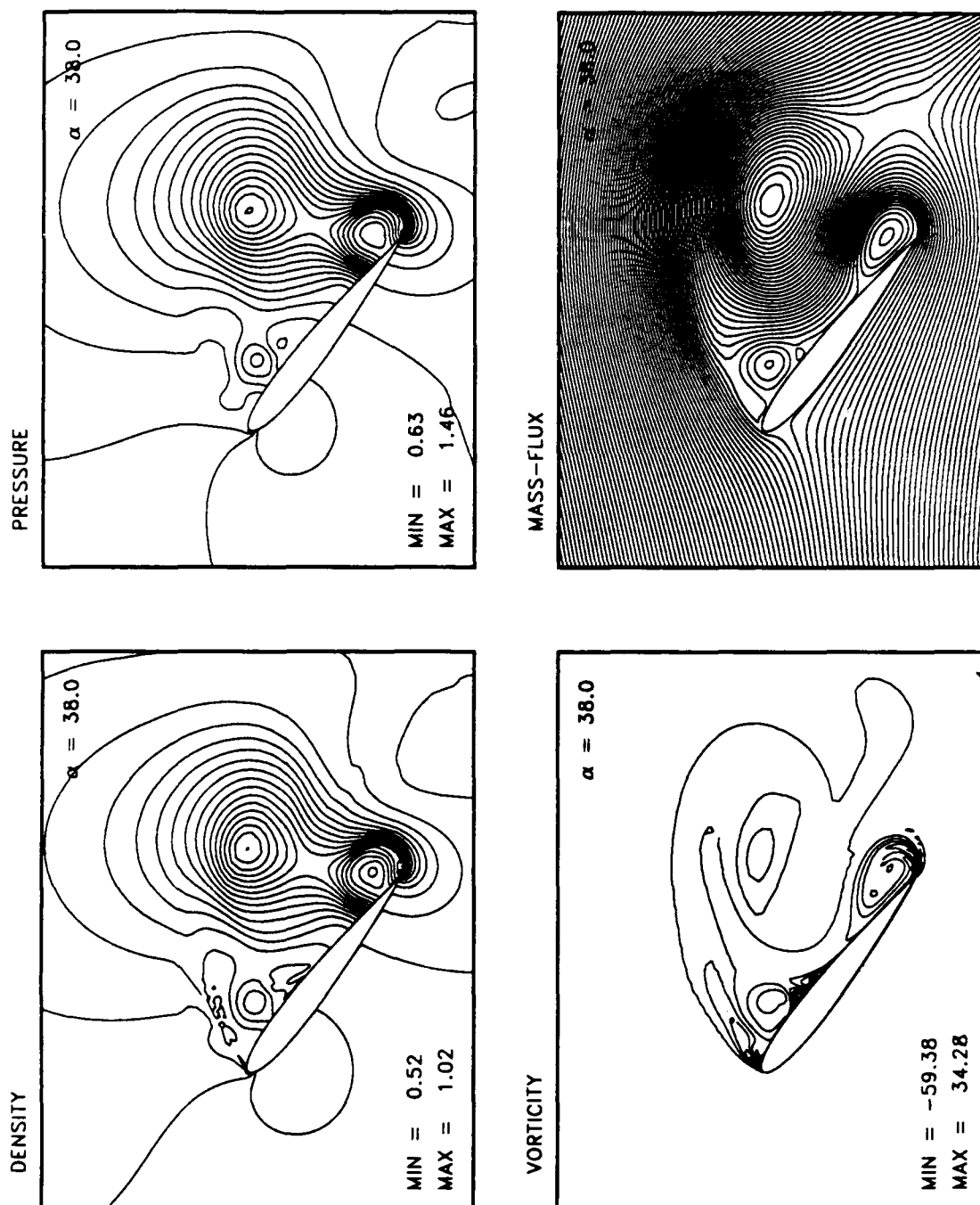


Figure 4.98: Ramp Motion Flow Details, $M_\infty = .3$, $k = .0127$, $Re = 2.7 \times 10^6$, $\alpha = 38.00^\circ$.

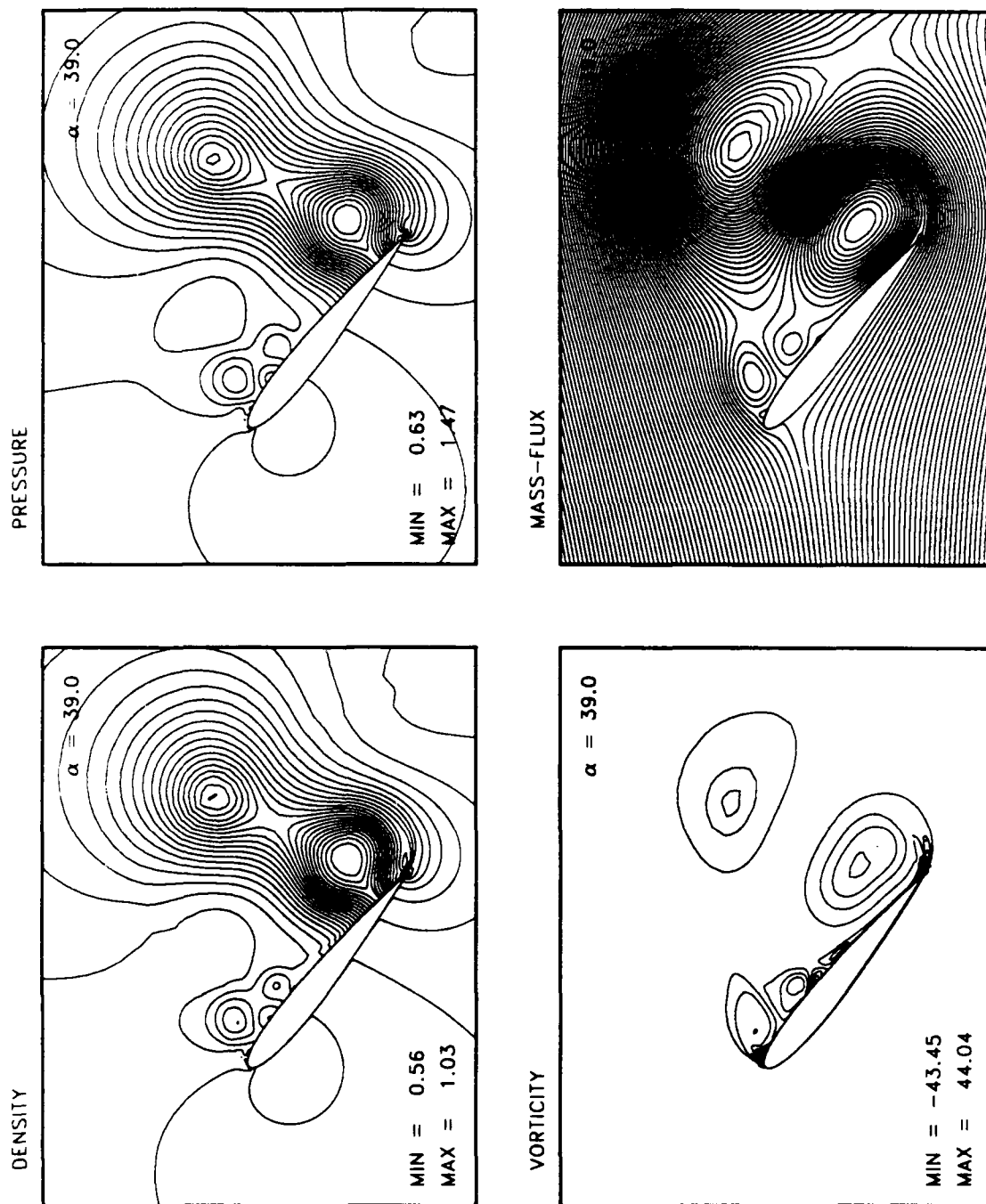


Figure 4.99: Ramp Motion Flow Details. $M_\infty = .3$, $k = .0127$, $Re = 2.7 \times 10^6$, $\alpha = 39.00^\circ$.

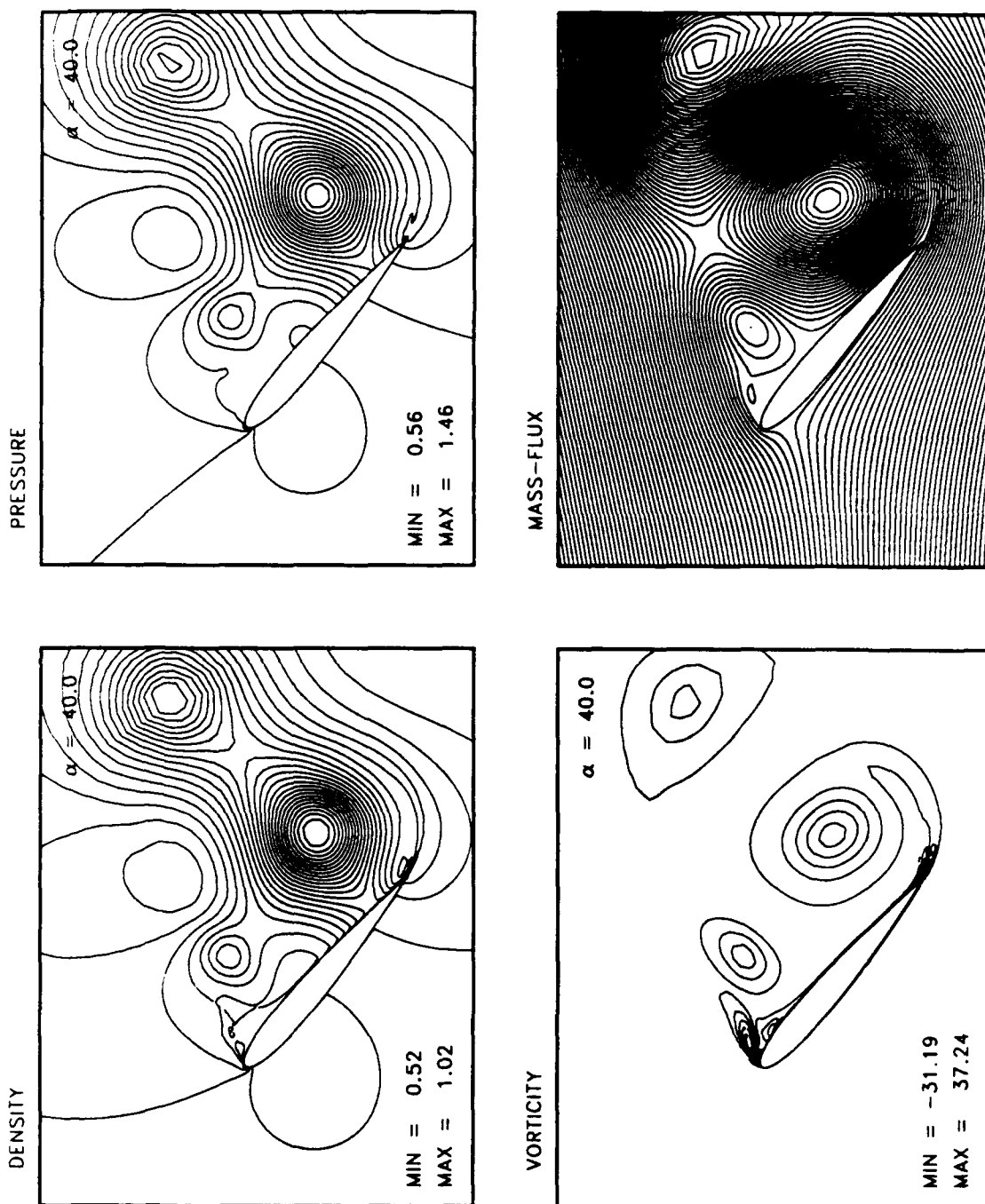


Figure 4.100: Ramp Motion Flow Details. $M_\infty = .3$, $k = .0127$, $Re = 2.7 \times 10^6$, $\alpha = 40.00^\circ$.

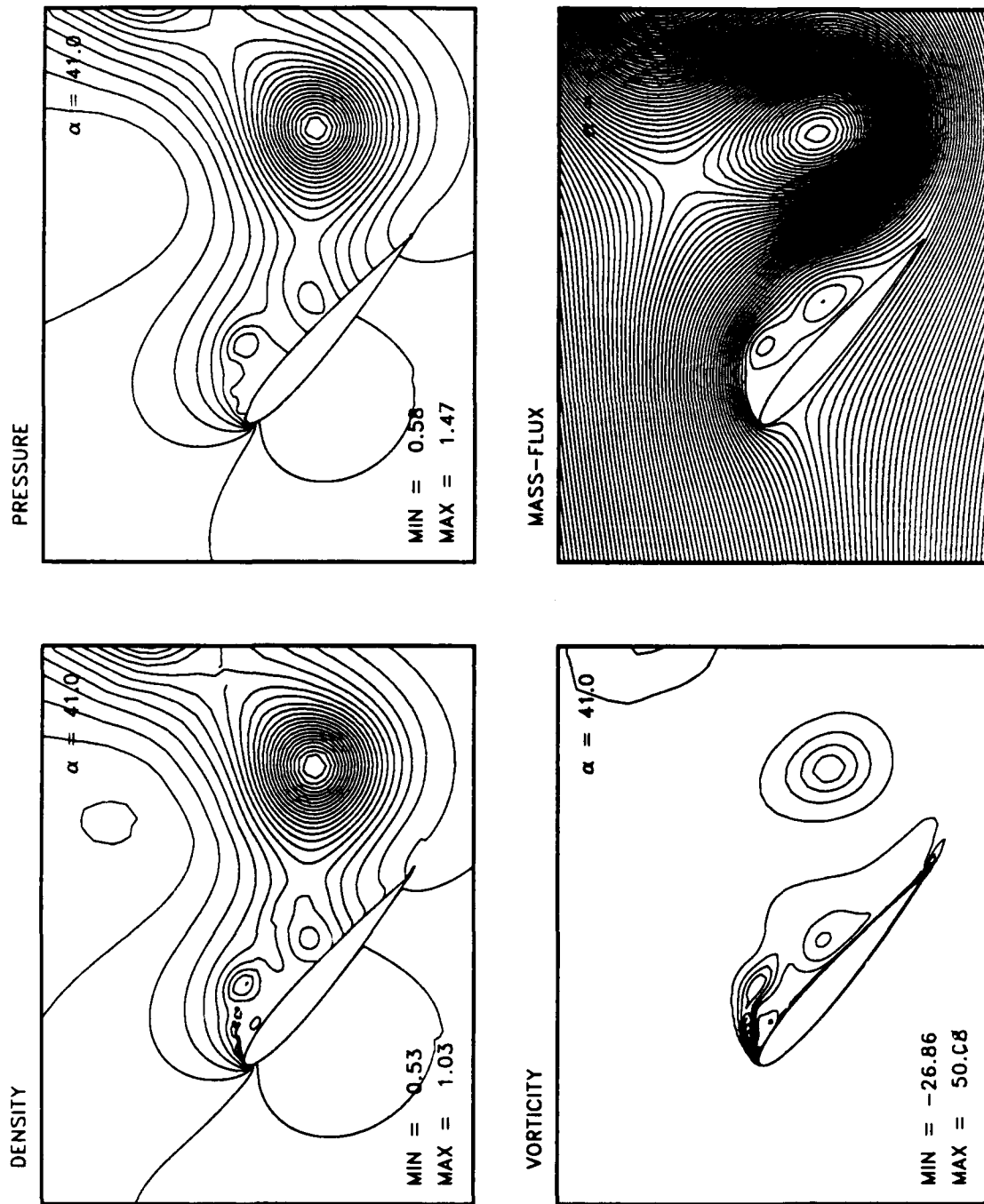


Figure 4.101: Ramp Motion Flow Details, $M_\infty = .3$, $k = .0127$, $Re = 2.7 \times 10^6$, $\alpha = 41.00^\circ$.

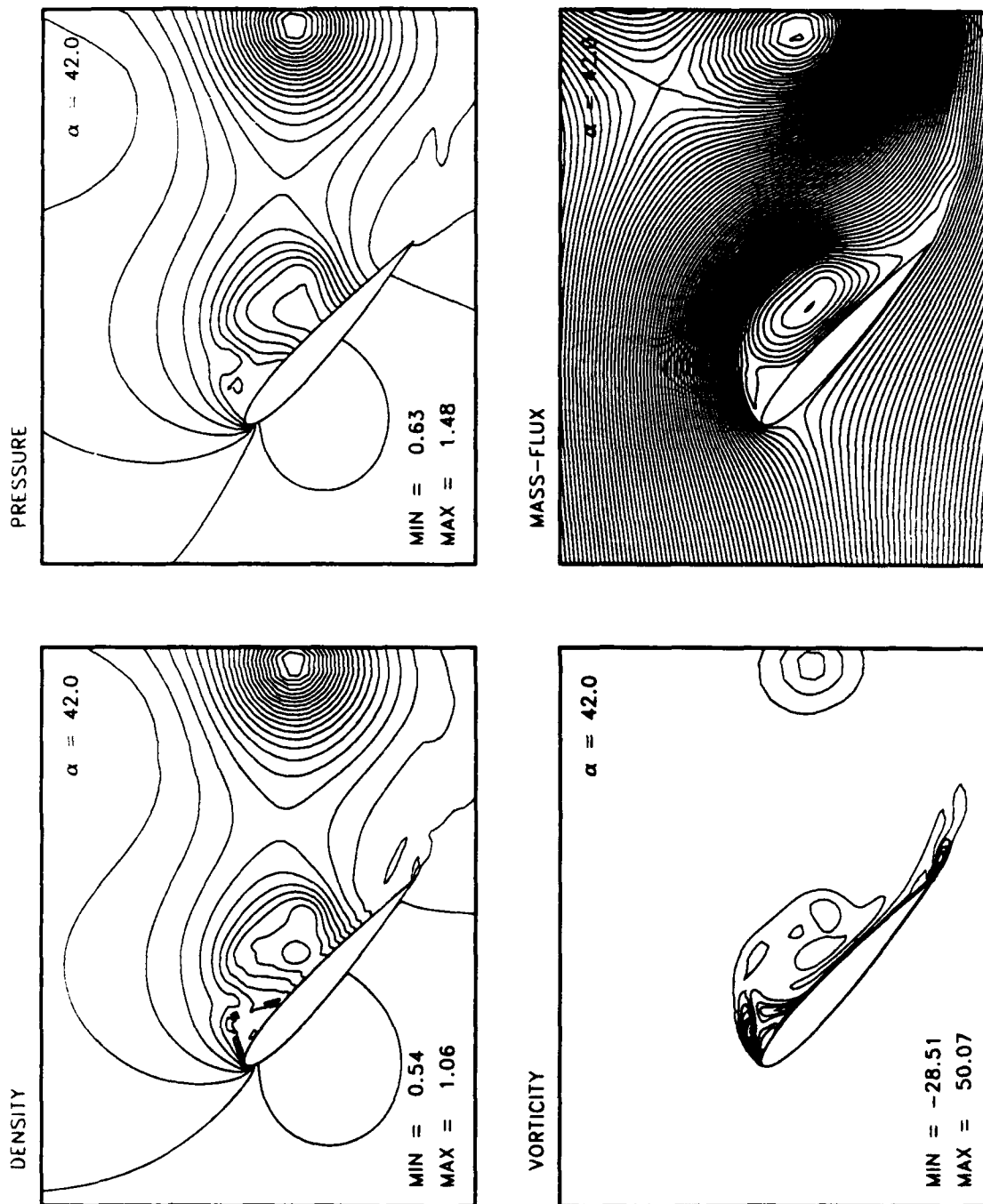


Figure 4.102: Ramp Motion Flow Details. $M_\infty = .3$, $k = .0127$, $Re = 2.7 \times 10^6$, $\alpha = 42.00^\circ$.

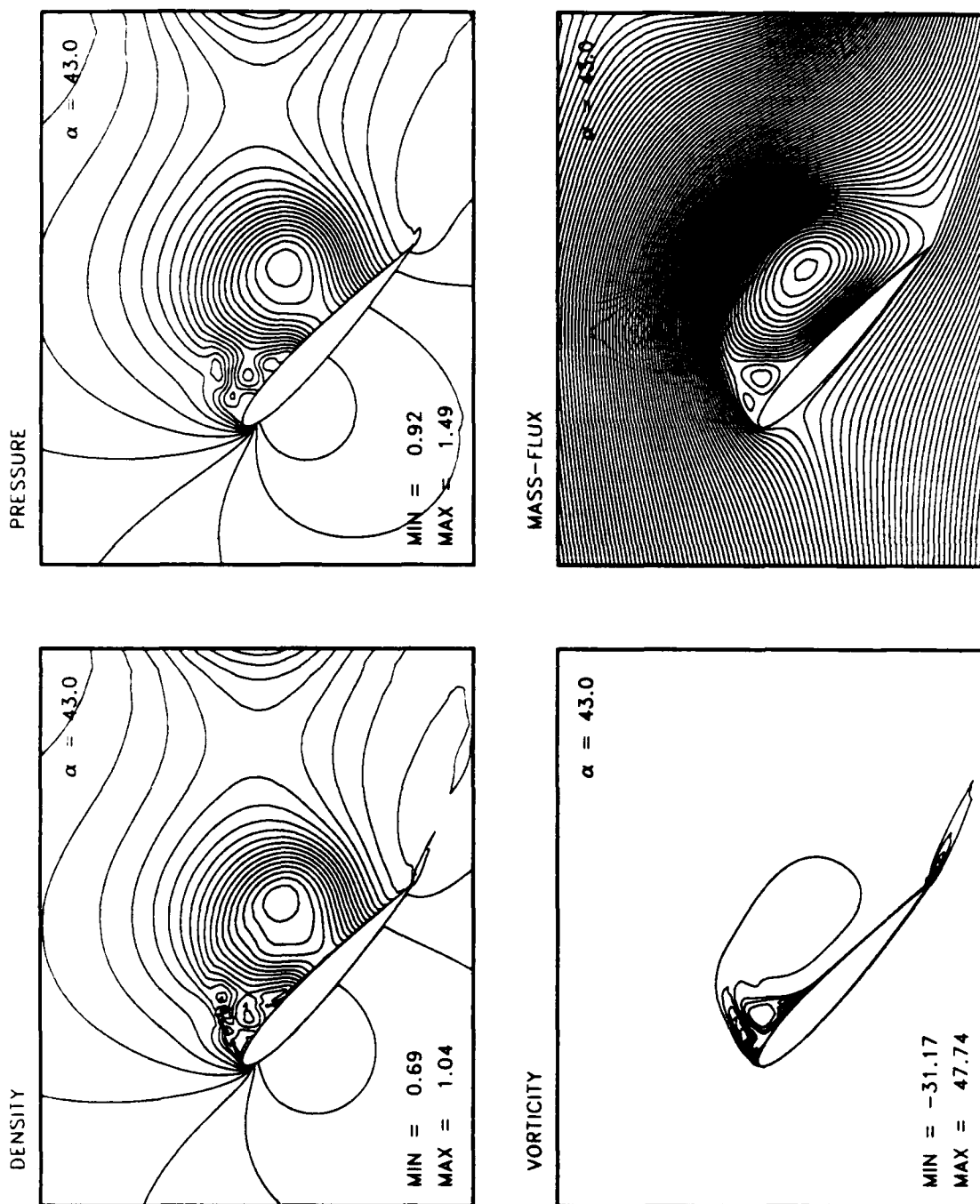


Figure 4.103: Ramp Motion Flow Details. $M_\infty = .3$, $k = .0127$, $Re = 2.7 \times 10^4$, $\alpha = 43.00^\circ$.

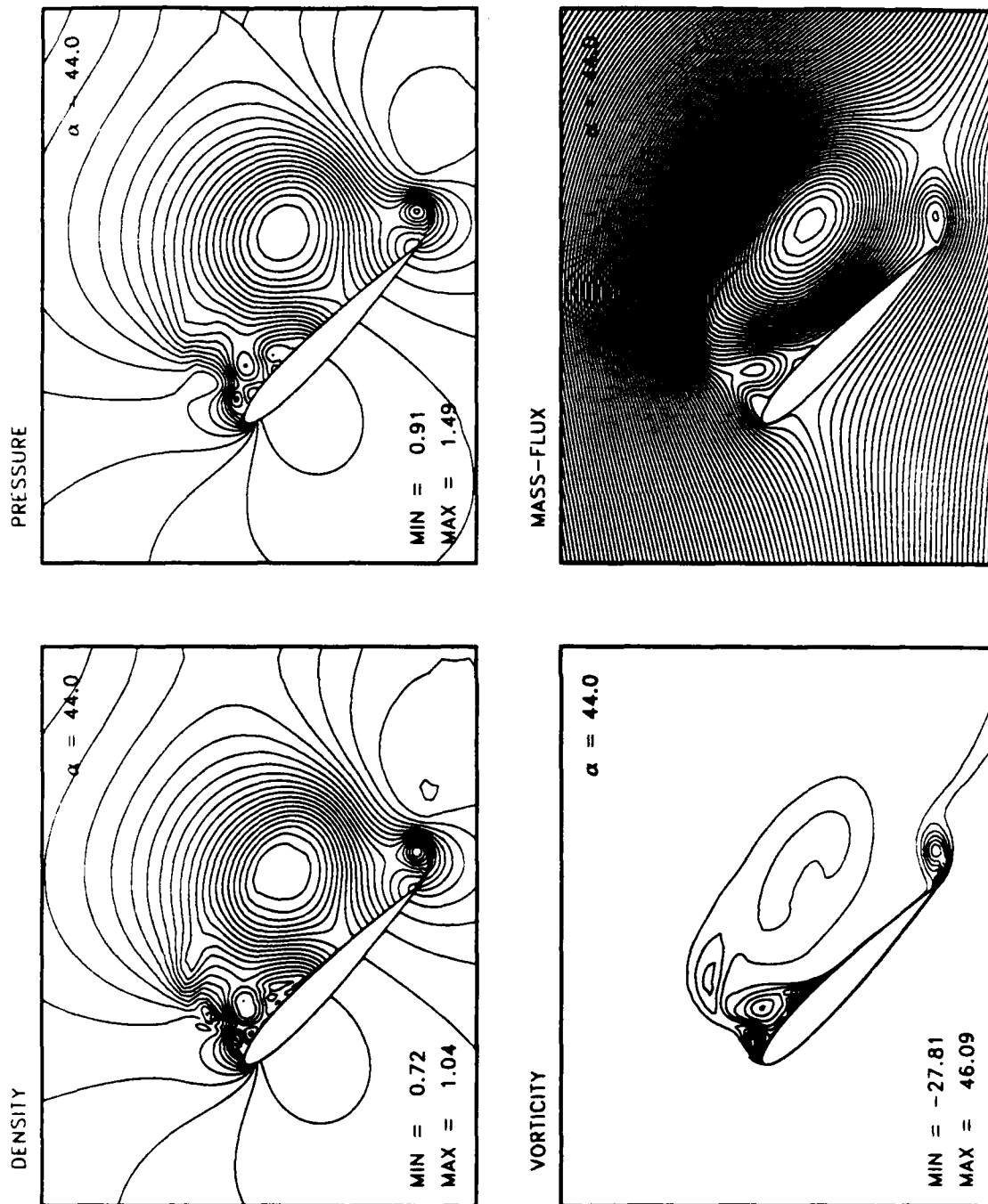


Figure 4.104: Ramp Motion Flow Details, $M_\infty = .3$, $k = .0127$, $Re = 2.7 \times 10^6$, $\alpha = 44.00^\circ$.

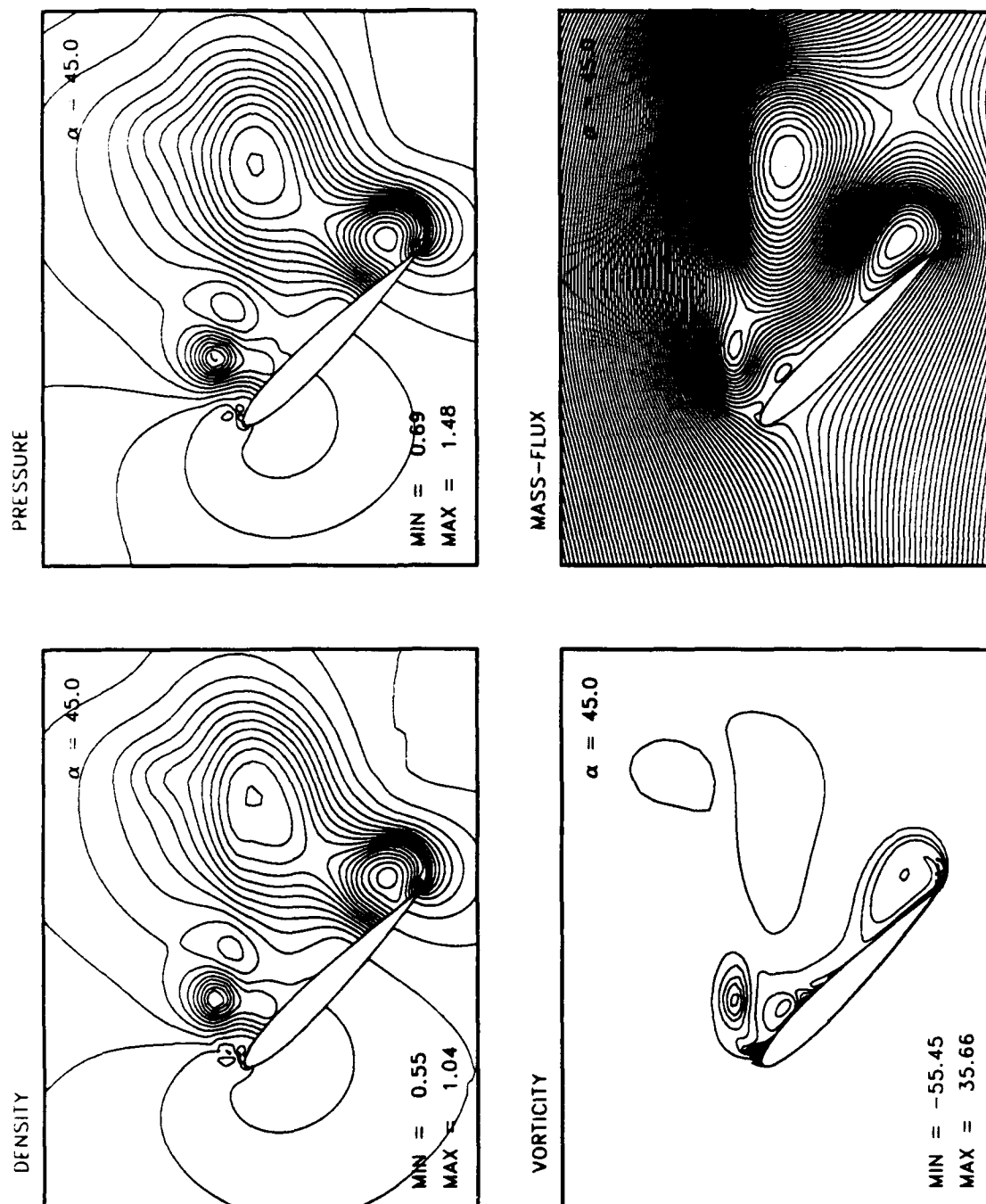


Figure 4.105: Ramp Motion Flow Details, $M_\infty = .3$, $k = .0127$, $Re = 2.7 \times 10^4$, $\alpha = 45.00^\circ$.

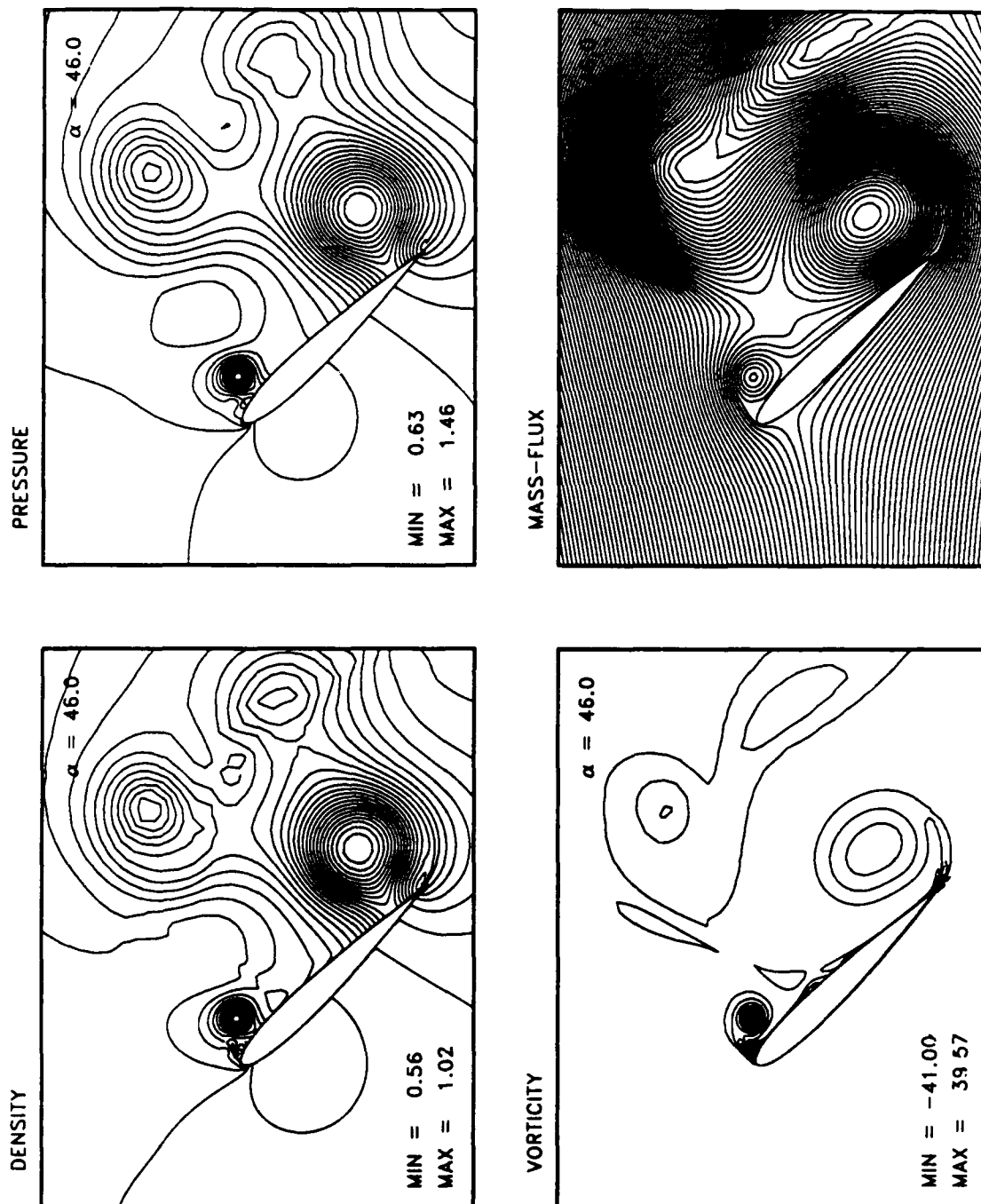


Figure 4.106: Ramp Motion Flow Details, $M_\infty = .3$, $k = .0127$, $Re = 2.7 \times 10^6$, $\alpha = 46.00^\circ$.

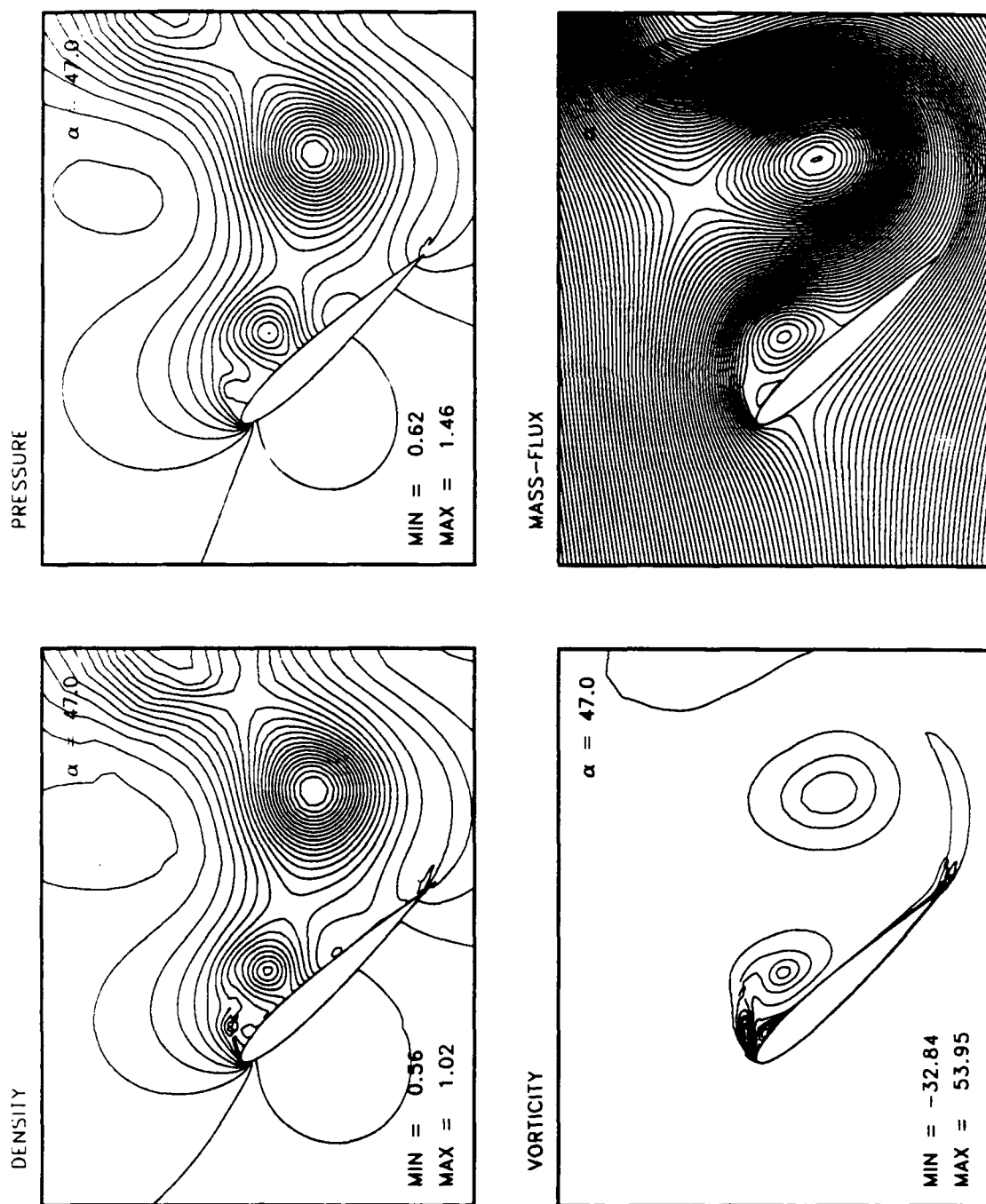


Figure 4.107: Ramp Motion Flow Details. $M_\infty = .3$, $k = .0127$, $Re = 2.7 \times 10^6$, $\alpha = 47.00^\circ$.

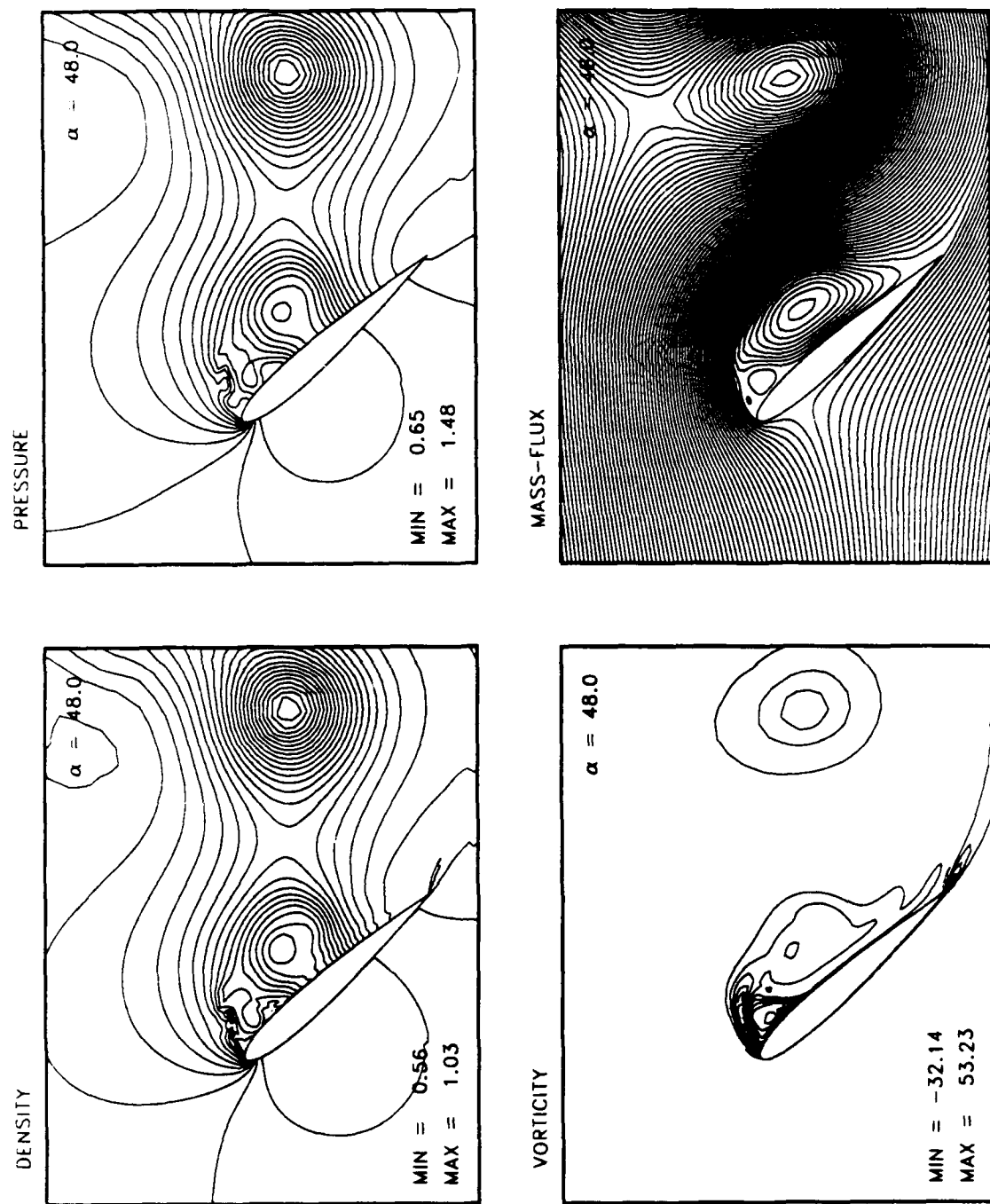


Figure 4.108: Ramp Motion Flow Details, $M_\infty = .3$, $k = .0127$, $Re = 2.7 \times 10^6$, $\alpha = 48.00^\circ$.

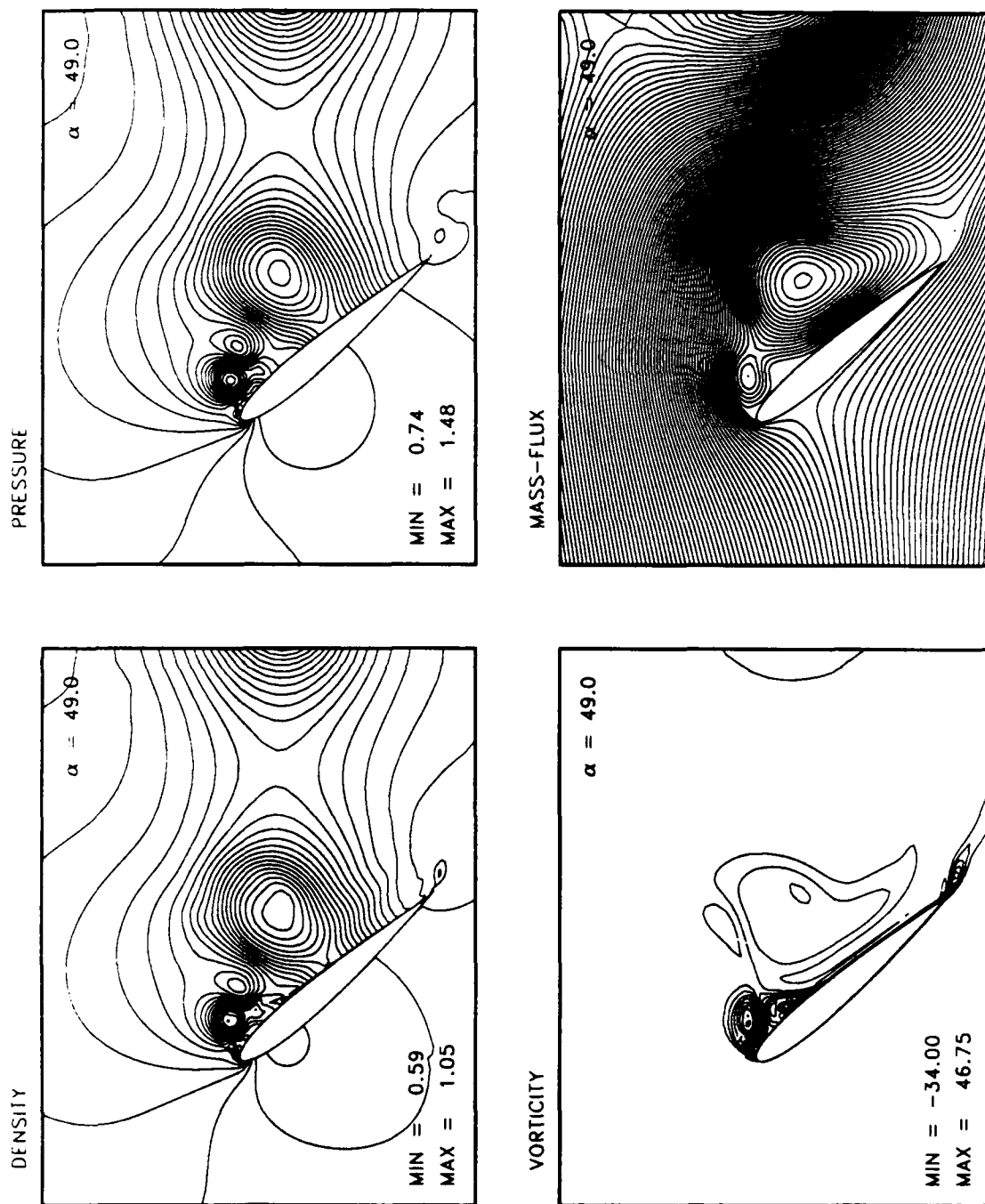


Figure 4.109: Ramp Motion Flow Details. $M_\infty = .3$, $k = .0127$, $Re = 2.7 \times 10^6$. $\alpha = 49.00^\circ$.

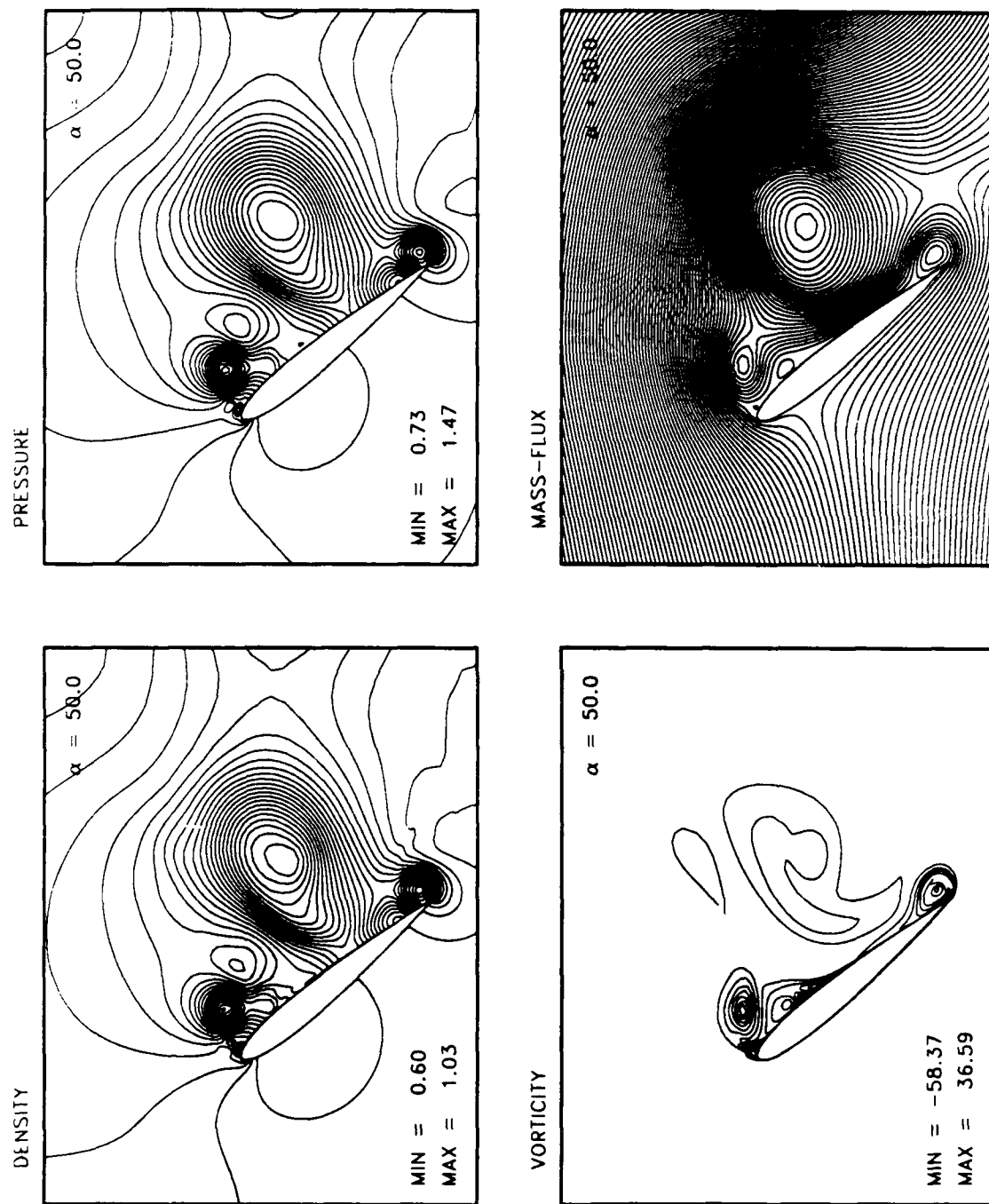


Figure 4.110: Ramp Motion Flow Details. $M_\infty = .3$, $k = .0127$, $Re = 2.7 \times 10^6$, $\alpha = 50.00^\circ$.

C. OSCILLATORY MOTION SOLUTION

The unsteady solution for a periodic oscillatory motion, given by $\alpha(t) = 4.86 + 2.44 \sin(\omega t)$, at $M_\infty = 0.6$, $Re_c = 4.8 \times 10^6$, with a reduced frequency of $k = 0.16$, was also obtained. Here the reduced frequency is defined as $k = \omega c / U_\infty$. The flow for this motion is initially purely subsonic; but, as the angle of attack increases to about $\alpha(t) \approx 5^\circ$, supersonic flow conditions are encountered at the leading edge region and a transonic shock forms. This shock is present during the upstroke until the maximum angle of attack is reached and during the downstroke up to about $\alpha(t) \approx 5.0^\circ$. The computed and measured lift and pitching moment response are compared in Figs. 4.111 and 4.112, respectively.

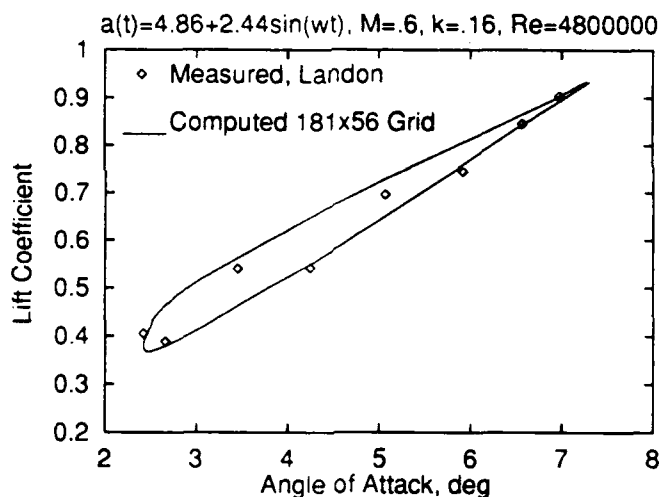


Figure 4.111: Comparison of Measured and Computed Lift for Oscillatory Test Motion

The computed lift and pitching moment coefficients are in close agreement with the measured values. The computed surface pressure distribution is compared with the measurements of reference [6] for two angles during the upstroke and two angles during the downstroke in Figs. 4.113 through 4.116. The computed surface pressure is in better agreement with the measurements at the lower angles of incidence ($\alpha = 5.95$

up and $\alpha = 5.11^\circ$ down). At higher incidences (Fig. 4.114 and 4.115), the agreement deteriorates in the region around the shock. The global view of the computed density field shows that the density contours smoothly cross the zonal interface for the case where a shock exists.

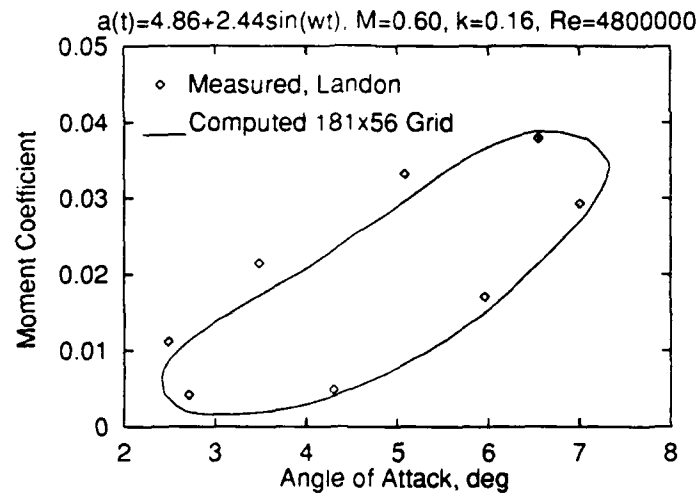


Figure 4.112: Comparison of Measured and Computed Moment Coefficient for Oscillatory Test Case

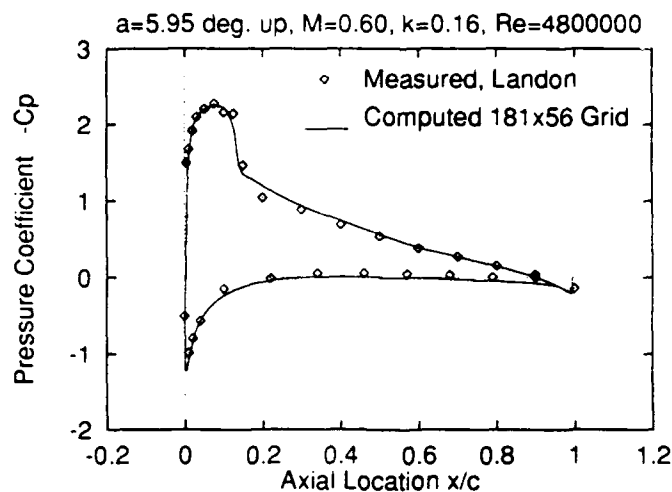


Figure 4.113: Comparison of the Measured and Computed Unsteady Surface Pressure Coefficient of Oscillatory Motion, $\alpha = 5.95^\circ$ upstroke.

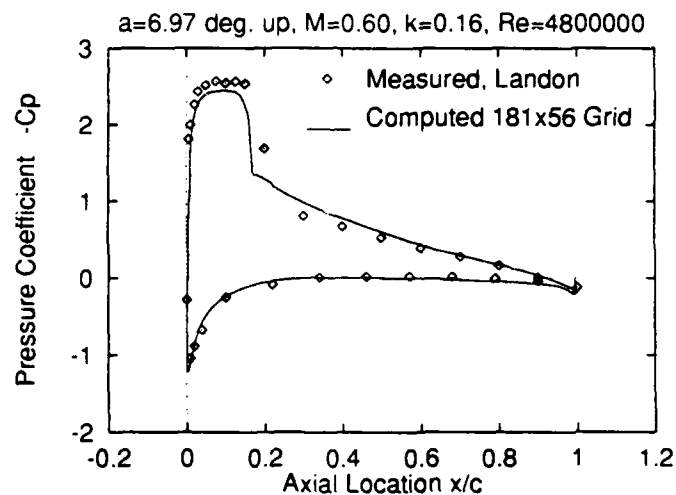


Figure 4.114: Comparison of the Measured and Computed Unsteady Surface Pressure Coefficient of Oscillatory Motion, $\alpha = 6.97^\circ$ upstroke.

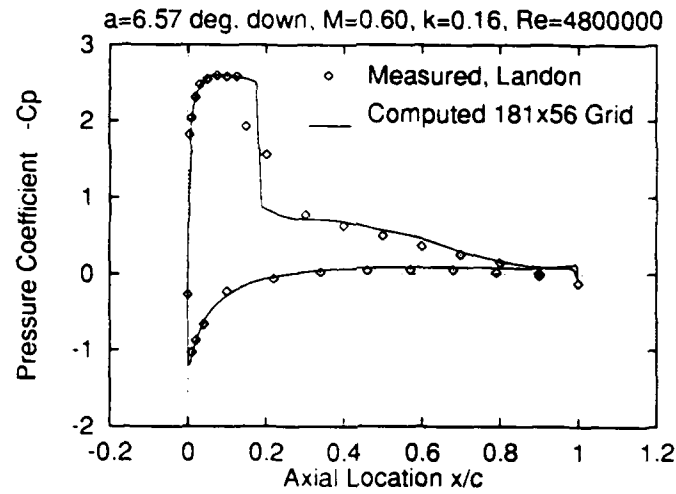


Figure 4.115: Comparison of the Measured and Computed Unsteady Surface Pressure Coefficient of Oscillatory Motion, $\alpha = 6.57^\circ$ downstroke.

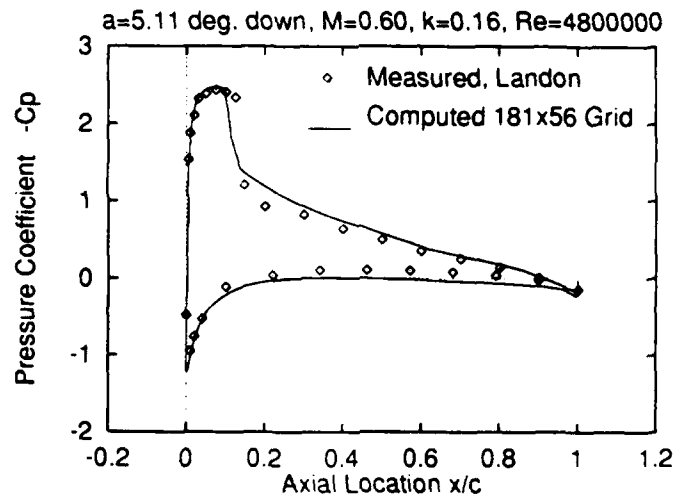


Figure 4.116: Comparison of the Measured and Computed Unsteady Surface Pressure Coefficient of Oscillatory Motion, $\alpha = 5.95^\circ$ downstroke.

V. CONCLUSIONS

A solution procedure suitable for steady and unsteady compressible flow solutions using zonal overlapped grids was developed. Simple weighted averaging was used at the overlapped zonal interfaces. Steady and unsteady, inviscid and viscous flow solutions for subsonic and transonic flows over airfoils were presented to validate the zonal grid approach.

The inviscid solutions presented show the overlapped zonal interface's ability to pass flow properties without distortion. It was found that for the inviscid test cases the location of the zonal interface is not important. In fact, as the zonal interface moved closer to the airfoil, while keeping the number of grid points constant, the pressure coefficient prediction actually improved. This is due to more grid points being clustered close to the airfoil. This test case had strong shocks on the upper and lower surface of the airfoil, and as the grid points were moved closer to the airfoil, the computed solution tended to have bigger oscillations near the shock.

The steady viscous test cases showed that using the Baldwin-Lomax turbulence model with the present approach gave accurate results for attached and mildly separated flow over stationary airfoils. This case demonstrates one of the advantages of the present approach, specifically, that solving the inviscid equations on the outer grid and the viscous equations on the inner grid gives good results. The flow variables were also passed smoothly through the zonal interface.

The ramp case again showed good agreement with experimental data. With this case another advantage of the present approach was displayed. The inner grid was rotated with the airfoil to the new angles of attack. The high order accurate scheme enabled the software to convect vortices, and at high angles, these vortices

convected up to 3 chord lengths.

The final test case was an oscillatory one. For this test case, supersonic flow was encountered on the upstroke at the leading edge region which produced a transonic shock. The computed lift and pitching moment coefficients are in close agreement with the measured values. At the higher angles of attack the agreement with measured data deteriorated in regions near the shock.

The following are some recommendations based on this study.

1. It has been shown that the zonal grid approach can be used to study unsteady viscous flows. A systematic comparison with other codes should be conducted in order to quantify the efficiency of the present approach.
2. Presently, there exists no easy way to generate zonal grids. In this study the grids were generated separately and then refined through several other programs. The development of a new or the modification of an existing software package such as GRAPE is recommended. The user should be able to specify, along with all the usual information, airfoil shape, the location of the overlapped region, the number of overlapped cells and the size of the outer grid.
3. An advantage of the present approach is that it can be extended to multiple inner and outer grids. A flow solver needs to be developed to take advantage of this so that effects of oscillating bodies in relative motion can be studied.

REFERENCES

1. Tyler, J. C., Leishman, J. G., "Analysis of Pitch and Plunge Effects on Unsteady Airfoil Behavior," American Helicopter Journal, Vol.37, No.3, pp69-82, 1992.
2. Chandrasekhara, M., Ahmed, S., and Carr, L., "Schlieren Studies of Compressibility Effects on Dynamic Stall of Airfoils in Transient Pitching Motion," AIAA Paper-90-3038, Aug. 1990.
3. Carr, L. W., "Progress in Analysis and Prediction of Dynamic Stall," Journal of Aircraft, Vol.25, No.1, pp.6-17, 1988.
4. McDevitt, J. B. and Okuno, A. F., "Static and Dynamic Pressure Measurements on a NACA-0012 Airfoil in Ames High Reynolds Number Facility," NASA Technical Paper 2485, June 1985.
5. McCroskey, W. J., McAlister, K. W., Carr, L. W., Pucci, S. L., and Lambert, D., "An Experimental Study of Dynamic Stall on Advanced Airfoil Sections," USA AVRADCOM TR 82-A-8, 1982.
6. Landon, R. H., "NACA 0012 Oscillatory and Transient Pitching," AGARD R 702, 1982.
7. Chandrasekhara, M. S., Brydges, B. E., "Amplitude Effects on Dynamic Stall of an Oscillating Airfoil", AIAA Paper No. 90-0575, Jan. 1990.
8. Chakravarthy, S. R., Szema, K-Y, Coldberg, U., and Corski, J. J., "Application of a New Class of High Accuracy TVD schemes to the Navier-Stokes Equations," AIAA Paper 85-0165, Reno, Nev., 1985.
9. Roe, P., "Some Contributions to the Modeling of Discontinuous Flows," Large Scale Computations in Fluid Mechanics, Lect. in Appl. Math., Amer. Math. Soc., 22-2, 1985, pp. 161-193.
10. Chakravarthy, S. R., "The Versatility and Reliability of Euler Solvers Based on High Accuracy TVD Formulations," AIAA Paper 86-0243, Jan. 1986.
11. Thompson, J. F., "A survey of dynamically-adaptive grids in the numerical solution of partial differential equations," Applied Numerical Mathematics, Vol.1 no. 1 p.3-27.
12. Rumsey, C. L. and Anderson, W. K., "Some Numerical and Physical Aspects of Unsteady Navier-Stokes Computations Over Airfoils Using Dynamic Meshes," AIAA Paper 88-0329, Jan. 1988.
13. Rubbert, P. E., Lee, K. D., "Patched Coordinate Systems," Numerical Grid Generation, J. F. Thompson, ed., North-Holland, New York, N.Y. 1982, pp 235-252.

14. Benek, J. A., Steger, J. L., Dougherty, F. C., "A flexible Grid Embedding Technique with Application to the Euler Equations," AIAA Paper No. 83-1911, July 1983.
15. Benek, J. A., Bunning, P. G. and Steger, J. L., "A 3D Chimera Grid Embedding Technique," AIAA Paper 85-1523, 1985.
16. Rai, M. M., "A Conservative Treatment of Zonal Boundaries for Euler Equation Calculations," AIAA Paper No. 84-0164, Jan. 1984.
17. Chesshire, G. and Henshaw, W. D., "Composite Overlapping Meshes for Solution of Partial Differential Equations," *Journal of Comp. Physics*, No 90, 1990, pp. 1-64.
18. Chyu, W. J., Davis, S. S., "Numerical Studies of Unsteady Transonic Flow over an Oscillating Airfoil," Agard Conference Proceedings No. 374.
19. Reu, T., and Ying, S., X., "A Composite Grid Approach to Study the Flow Surrounding a Pitch-Up Airfoil in a Wind Tunnel," AIAA Paper No 91-0599, Jan. 1991.
20. Rai, M. M. and Chakravarthy, S. R., "An Implicit Form of the Osher Upwind Scheme," *AIAA Journal*, Vol. 24, No. 5, May 1986, pp. 735-743.
21. Harris, C. D., "Two-Dimensional Aerodynamic Characteristics of the NACA 0012 Airfoil in the Langley 8 Foot Transonic Pressure Tunnel," NASA TM 81927, 1981.
22. Jang, H. H., Ekaterinaris, J. A., Platzer, M. F., and Cebeci, T., "Essential Ingredients for the Computation of Steady and Unsteady Boundary Layers," *Journal of Turbomachinery*, Vol. 13, Oct. 1991, pp. 608-616.
23. Schlichting, H., *Boundary-Layer Theory*, McGraw-Hill Book Company, 1966.
24. Anderson, D. A., Tannhill, J. C., and Pletcher, R. H., *Computational Fluid Mechanics and Heat Transfer*, Hemisphere Publishing Corporation, 1984.
25. Baldwin, B. S., Lomax, H., "Thin Layer Approximation and Algebraic Model for Separated Turbulent Flows," AIAA Paper 78-257, Jan 1978.
26. Cebeci, T., and Smith A. M., *Analysis of Turbulent Boundary Layers*, Academic Press, New York, 1974.
27. Sorenson, R. L., "A Computer Program to Generate Two-Dimensional Grids about Airfoils and Other Shapes by the Use of Poisson's Equation," NASA TM 81198, May 1980.
28. Steger, J. L. and Warming, R. F., "Flux Vector Splitting of the Inviscid Gas Dynamic Equations with Applications to Finite-Difference Methods," *Journal of Comp. Phys.*, Vol. 40, 1981, pp. 263-293.
29. Yee, H. C., "A Class of High-Resolution Explicit and Implicit Shock-Capturing Methods," NASA-TM 101088, Feb. 1989.

30. Yee, H. C., Warming, R. F., and Harden, A., "Implicit Total Variation Diminishing (TVD) Schemes for Steady State Calculations," NASA TM 84323, 1983.
31. Chakravarthy, S. R. and Osher, S., "A New Class of High Accuracy TVD Schemes for Hyperbolic Conservation Laws," AIAA Paper 85-0363, Jan. 1985.
32. Johnson, D. A. and King, L. S., "A Mathematically Simple Turbulence Closure Model for Attached and Separated Turbulent Boundary Layers," *AIAA Journal*, Vol. 23, No. 11, Nov. 1985, pp. 1684-1692.
33. Yakhot, V. and Orszag, S. A., "Renormalization Group Analysis of Turbulence. I. Basic Theory," *Journal of Scientific Computing*, Vol. 1, 1986.
34. Clarkson, J. D., Ekaterinaris, J. A., and Platzer, M. F., "Computational Investigation of Airfoil Stall Flutter," 6th International Symposium on Unsteady Aerodynamics, Aeroacoustics and Aeroelasticity, Sept. 1991.
35. Ekaterinaris, J. A., "Airfoil Flow Predictions Using an Upwind Scheme and Different Turbulence Models," Submitted to ASME Journal of Fluids Engineering.

INITIAL DISTRIBUTION LIST

		No. of Copies
1.	Defense Technical Information Center Cameron Station Alexandria, Virginia 22304-6145	2
2.	Library, Code 52 Naval Postgraduate School Monterey, California 93943-5002	2
3.	Dr. M. F. Platzer Department of Aeronautics and Astronautics, Code AA/PI Naval Postgraduate School Monterey, California 93943-5000	5
4.	Dr. J. A. Ekaterinaris NASA Ames Research Center (M.S. 258-1) Moffet Field, California 92035	2
5.	Dr. R. Kolar Department of Aeronautics and Astronautics, Code AA/Kj Naval Postgraduate School Monterey, California 93943-5000	1
6.	Dr. G. Hobson Department of Aeronautics and Astronautics, Code AA/Hg Naval Postgraduate School Monterey, California 93943-5000	1
7.	Mr. A. M. Cricelli Department of Aeronautics and Astronautics, Code AA/Tc Naval Postgraduate School Monterey, California 93943-5000	2